



<https://theses.gla.ac.uk/>

Theses Digitisation:

<https://www.gla.ac.uk/myglasgow/research/enlighten/theses/digitisation/>

This is a digitised version of the original print thesis.

Copyright and moral rights for this work are retained by the author

A copy can be downloaded for personal non-commercial research or study, without prior permission or charge

This work cannot be reproduced or quoted extensively from without first obtaining permission in writing from the author

The content must not be changed in any way or sold commercially in any format or medium without the formal permission of the author

When referring to this work, full bibliographic details including the author, title, awarding institution and date of the thesis must be given

Enlighten: Theses

<https://theses.gla.ac.uk/>
research-enlighten@glasgow.ac.uk

**Experimental Investigation of the Degradation of Ceramic
Composites in Aggressive Thermomechanical Environments**

Raymond. John. Gibson

Degree of MSc

University of Glasgow, Department of Mechanical Engineering

© December 1995

ProQuest Number: 10391304

All rights reserved

INFORMATION TO ALL USERS

The quality of this reproduction is dependent upon the quality of the copy submitted.

In the unlikely event that the author did not send a complete manuscript and there are missing pages, these will be noted. Also, if material had to be removed, a note will indicate the deletion.



ProQuest 10391304

Published by ProQuest LLC (2017). Copyright of the Dissertation is held by the Author.

All rights reserved.

This work is protected against unauthorized copying under Title 17, United States Code
Microform Edition © ProQuest LLC.

ProQuest LLC.
789 East Eisenhower Parkway
P.O. Box 1346
Ann Arbor, MI 48106 – 1346

Ther
10567
Copy 2



i. Acknowledgement

I would like to thank members of the staff in the Mechanical Engineering Department, Glasgow University, UK and in particular to Dr R.D.Thomson for his countless time and effort in driving me to get this thesis finished. Particular thanks are also due to Mr R.Hillier, then of Rolls Royce, for much useful discussion.

ii. Synopsis

To support a design methodology using monolithic and ceramic composites for use in aerospace components, an experimental test programme was initiated at Engineering Design and Research Centre (EDRC) /Glasgow University (GU) in 1990 to test advanced materials at ambient and elevated temperatures. This was carried out in conjunction with computer modelling and design system development. The facilities based at GU were restricted to thermal macromechanical testing. Due to the difficulty of achieving reproducible and reliable data from, eg tensile testing, simpler flexure and compression tests were preferred. Thermal shock, identified as a potential cause of failure in engineering ceramics, was shown by computational analysis to be less important than initially assumed. This was however not confirmed experimentally. Ambient and elevated macromechanical testing was therefore restricted to flexure tests carried out in an air environment under steady state conditions. The main focus of the test programme was to understand the physics of the composite materials and in particular the failure modes associated with specific loading configurations. Investigations of damage at stress concentrations or changes in fibre architecture and of delamination effects through varying changes in thickness was a key part of the study. The flexure tests would not only establish a materials properties and performance database, but will allow the fibre architecture of the loaded structure to be fully optimised

iii. Contents

	Page No
i. Acknowledgement	1
ii. Synopsis	2
iii. Contents Pages	3
iv. List of Figures	6
v. Tables.....	9
vi. List of Symbols.....	11

Chapter 1. Design of Monolithic and Ceramic Composites for Aerospace Propulsion.

1.0 Introduction.....	13
1.1 Materials For Ambient Experimental Testing	15
1.2 Materials For High Temperature Applications.....	16
1.3 Composites Manufacture & Design	17
1.3.1 Polyester Matrix Composites-Model Materials.....	17
1.3.2 Ceramic Matrix Composites.....	18
1.3.2.1 DuPont Lanxide Ceramic Composites.....	22
1.3.2.2 Amercom 3D Braided Ceramic Composites	23

Chapter 2. Test Programme Design

2.0 Introduction.....	25
2.1 Design Of Sub-Element Testpieces	26
2.2 Design Of The Thermomechanical Test Rig.....	31
2.2.1 Loading System.....	32
2.2.2 Flexure Testing Of Brittle Materials.....	34
2.2.3 Compression Testing	39
2.2.4 Heating System.....	40
2.2.5 Radiation Heating By Infrared Heat Lamps	44
2.2.6 Vertical Prototype Designs	48
2.2.7 Horizontal Prototype Design.....	53
2.2.8 Calibration Of The Horizontal Prototype	59
2.2.9 Final Horizontal Furnace Design.....	63
2.3 Instrumentation & Control.....	66
2.3.1 Displacement Measurement And Control.....	67
2.3.2 Temperature Measurement And Control.....	70

2.3.3	Furnace Heat Lamp Control.....	72
2.3.4	Data Acquisition System.....	73
2.3.4.1	Single Buffered System.....	75
2.3.4.2	Double Buffered System.....	76
2.3.4.3	Lloyd RControl Software System	76
2.3.5	Data Logging Error Sources.....	77
2.3.6	Equipment Calibration	79

Chapter 3. Test Programme Results

3.0	Introduction.....	80
3.1	Mechanical Flexure Tests.....	81
3.1.1	Bend Bars.....	83
3.1.2	Model Material Bend Bar (MMBB).....	84
3.1.3	Dupont Lanxide Bend Bar (RSB)	86
3.1.4	Amercom Bend Bar (Amercom)	88
3.1.5	Wedge Sections.....	89
3.1.6	Model Material Wedge Bar (MMWS).....	89
3.1.7	Dupont Lanxide Reinforced Section (RSR).....	90
3.1.8	T-Section	92
3.1.9	Model Material T-Section (MMTS).....	92
3.1.10	Dupont Lanxide T-Section (RST).....	94
3.2	Thermomechanical Flexure Tests	100
3.2.1	Dupont Lanxide Bend Bar (RSB)	100
3.2.2	Amercom Bend Bar (Amercom)	102
3.2.3	Dupont Lanxide Reinforced Section (RSR).....	102
3.2.4	Dupont Lanxide T-Section (RST).....	104
3.3	Discussion	105
3.4	Conclusions.....	106

Chapter 4 Test Programme Initial Observations

4.0	Introduction.....	109
4.1	Non-Dimensionalised Comparative Graphs.....	110
4.1.1	Bend Bars.....	111
4.1.2	Wedge-Sections.....	113
4.1.3	T-Sections.....	114
4.1.4	Discussion	115

4.1.5	Conclusions.....	116
4.2	Mechanical and Thermomechanical Property Observations.....	117
4.2.1	Bend Bars.....	117
4.2.2	Wedge-Sections.....	120
4.2.3	T-Sections.....	122
4.2.4	Discussion.....	123
4.2.5	Conclusions.....	125
4.3	Damage Evolution in Ceramic Composites.....	127
4.3.1	Modulus Decay Curves.....	129
4.3.2	Calculation of the Damage (D) parameters.....	132
4.3.3	Discussion.....	134
4.3.4	Conclusions.....	134
4.4	Crack Growth Mechanism-Optical & Fractographic Examination.....	136
4.4.1	Bend Bars.....	136
4.4.2	Wedge Sections.....	142
4.4.3	T-Sections.....	147
4.4.4	Thermomechanical Tests.....	151
4.4.5	Discussion.....	152
4.4.6	Conclusions.....	153
4.5	Design System Finite Element Observations of the Sub-elements.....	161
4.5.1	Analysis of the Sub-elements.....	161
4.5.2	Discussion.....	164
4.5.3	Conclusions.....	164
4.6	Residual Strain Behaviour & Energy Release Rates.....	173
4.6.1	Bend Bars.....	173
4.6.2	Wedge Sections.....	175
4.6.3	T-Sections.....	177
4.6.4	Discussion.....	178
4.6.5	Conclusions.....	179
5.0	Final Conclusions.....	186
6.0	References.....	189
	Appendices.....	192

iv. List of Figures

Fig 1.3.2	Dimox matrix formation process
Fig 1.3.2.1(a)	Harness satin weave pattern
Fig 1.3.2.1(b)	Bar/washer orientation architecture
Fig 1.3.2.2	Three Dimensional braiding
Fig 2.1.1	Sub-element testpieces
Fig 2.1.2	Experimental design process
Fig 2.1.3	Theoretical transition graphs
Fig 2.2.1	Loading system
Fig 2.2.2	Ideal 3/4 point moment diagrams
Fig 2.2.3	Wedging Action
Fig 2.2.4	Twisting of rollers
Fig 2.2.5	Compression platens
Fig 2.2.6	Vertical Infra-Red (IR) Lamps
Fig 2.2.7	Specular and Diffuse surfaces
Fig 2.2.8	Design of infra-red lamp
Fig 2.2.9	IR lamp performance rates
Fig 2.2.10	Cylindrical Prototype Furnace
Fig 2.2.11	Redesign of the heat chamber
Fig 2.2.12	Vertical Cylindrical Furnace
Fig 2.2.13	Final Vertical Prototype Design
Fig 2.2.14	IR heat distribution
Fig 2.2.15	Operating view of split horizontal furnace
Fig 2.2.16	Lamp orientation of split horizontal furnace
Fig 2.2.17	Radiant focusing onto the testpiece
Fig 2.2.18	Split Horizontal Furnace
Fig 2.2.19	Temperature gradients along the testpiece

- Fig 2.2.20 Interior of the 'large' optical furnace
- Fig 2.2.21 Optical furnace on the test rig
- Fig 2.3.1 Differential LVDT set-up
- Fig 2.3.2 Adjustable Op Amp and 15V dc supply circuit
- Fig 2.3.3 Self-Tune Control
- Fig 2.3.4 Embedded thermocouple in dummy testpiece
- Fig 2.3.5 Power control using a phased angle thyristor
- Fig 2.3.7 Data Acquisition using the software package Labview
- Fig 2.3.8 Data Acquisition system using Lloyd software
- Fig 2.3.9 Ground loop problem/solution
- Fig 2.3.10 Low pass filtering system
- Fig 3.1(a) Idealised monotonic load-displacement graph
- Fig 3.1(b)/(c) Cyclic load/unload curves.
- Fig 3.1.2 Model material polymer/polymer bend bar load-displacement curves
- Fig 3.1.3 Dupont Lanxide SiC/Al₂O₃ bend bar load-displacement curves
- Fig 3.1.4 Amercom SiC/SiC bend bar load-displacement curves
- Fig 3.1.6 Model material polymer/polymer thicken section load-displacement curves
- Fig 3.1.7 Dupont Lanxide SiC/Al₂O₃ thicken section load-displacement curves
- Fig 3.1.9 Model material polymer/polymer t-section load-displacement curves
- Fig 3.1.10 Dupont Lanxide SiC/Al₂O₃ t-section load-displacement curves
- Fig 3.2.1 Dupont Lanxide SiC/Al₂O₃ bend bar load-displacement curves tested at 1273K
- Fig 3.2.2 Amercom SiC/SiC bend bar load-displacement curves tested at 1273K
- Fig 3.2.3 Dupont Lanxide SiC/Al₂O₃ thicken section load-displacement curves tested at 1273K
- Fig 3.2.4 Dupont Lanxide SiC/Al₂O₃ t-section load-displacement curves tested at 1273K
- Fig 4.1 Ideal comparison of load-displacement curves for a Ceramic and Polymer Composites
- Fig 4.1.1 Normalised model material and ceramic composite bend bars
- Fig 4.1.2 Normalised model material and ceramic composite thicken sections
- Fig 4.1.3 Normalised model material and ceramic composite t-sections

- Fig 4.2.1 SiC/Al₂O₃ and SiC/SiC bend bars load-displacement curves at room and 1273K
- Fig 4.2.2 SiC/Al₂O₃ thicken sections load-displacement curves at room and 1273K
- Fig 4.2.3 SiC/Al₂O₃ t-sections load-displacement curves at room and 1273K
- Fig 4.3. Flexure loading/unloading response; a)no damage present, b)with damage present
- Fig 4.3.1 Decay in elastic modulus as a function of displacement curves for each sub-element
- Fig 4.3.2 Damage curves for each of the sub-elements
- Fig 4.4.1-(a) Model material bend bar crack initiation, cycled to 2.5mm
- Fig 4.4.1-(b) Model material bend bar crack deflection, cycled to 6mm.
- Fig 4.4.1 (c) SiC/Al₂O₃ bend bar crack deflection, cycled to 2.5mm
- Fig 4.4.1-(d) SiC/Al₂O₃ bend bar crack deflection and branching, cycled to 3.5mm
- Fig 4.4.1-(e) SiC/Al₂O₃ bend bar taken to failure, cycled to 9mm
- Fig 4.4.1-(f) SiC/Al₂O₃ bend bar fractured surface.
- Fig 4.4.1-(g) Amercom SiC/SiC bend bar crack deflection, cycled to 2mm
- Fig 4.4.1-(h) SiC/SiC bend bar fractured surface
- Fig 4.4.2-(a) Model material thicken section crack deflection, cycled to 7.5mm
- Fig 4.4.2-(b) SiC/Al₂O₃ thicken section crack initiation, cycled to 0.472mm
- Fig 4.4.2-(c) SiC/Al₂O₃ thicken section crack deflection, cycled to 0.472mm
- Fig 4.4.2-(d) SiC/Al₂O₃ thicken section taken to failure, cycled to 2mm
- Fig 4.4.2-(e) SiC/Al₂O₃ thicken section fractured surface
- Fig 4.4.2-(f) SiC/Al₂O₃ thicken section fractured surface showing fibre pull-out
- Fig 4.4.3-(a) Model material t-section crack deflection and branching
- Fig 4.4.3-(b) Model material t-section crack opening, cycled to 7.5mm
- Fig 4.4.3-(c) SiC/Al₂O₃ t-section crack initiation, cycled to 1.5mm
- Fig 4.4.3-(d) SiC/Al₂O₃ t-section crack taken to failure, cycled to 6.4mm
- Fig 4.4.3-(e) SiC/Al₂O₃ t-section fibre pull-out shown on fractured surface
- Fig 4.4.3-(f) SiC/Al₂O₃ t-section crack deflection through fibre tow.
- Fig 4.4.4-(a) SiC/Al₂O₃ bend bar crack deflection, cycled to 2mm at 1273K
- Fig 4.4.4-(b) SiC/Al₂O₃ bend bar displaced to failure at 1273K
- Fig 4.4.4-(c) SiC/Al₂O₃ bend bar fractured surface at 1273K

- Fig 4.4.4-(d) SiC/Al₂O₃ bend bar oxidation of fractured surface at 1273K
- Fig 4.4.4-(e) Amercom SiC/SiC bend bar displaced to failure at 1273K
- Fig 4.4.4-(f) Amercom SiC/SiC bend bar fractured surface showing fibre pull-out at 1273K
- Fig 4.4.4-(g) SiC/Al₂O₃ thicken section prior to failure at 1273K
- Fig 4.4.4-(h) SiC/Al₂O₃ thicken section fractured surface at 1273K
- Fig 4.4.4-(i) SiC/Al₂O₃ thicken section fibre pull-out and deflection through fibre tow at 1273K
- Fig 4.4.4-(j) SiC/Al₂O₃ t-section prior to failure at 1273K
- Fig 4.4.4-(k) SiC/Al₂O₃ t-section fractured surface at 1273K
- Fig 4.4.4-(l) SiC/Al₂O₃ t-section fibre pull-out at 1273K
- Fig 4.5 Maximum stress conditions for the sub-elements
- Fig 4.5.1-(a) FE Analysis MMBB inplane stress
- Fig 4.5.1-(b) FE Analysis RSB inplane stress
- Fig 4.5.1-(c) FE Analysis MMWS inplane stress
- Fig 4.5.1-(d) FE Analysis RSR inplane stress
- Fig 4.5.1-(e) FE Analysis MMTS interlaminar stress
- Fig 4.5.1-(f) FE Analysis RST interlaminar stress
- Fig 4.6.1 (a) Bend bars non-dimensionalised residual behaviour
- Fig 4.6.1 (b) Bend bars non-dimensionalised energy release behaviour
- Fig 4.6.2 (a) Thickened sections non-dimensionalised residual behaviour
- Fig 4.6.2 (b) Thickened sections non-dimensionalised energy release behaviour
- Fig 4.6.3 (a) T-sections non-dimensionalised residual behaviour
- Fig 4.6.3 (b) T-sections non-dimensionalised energy release behaviour

Appendix 1

- A1-1 Induction Generator
- A1-2 Schematic Labview Software
- A1-3 Horizontal Split Furnace Exploded View
- A1-4 Horizontal Split Furnace Dimensional View
- A1-5 Horizontal Split Furnace Side/Base Exploded View

v. Tables

Table 2.2.7	Furnace Dimensions And Parameters
Table 3.1	Model Material Bend Bar (MMBB) Property Data
Table 3.2	DuPont Lanxide Bend Bar (RSB)/Amercom Property Data
Table 3.3	Model Material Wedge Section (MMWS) Property Data
Table 3.4	DuPont Lanxide Wedge Section (RSR) Property Data
Table 3.5	Model Material T-Section (MMTS) Property Data
Table 3.6	DuPont Lanxide T-Section (RST) Property Data
Table 3.7	DuPont Lanxide Bend Bar (RSB)/Amercom Property Data At 1273K
Table 3.8	DuPont Lanxide Wedge Section (RSR) Property Data At 1273K
Table 3.9	DuPont Lanxide T-Section (RST) Property Data At 1273K
Table 4.1	Model Material Mechanical Properties
Table 4.2	Ceramic Composite Mechanical Properties At Room Temperature And 1273K
Table 4.5.1	FE And Experimental Benchmarked Data
Table 4.5.2	Design System Generated Property Data
Table 4.6.1	Model Material Bend Bar Residual And Energy Release Data
Table 4.6.2	DuPont Lanxide Bend Bar Residual And Energy Release Data
Table 4.6.3	Model Material Wedge Section Residual And Energy Release Data
Table 4.6.4	DuPont Lanxide Wedge Section Residual And Energy Release Data
Table 4.6.5	Model Material T-Section Residual And Energy Release Data
Table 4.6.6	DuPont Lanxide T-Section Residual And Energy Release Data
Table 4.6.7	DuPont Lanxide Bend Bar Residual And Energy Release Data At 1273K
Table 4.6.8	DuPont Lanxide Wedge Section Residual And Energy Release Data At 1273K
Table 4.6.9	DuPont Lanxide T-Section Residual And Energy Release Data At 1273K

vi. List of Symbols

k	thermal conductivity (W/mK)
E, E_0	initial elastic modulus (GPa)
E_1	elastic modulus in the 1-direction (GPa)
E_2	elastic modulus in the 2-direction (GPa)
\bar{E}	damaged elastic modulus (GPa)
E_f	fibre modulus (GPa)
E_m	matrix modulus (GPa)
D	Damage parameter
b	breadth of beam (m)
d	depth of beam (m)
L	length of beam (m)
P	load (N)
P_m	microcracking load (N)
r	radius of roller (m)
G	energy release rate (mJ)
T	temperature (K)
Z	number of zones
J	radiosity
K	stiffness (N/mm)
δ	displacement (m)
δ_m, d_m	microcracking displacement (m)
δ_r	residual displacement (m)
δ_{rel}	reversible elastic displacement (m)
$\hat{\sigma}$	matrix stress tensor
σ, s_{11}	in-plane direct stress (N/m ²)
s_{22}	interlaminar direct stress (N/m ²)
σ_m	microcracking stress (N/m ²)
σ_u	ultimate stress (N/m ²)
σ_f	stress to failure (N/m ²)
σ_b	bending stress (N/m ²)
t_{12}, τ_{12}	interlaminar shear stress (N/m ²)
ϵ	in-plane direct strain
ϵ_m	microcracking strain
ϵ_f	strain to failure
ϵ_u	ultimate strain

M	bending moment (Nm)
ϵ	emissivity
F_{ij}	viewfactor
σ_{sb}	Stefan-Boltzmann constant
E_p	emissive power (W)
$\partial q/\partial t$	radiation heat flow (W)
\bar{e}	eccentric error
a_1	half of the support span L (m)
a_c	crack length (mm)
a_L	distance between lamps (mm)
ρ	pressure (N/m ²)
ν	Poisson's ratio
ν_f	fibre Poisson's ratio
ν_m	matrix Poisson's ratio
ϕ_i	incident angle ray
ϕ_r	reflected angle ray
δ_{kj}	Kronecker delta
N	normal

Chapter 1

Design of Monolithic and Ceramic Composites for Aerospace Propulsion

1.0 Introduction

Engineering ceramics feature a combination of high melting point, chemical stability and strength which makes them prime candidates for use in aggressive thermo-mechanical environments. Unfortunately, these desirable properties are associated with low fracture toughness, which make ceramic components sensitive to the presence of manufacturing defects and to in-service damage. In addition, differences in the elastic constants, thermal conductivities and expansion coefficients between the components of composite systems lead to poor tolerance to thermal stresses.

In aero-engines such as the Rolls-Royce RB211, ceramic coatings have been used as thermal barriers in combustion chambers and turbine stator blades for more than a decade. These coatings modify the film coefficients and so eliminate the need for cooling air required with uncoated components. Monolithic ceramics are more problematic but ceramic turbine blades and shroud rings have been bench tested by Rolls-Royce, while Ford and Nissan (Hancock et al, 1990) have tested ceramic radial turbine rotors, stators, regenerators and seals in automotive development programmes in Japan, Germany and the USA. However, progress in power systems design, whether in the automotive or aerospace industries, is limited by the difficulty of realising the potential of ceramics in practical engineering components. It is then appropriate to encourage only gradual expansion in the use of ceramics to avoid overreaching developments in the necessary materials technology and design methods.

With aero-engines it is prudent to develop the technology in components which are not flight-critical but this must be seen as part of wider, longer-term aim to develop general (computer-aided) design methodologies for ceramics and ceramic composites in severe engineering environments. There are two necessary and complementary approaches to this objective. The first is a materials engineering programme to improve fracture toughness by mechanisms such as transformation toughening or by the use second-phase particles or fibres, in order to produce benign rather than catastrophic failures. However, to allow the performance of ceramic components to be predicted with the same confidence as that of components using more conventional materials, this work must be complemented by the development of high-temperature test procedures which allow the identification and specification of appropriate design parameters.

The potential advantages of fibre reinforced systems can be compromised by both inappropriate design of the fibre architecture and of the fibre-matrix interface.

Fundamental understanding and control of these features is essential if ceramic composites are to be used in safety-critical components. The optimum fibre architecture is dependent on the stress state in the component but to determine this accurately would require a full thermomechanical analysis, which included:

- the effects of gas pressure and the associated transient and steady state heat flows,
- boundary effects and the behaviour of the ceramic-metal coupling,
- thermal and mechanical boundary conditions,

all in anisotropic components of uncertain material properties. The Catia CAE package has been enhanced (Hopper, McCafferty, Gibson 1993) to aid the design of composite components but while each iteration through the design loop might incorporate a more sophisticated material model, it is sensible to start any design analysis with a simple linear elastic isotropic model and relatively simple boundary conditions. The results of this,

especially the predicted directions for principal stresses, assists both in the design of the component and of the experiments to provide better measures of material properties and improved understanding of failure mechanisms in the real material. The analysis may then be repeated with an anisotropic material model and the fibre architecture modified until the response of a real component can be predicted with confidence. Such analysis have been reported elsewhere (Hopper et al 1993, McCafferty, Hancock 1992).

1.1 Materials for Ambient Experimental Testing

Ceramic composite testpieces are very expensive and much of the development of the test equipment and procedures can be done with 'model materials', each of which mimics at least one feature of the ceramic composite. Candidate model materials include refractory metals and monolithic ceramics. They may also include non-ceramic or mixed systems, such as:

glass fibres in a cement matrix, to show the toughening effect of fibres on a brittle matrix,

SiC fibres in a glass ceramic matrix, to favour breakage and pullout,

35-40% polyester fibres in a polyester matrix, to minimise modulus mismatch and so to mimic the behaviour of systems such as SiC/SiC.

A low-cost polymer composite system was developed by Rolls Royce (Butler 1991) simulating the behaviour of a homogenetic ceramic composite system such as SiC/SiC in which both fibre and matrix are chemically identical. The critical feature of such systems is that the components moduli are of the same order of magnitude, differing only by an amount which reflects the different morphology of the chemically identical fibre and matrix. This is in contrast to, say, CFRP where the carbon fibre modulus is several orders of magnitude greater than that of the, typically epoxy matrix. The Butler model material comprises polyester fibres with a modulus of 57MPa embedded in a matrix of

polyester with a modulus of 36MPa.

To investigate the feasibility of different fibre architectures, a number of model material testpieces were envisaged, including, thin coupons with 2-D architectures, thick coupons with 3-D architectures and simple sub-element testpieces. The Model materials consisted mainly of a Polyester resin/10 layers polyester fibre. The ready availability of the material allowed additional tests beyond those that would have been done on the limited number of ceramic composite testpieces available.

In the current work, polyester model material was used in tests at room temperature while true ceramic composites were procured for high-temperature work.

1.2 Materials For High Temperature Applications

High temperature materials which were investigated over the three year period included commercially available monolithic materials eg silicon carbides and nitrides, to give some confidence in the test procedures, and a range of ceramic-ceramic composites purposely developed and manufactured for RR, specifically Nicalon-reinforced alumina (2-D Lanxide) and Nicalon reinforced silicon carbide (3-D Amercom). Unfortunately not all of the testpieces were available in all of the materials.

The availability of continuous SiC fibres such as 'Nicalon' with good oxidation resistance at high temperatures offers the best potential for development of fibre-toughened ceramic composites (Evans, Marshall 1989). These differ from common fibre-reinforced polymers in a number of ways. Firstly, as the terminology implies, the primary role of the fibres is not to act as load carriers through a relatively weak matrix but to improve the toughness of strong but brittle monolithic ceramics. The material is then engineered such

that the strain energy, which would otherwise cause the initiation and propagation of a macrocrack, is dissipated in diffuse microdamage, via multiple matrix micro-cracking or fibre pullout and breakage. Again in contrast to fibre reinforcement, fibre-toughening requires a relatively weak fibre/matrix interface and, ideally, the use of relatively short fibres.

Toughness of the order of the $30 \text{ MPa m}^{1/2}$ needed for design in aero-engines, have been found (Evans, Marshall 1989) in SiC-SiC systems. Such systems have the added advantage of minimal thermal and chemical mismatch between the fibre and the matrix but their long-term performance at temperatures above 1400K, where degradation processes such as grain growth, stable crack growth and creep may compromise both strength and toughness, has yet to be proven.

1.3 Composite Manufacture and Design

1.3.1 Polyester Matrix Composites - Model Materials

The polyester-polyester matrix composites that were used as model material sub-elements were manufactured in sheet form of nominal thickness 3mm, consisting of a woven 0-90 polyester filament yarn, polyester resin and hardener. The manufacturing involved a 'hand lay-up' process, the term indicating that no special apparatus is usually required to provide pressure during the moulding stage (Phillips, 1989). In the simplest case a smooth flat surface, such as a sheet of thick metal plate is coated with parting agent and a first layer of catalysed resin is applied by brush. A layer of cloth is placed over it and the resin is absorbed. A second layer of resin and a second layer of filament sheet is applied in the same way; the procedure is repeated with alternative layers of resin and fibre until the desired thickness is achieved. The moulding is allowed to gel and then harden, either

at room temperature, or after gelation, removed to an air oven to speed up the hardening process.

For the polyester composite matrix, the resin was poured into a compression mould and the polyester fibre sheets aligned at 0° and 90° to each other forming a 10 ply $0/90^\circ$ polyester composite ~3mm thickness. The mould was allowed to set for a duration of 4 hours at a constant pressure of 3.5MPa. By keeping pressure on the composite and restricting the flow, fibre distortion can be avoided. This also expels any bubbles that are present to produce a 'void-free' composite. Curing of the polyester composite took place for 2 hours at a temperature of 450K. Sub-element bend bars 10mm wide were then cut from the sheet to be tested. Since the fibre-matrix interface of the model material is weak a low volume fraction of around 40% should allow the polyester composite system to model the ceramic composite system.

1.3.2 Ceramic Matrix Composites

Ceramic-fibre-ceramic matrix composites are of interest for applications in the aerospace industry because of their potential toughness and higher strength as compared to conventional monolithic ceramics, while retaining the normal attributes of refractories and high resistance to abrasion and corrosion. However some ceramic fabrication processes tend to mechanically and chemically damage the fibres when they are consolidated within a ceramic matrix. For example, the fibres may be broken by a pressing operation, or the high sintering temperatures required to densify the ceramic matrix may damage the fibres or cause them to react chemically with the matrix. In addition, traditional ceramic processing methods place limitations on the shapes and sizes of ceramic components that can be made conveniently (Schiroky, Urquhart 1989).

A joint venture developed by Lanxide Corporation and DuPont is being applied to gas

turbine engine components by DuPont Lanxide Composites Inc., using a new process for manufacturing ceramic composites known as the DIMOX process (Direct Metal Oxidation Process). Aluminium founders have long been aware of the phenomenon of spontaneous growth of ceramic-metal lumps on layers near the surface of molten aluminium. When certain alloys are held molten in air for long periods, the "fungus-like growth" occurs typically at the refractory metal/air interface. Impurities from the refractory may also play a critical role.

Newark (Butler et al, 1991) discovered methods for controlling the growth of such composites and related systems and based on this knowledge, started the company Lanxide in the USA in 1983. The process for the matrix formation and the composite formation is illustrated in fig 1.3.2a and 1.3.2b.

The essential features of the matrix formation process (fig 1.3.2(a)) are the reaction of the metal with the surrounding gas, typically aluminium with oxygen in the air, to give a porous oxide skeleton (Newkirk et al 1986). Capillary forces then encourage new metal to move through the skeleton (microscopic channels) to react with air at a free surface. The resulting matrix material is typically ceramic/metal composite which has discontinuous phase in a metallic matrix. The matrix normally exhibits a brittle failure mode, although the fracture toughness can be quite high due to the inclusion of the ductile metal. The use of a few per cent of magnesium and other elements such as Si, Ga, Sn and Pb speeds up the oxidation process. The processing temperature is around 1173K-1573K, but because of diffusion and growth aspect of the process, long periods of time typically 4 days, are required to build up a reasonable thickness of material.

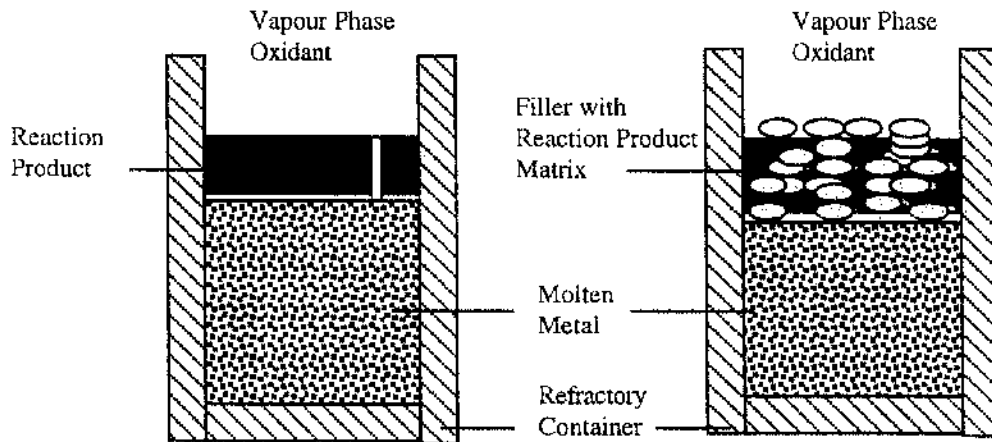


Fig 1.3.2 (a)

Fig1.3.2 (b)

A ceramic matrix composite (fig 1.3.2(b)) can be formed by the use of preforms of particulate or of a particulate or fibrous materials placed adjacent to the parent metal surface in the path of the outward oxidation growth process, thus growing a reaction product matrix through the filler mass (Newark et al 1987; Creber et, 1988; Schiroky et al 1989). In most cases some of the parent metal, or, alternately, a modified metallic constituent, is also present in the final composite (3-15% volume). The filler can be any material that is chemically compatible with the ceramic and metallic constituents of the matrix and with the growth atmosphere, and tolerates the growth temperatures. Incompatible fillers can often be used by applying compatible coatings to the filler.

This new manufacturing process (Chemical Vapour Deposition (CVD), Schlichting 1980, Caputo et al 1985, Borossa 1989) is quite versatile, compared to conventional ceramic technologies allowing the formation of a wide variety of composites in a range of shapes and sizes. The process also allows the engineering of specific materials properties through the selection of composite constituents and the control of the structure and microstructure of the composite. And, since matrix formation occurs by a growth process, there should be no densification shrinkage with the grain boundaries free of impurity phases favourable for high temperature properties.

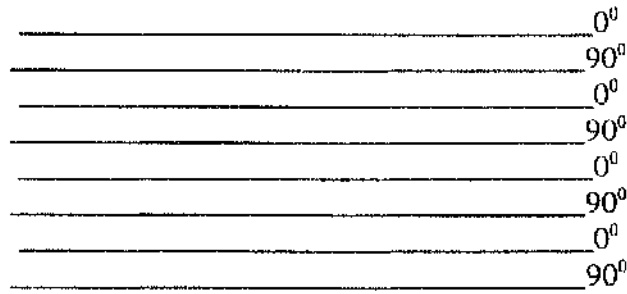


Fig 1.3.2.1(b) Bar and Washer orientation architecture

Alternating the plies means that nesting of the tows can be avoided and eliminates any difficulties that would occur in the proper coating of the fibres. The design also takes into account that the fill direction is typically about 10% weaker in tension than in the warp direction, though in compression the strengths are comparable. The thickened bar specimens are produced first by laying up the base plate of eight plies in a 0/90° pattern and in decreasing widths of plies. After processing the specimens are machined to shape. The cylindrical specimens were fabricated as a winding of fabric on a cylinder in either a 0° or 90° orientation. The ends of the fabric are located at the same circumferential position to avoid local excess thickness. The specimens are produced on a 4" long cylinder and cut to length after processing.

Finally the T-section subelements are fabricated by layup of 4 plies around a round-cornered mandrel, followed by a 4-ply layup of flat plies, and lastly 4 plies laid in the shape of a C applied on either end, forming a shape which, in cross section appears as a double sideways H. When split this yields four specimens. The central region of the T may not fill with the repositioned fibres during the forming process, and may require the laying in of a 1-D tow to fill the gap.

1.3.2.1 DuPont Lanxide Corporation Ceramic Composites

The subelements fabricated by DuPont Lanxide Corporation (DLC) ranged from bars to washers to T-Sections. The reinforcing fibres were Nicalon silicon carbide fibres in 500 fibre tows woven into 8 Harness Satin Weave (HSW) and 12 HSW cloth. The composite material was DLC Nicalon-reinforced alumina produced via the DIMOX process. In an eight-harness satin weave for example, one warp yarn runs over seven and under one fill yarn. Satin weaves are not as simple as the plain weave (one warp yarn running over and under one fill yarn) but offer more flexibility in addition to being pliable and with the ability to conform to complex and compound contours. The twelve-harness weave has a higher fabric count (number of warp or fill yarns per inch (cm)) which increases the composite strength. Plies can be layed up to form a multilayer composite, though the composite will be weak in interlaminar shear (Klein 1986). An example of a Harness Satin Weave pattern is shown in fig 1.3.2.1(a)

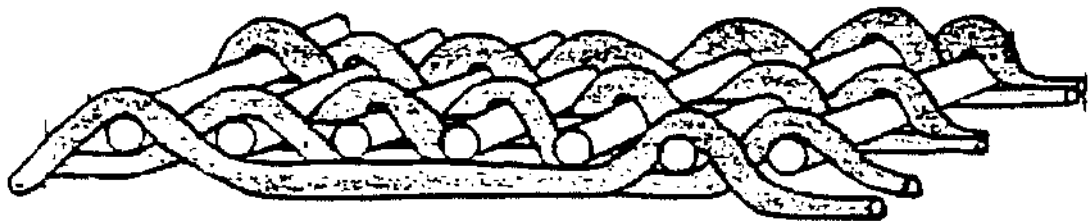


Fig 1.3.2.1(a) Example of a Harness Satin Weave pattern

The bar and washer shapes where produced in a $0/90^0$ orientation, beginning with an 8HSW ply, followed by 6 plies of 12HSW, followed by a final 8HSW in the orientation sequence shown below in fig 1.3.2.1(b).

1.3.2.2 Amercom 3D Braided Ceramic Composites

The Atlantic Research Corporation (Amercom) fabricated a similar range of subelements (exception of the thickened bar section) for evaluation and analysis, manufactured in a 3-D braided Nicalon-reinforced silicon carbide (SiC/SiC) ceramic composite. Amercom's through-the-thickness, or 3-D braiding, process uses a large braider with a 2,880 bobbin capacity, automated by their own software system. The braider can be programmed to produce irregular, solid or hollow textiles to net shape.

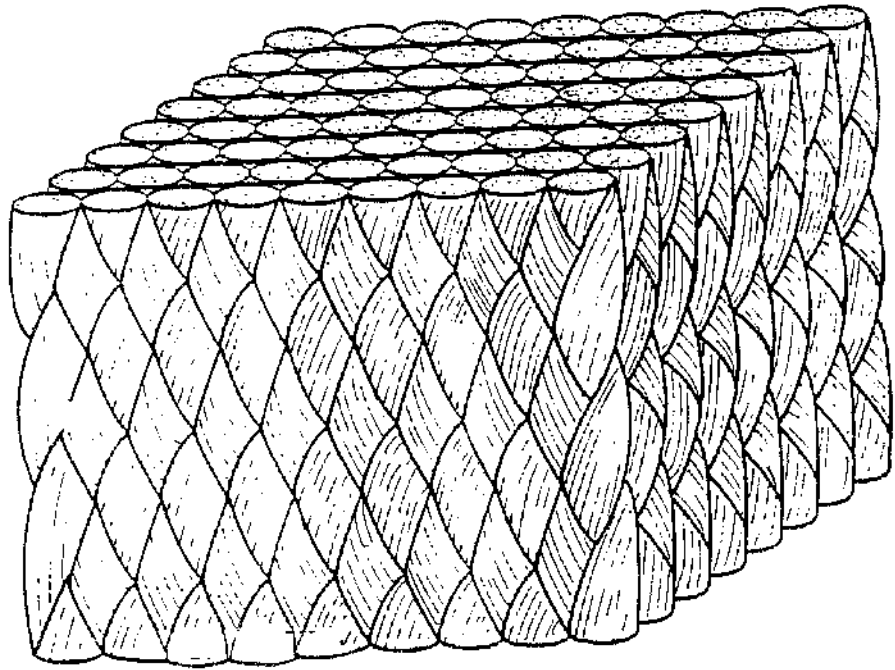


Fig 1.3.2.2 Through-the-thickness braiding (3-D)

By continuously intertwining reinforcing fibres, the three-dimensional braiding process is expected to improve delamination resistance and cracking, due to their non-orthogonal architecture as shown in fig 1.3.2.2. It is similar to two-dimensional braiding with the addition of a set of fibres that runs axially. During braiding, all of the fibre carriers move simultaneously, which is in contrast to most other weaves, where

fibre carriers move simultaneously, which is in contrast to most other weaves, where the warp yarns are fixed and the fill yarns are inserted. The process is generally slow with impregnation of resin difficult (Klein, 1986). Hybrids are feasible, using one type of fibre axially, and another type of fibres for the interwoven braids. Complex shapes can be made rigid, limited only by the size of the equipment, when a matrix material is added and the composite is cured. The exact manufacturing details for each subelement is unfortunately not known.

Chapter 2

Test Program Design

2.0 Introduction

A key part of the experimental programme was the validation of the design tools and methods, by means of sub-element tests. These also provide a means of acquiring relevant mechanical properties. The basic mechanical properties required by designers using composite orthotropic materials are the Young's moduli, shear moduli, Poisson's ratios and tensile, compressive and shear strengths (Rosensaft, Marom 1985). The point of first matrix micro-cracking is also an important design parameter. For basic understanding of deformation and failure mechanisms, interfacial bond strength and flexural testing are also necessary. For the envisaged applications these results are required at elevated temperatures. Toughness or work of fracture for fibre composites have to be interpreted and established if they are to be used as design parameters.

Tensile and flexural strengths and the stress at fracture are well established for monolithic ceramics. Unfortunately determining these for ceramic composites is not as straightforward due to the anisotropy in strength and elasticity. The common uniaxial tensile test has been found unsuitable for brittle materials which tend to break in the grips. Problems also arise from a lack of symmetry in loading. It is therefore easier to test such materials in bending. The maximum surface stress when a beam breaks in bending is called the modulus of rupture (MOR), a popular means of characterising the strength of engineering ceramics. If the specimens length is great compared to its width and depth, frictional effects at the contact points are negligible. Also if the specimen deforms only a little before failure, then the results obtained agree with simple beam theory.

Strength estimates of orthotropic composites generally have been obtained via flexural measurements using tests similar to those for isotropic monolithic ceramics, because of the ease with which these measurements can be made. Although flexural strength is not a commonly used material property in composites, flexure itself is useful in simulating behaviour during service. Several predicted failure modes are observed in flexural testing, depending on specific loading configuration, including fibre buckling, matrix fragmentation and shear failures. Investigation of damage arising at stress concentrations or changes in fibre architecture and of delamination effects through varying changes in thickness can also be observed. Matrix micro-cracking can be identified with the appearance of non-linearity in the load-displacement curve.

2.1 Design of Sub-Element Testpieces

To develop the capability to design and manufacture ceramic composite components suitable for use in gas turbine engines, generic testpieces which simulate, to some extent, the behaviour of a non-flight-critical component were developed. The geometrical shapes of the sub-element testpieces are a function of both the performance required in service and the restrictions imposed by the production process. While useful experiments can be conducted on coupons or simple shapes containing geometric features found in, say, the exhaust diffuser, they must all be capable of modelling, in a more or less limited way, the response and failure modes expected in the full-size component. The testpieces must be large enough to contain the generic geometric feature of interest and to be mechanically loaded while being heated but they must also be small enough for spatial temperature gradients to be minimised. A number of testpiece geometries were therefore considered, including:

- a) Bar sub-element to assess damage from point loading and determine basic properties such as elastic modulus.

- b) T-section sub-element to investigate damage such as mode-1 (tensile) delamination.
- c) Wedge sub-element to investigate damage such as mode-2 (shear) delamination.
- d/e) Washer/Cylindrical sub-element to investigate failure modes associated with through thickness thermal gradients and mechanical loads

The sub-element testpieces are shown in fig 2.1.1. To allow three-point bend loading on sub-elements (a)-(c) they were designed to be symmetric about their mid-section.

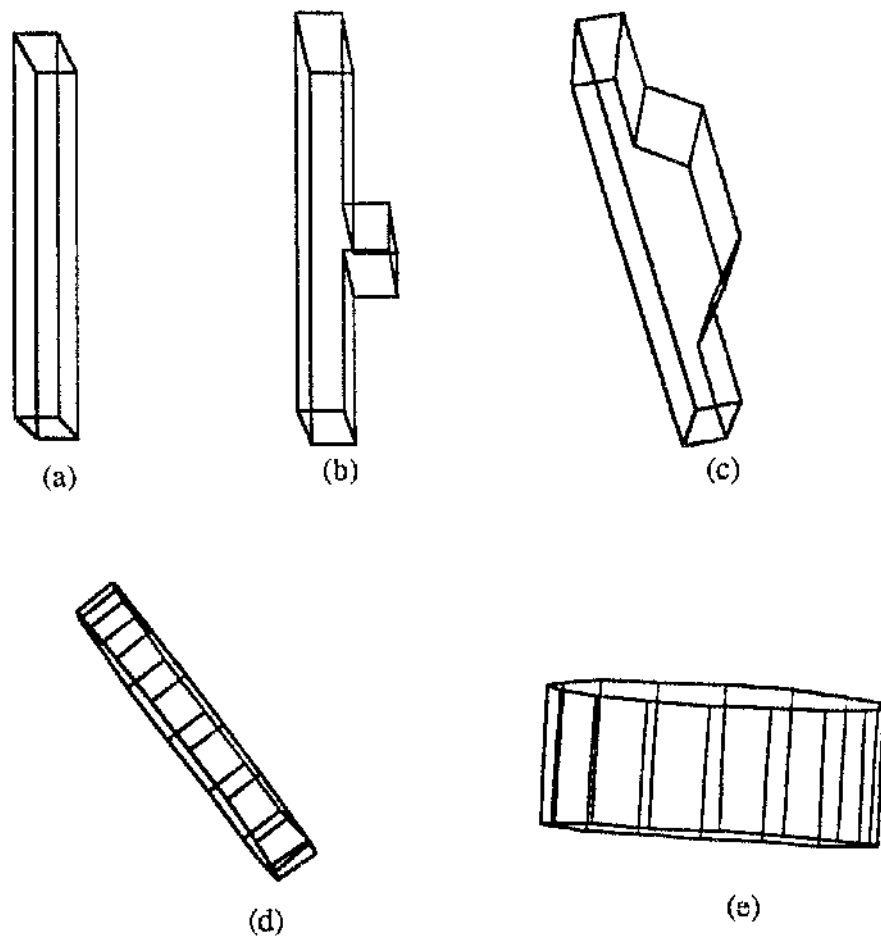


Fig 2.1.1 Sub-element testpieces

When designing in composites, not only is the component (shape) designed but also the material itself. These aspects cannot be considered in isolation. Candidate solutions are

proposed and analysed. These themselves will provide the initial property database to aid future design and optimization of the materials architecture. The design and analysis form an iterative loop, each repetition of the process incorporating more sophisticated models which converge to a final solution. This is true for whole components but is equally true for the experimental testpieces. The tests and analysis started with simple isotropic elastic materials and progressed to more complex anisotropic materials to determine the state of stress and so aid the optimization of fibre architecture. The experimental design process is shown schematically in fig 2.1.2.

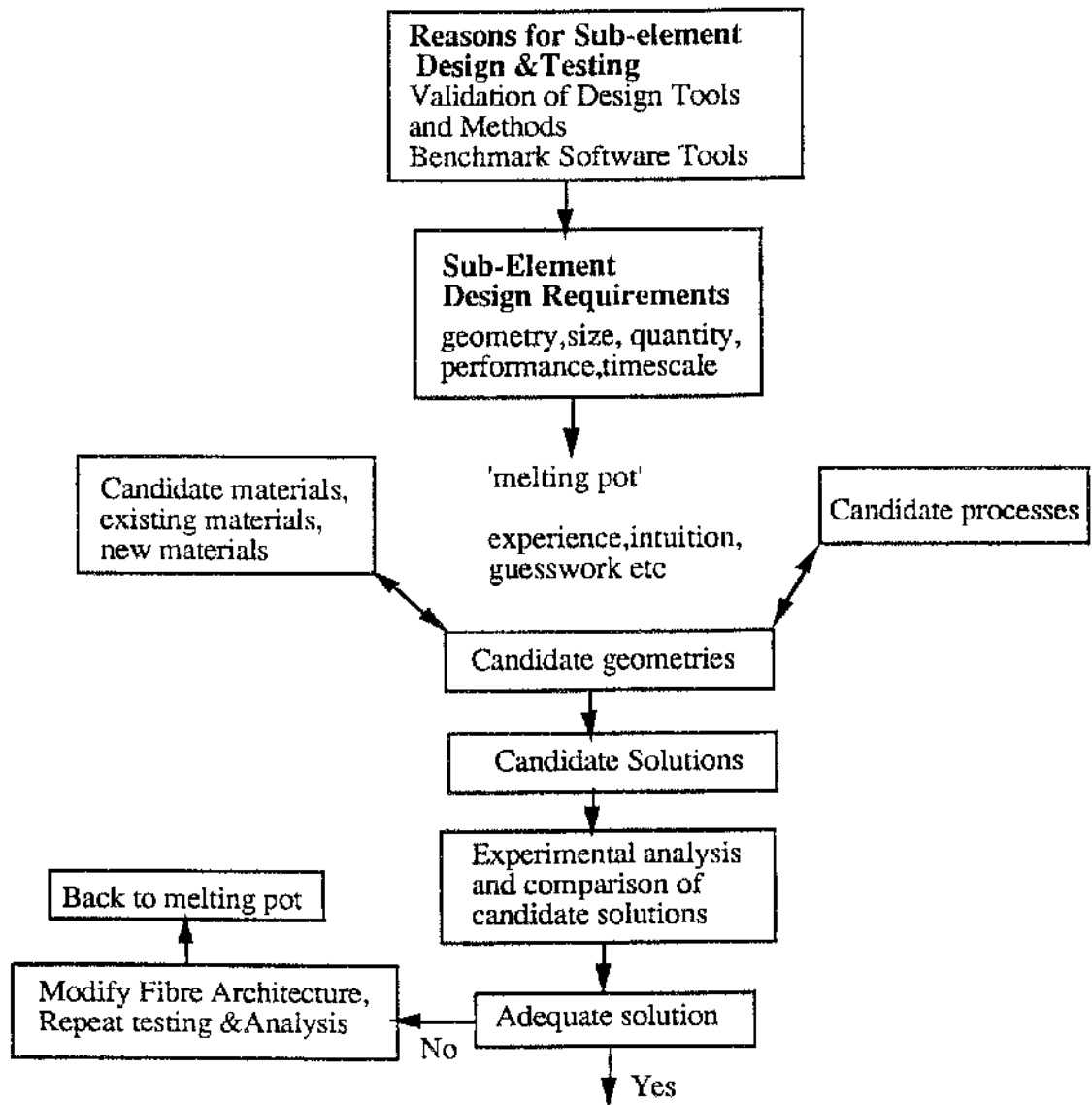


Fig 2.1.2 Experimental design process

Ceramic composites, unlike monolithic ceramics, exhibit anisotropic mechanical properties. In highly anisotropic materials it is crucial to ensure that the mode of failure actually found in the testpiece corresponds to that for which the test has been designed. Beam specimens are widely used in testing because the uniform cross-section simplifies fabrication and the design of grips, which are simple in comparison to those needed for tensile specimens. Beam specimens are used to develop both flexural and shear properties, the span to depth ratio governing the mode of failure by preferentially enhancing one stress component. For composites, the failure mode is also controlled by the volume fraction of fibres.

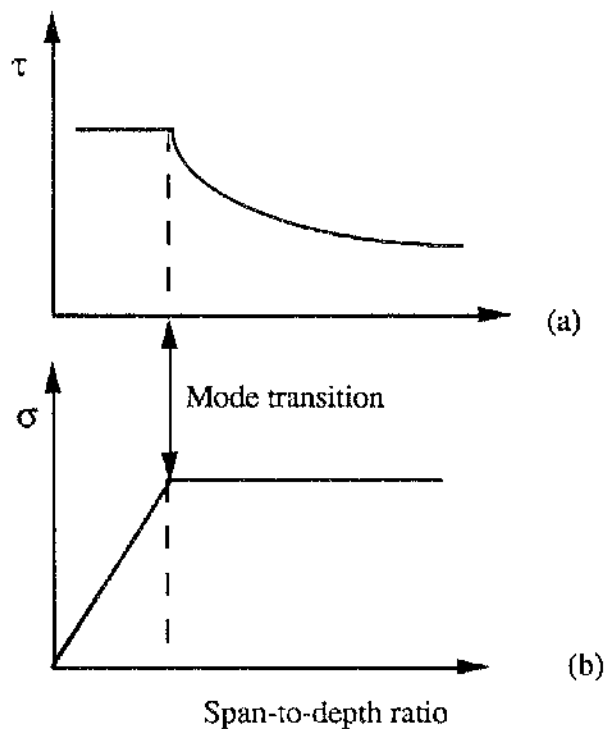


Fig 2.1.3 Theoretical shear graph (a) and tensile/compressive stress graph (b) as a function of Span-depth ratio

A short beam test is usually chosen for measuring the ultimate interlaminar shear stress. This occurs at the neutral surface and from elementary strength of material principles is given by $\tau_{\max} = \frac{3P}{4bd}$. A high span to depth ratio is selected for testing ultimate tensile (flexural) or compressive stresses. The maximum flexural stress occurring at mid-span in the top and bottom fibres is given by $\sigma_{\max} = \frac{3PL}{2bd^2}$.

The experimental test programme included both flexure testing and compression testing, and a span-to-depth ratio was chosen based on recent surveys of published work (Mecholsky, 1986) together with general guidelines on flexural testing of refractories (Loveday & Morrel, 1988). Generally, the ultimate flexural strength values are higher than the ultimate tensile strength values, with the calculated flexural strength or elastic modulus only approaching the ultimate tensile value for very large span-to-depth ratios. Since a universal test standard for ceramic composites hasn't yet been established, a span-to-depth ratio of 23:1 was chosen. This ensures a flexural failure and prevents the sub-elements failing in shear. The theoretical shear and tensile/compressive stresses as a function of the span-to-depth ratio is shown in fig 2.1.3. The mode transition points indicate the transition from shear (delamination) failure at a low span to depth ratios to tensile/compressive failure. Although there may be no prior knowledge of the shear strength of the composite, the shear strength of the unreinforced matrix may be used as a first estimate to obtain the transition value. Deviations from the theoretical tensile/compressive strength values are caused by a stress concentration around the loading nose, which causes local compressive failure.

2.2 Design of the Thermomechanical Test Rig

An experimental test programme to provide fundamental design data involving the effects of mechanical loading, induced by the exposure of thermal shock and thermal cycling, required the design and development of a special test-rig. This must allow thermophysical properties of ceramic composites to be measured in an environment similar to that expected in service, and which can be related to the component specification. The thermo-mechanical test-rig therefore consisted of two main components: a loading system and a heating system.

The loading system must include a testpiece-holder and a method of loading. Materials that can survive elevated temperatures for repeated long periods while retaining good mechanical and thermal properties are required for such duties. The choice of materials was governed by the upper temperature they can endure while maintaining high strength and oxidation resistance. Nimonic alloys exhibit good mechanical and thermal properties at elevated temperatures and, having been developed to operate in hostile environments, such as exist aircraft gas turbines, they were a suitable choice for the manufacture of the test rigs jigs and fixtures.

The heating system had to operate from ambient to 1273K in an air environment. It was also desirable that it would be versatile enough to accommodate various geometric sub-elements and be capable of operating in short burst and steady state thermal cycling modes.

2.2.1 Loading System

A special purpose loading system was designed and constructed to provide high accuracy with long term reliability and repeatability for flexure and diametrical compression loading as shown in fig 2.2.1. The force is applied through a push-rod attached via a calibrated interchangeable load cell to the moving crosshead of an JJ Lloyd LR30K Universal Testing Machine. Deformation measurements were made by linear variable differential transformers (lvdt's) mounted below the heat chamber connected to an alumina rod, which bears on the tensile face of the specimen. The main support columns for the loading system were machined from nimonic 90 alloy, while the loading rollers were fabricated from hot pressed silicon carbide and dense silicon nitride. To provide extra rigidity, and a flat base on which to work, a machined steel base plate replaced the universal test machines testbed. The support assembly was built-up from the base plate, with the support fixture being a push-fit onto the machines circular base ring. The support columns also had a push-fit tolerance. Off-axis alignment and rotation control could be adjusted on the support fixture base assembly. A 70mm/40mm adapter allowed smaller lengths of testpieces to be flexure tested. This was particularly useful for testing a supply of short monolithic materials, in accordance to ASTM C1161(1990) for testing brittle monolithic ceramics. Previous work carried out by Marsh & Bell (1988) and Chateigner & Jouin (1990) was taken into account in designing the loading system.

For the loads expected, push rods of 30mm diameter were chosen. The needs of the 3 and 4 point bending tests are met by a single bi-functional push-rod with a replaceable roller and an overall working length of 250mm. Load and deformation are constantly monitored during testing, using a computer for closed loop control. Constant-deformation rate testing with deformation cycling was the control mode for the tests. The computer was capable of scanning the two single channels as often as 1000 times per second, and saving the raw data on a file which could be read and translated by a spreadsheet.

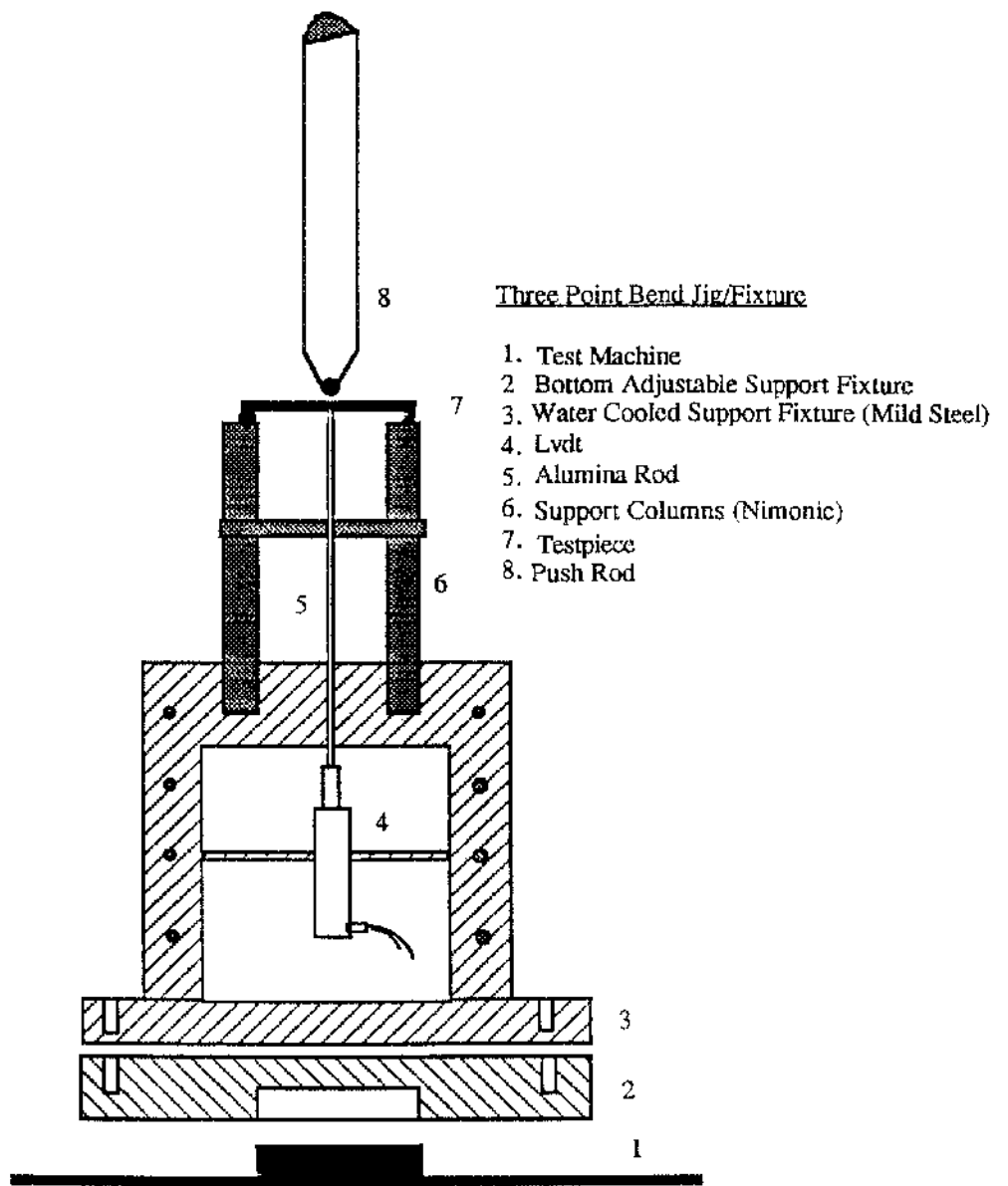


Fig 2.2.1 Loading system

2.2.2 Flexure Testing of Brittle Materials

Flexure testing of brittle materials is considerably more problematic than testing of ductile materials. Elementary beam theory predicts that the maximum stress in a beam occurs at the surface and that this stress is uniaxial. The value of this maximum stress at the instant of fracture is a conveniently obtained measure of the materials strength. Minimising errors imposed by displacements on the specimen during loading is therefore of vital importance if the stress predicted from simple bending theory is to be correctly calculated. The idealisation of simple beam theory is however rarely met, the practical prerequisite being that in flexure testing of brittle materials, the design of the specimen and the test rig are such that deviations from the stress distribution given by elementary theory are acceptably small. The objective therefore is to identify and isolate potential error sources in static bend tests.

Failure stress and strain can be calculated providing that simple bending theory is applicable, ie that:

- a). The material shows linear-elastic behaviour and the stress-strain relationship is identical in tension and compression.
- b). The beam is bent into an arc of a circle between the outer support rollers, with the specimens deflection being small in comparison to it's depth.
- c). Shear stresses are negligible compared to those caused by bending action.

An idealised moment diagram for three and four point bend tests is shown in fig 2.2.2. For the three point bend test the maximum moment and hence the the maximum stress occurs under the loading point at the mid-span position. Marschall & Rudnick (1974) and Baratta (1984) have identified experimental errors which occur during flexure testing of brittle materials.

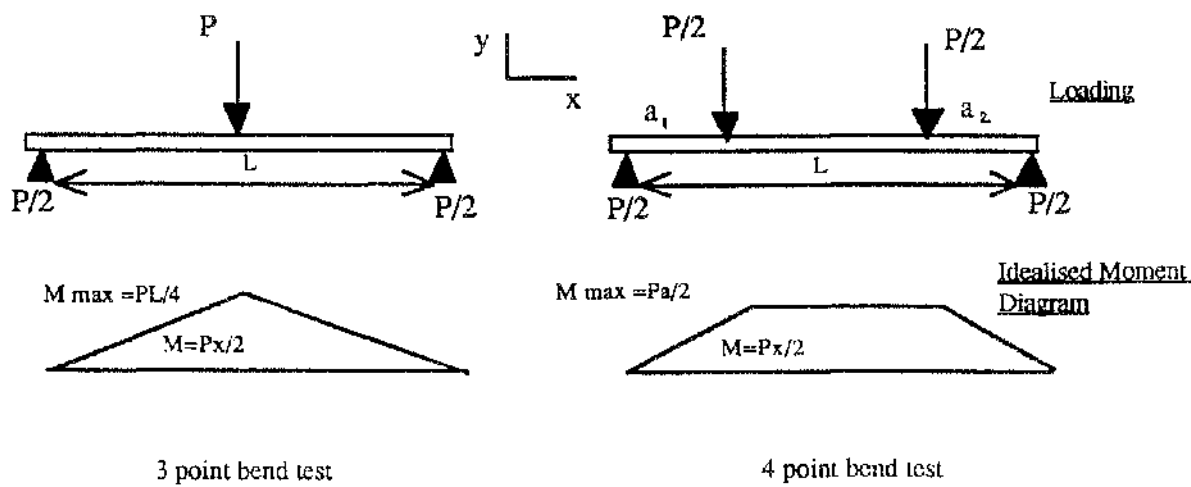


Fig 2.2.2 Ideal 3/4 point moment diagrams

These include first order effects that alter the stress field and deviate from simple bending theory, such as:

- Load Mislocation
- Wedging/Contact Stresses
- Twisting
- Friction

These effects can significantly alter the stress distribution in a specimen and induce an uncertainty that isn't acceptable (RR's cumulative tolerance was 2%) when ascertaining structural reliability. However if the above deviations are known or suspected, it is possible to account for them.

Load Mislocation

One of the obvious errors obtained in flexure testing of brittle materials is associated with incorrect positioning of the load points. If $a_1 \neq a_2$ the moment distribution acting over the centre will not be constant.

The resulting percentage error due to an eccentric load application is given by

$$\bar{e} = \left[\frac{1}{4} \left(\frac{1}{1 - \frac{a_1}{L}} \right) \left(\frac{1}{\frac{a_1}{L}} \right) - 1 \right] 100 \quad 2.2.1$$

where a_1 is generally half of the support span L (adopting the three point design results in much less error than the equivalent four point design). Assuming an eccentric load occurring at 36mm over a working span of 70mm for a 3 point bend rig for example, and using equation 2.2.1, gives:

$$\bar{e} = \left[\frac{1}{4} \left(\frac{1}{1 - \frac{36}{70}} \right) \left(\frac{1}{\frac{36}{70}} \right) - 1 \right] 100 = 0.059\%$$

Thus, to induce significant errors in the chosen specimen would require the load to be very eccentric. To ensure the support columns pitch was accurately verified, a shadow graph projector incorporating a magnified scaled mapping grid was used. Using the longitudinal and transverse micrometer heads, the pitch and angular misalignment can be established. For the design shown the pitch between the rollers was found to be $70\text{mm} \pm 0.005\text{mm}$.

The position of the push-rod in relation to the support members was measured in two ways. Firstly, bringing the push-rod down between the column supports, the gap on either side of the push-rods squared face and the support columns can be measured accurately by an internal micrometer. Since the transducers measuring probe is accurately aligned via the guide, bringing the base of the push-rods roller into contact with the probe gives visual confirmation. Alternatively, loading the push and support rollers into a 'soft' material will produce an indent which can be easily measured.

Wedging/Contact Stresses

Loads on flexure specimens, applied through small diameter rollers, can result in a substantial tensile stress contribution at the compressive side of the beam adjacent to the load points as shown in fig 2.2.3. Wedging is of the greatest concern in three-point loading, since an additional tensile bending stress is included on the tensile side of the beam. The actual stress will therefore deviate from the maximum tensile stress calculated from simple beam theory. On the compressive side, the maximum stress occurs a short distance either side of the centre.

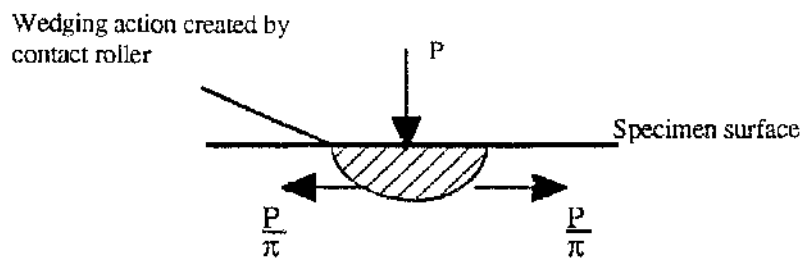


Fig 2.2.3 Wedging Action

The stress distortion due to wedging effects decays rapidly with axial distance from the loading points and is negligible at distances greater than the beam depth. The stress distribution around the loading nose is larger for composites than for isotropic materials. A general check on the maximum pressure between a roller and a flat surface for a given load is given by

$$\rho_{\max} = 0.59 \left(\frac{PE}{2br} \right)^{\frac{1}{2}} \quad 2.2.2$$

For three-point loading

$$\sigma_b = \frac{3PL}{2bd^2}$$

Substituting into eqn(2.2.2)

$$\frac{r}{d} > \frac{29}{L}$$

2.2.3

On this basis, for the bend fixture design, the radius of the rollers (r) should have been greater. However the formula assumes that the two materials have identical *properties* and that $E/\sigma_b = 1 \times 10^3$. This is not so here, and for the specific design considered, the diameter of 5mm is satisfactory.

Twisting

Twisting of the rollers or of the testpiece can lead to a net torque being produced, a potential source of error due to non-uniform load distribution along the width of the testpiece as shown in fig 2.2.4. This arises if the rectangular cross-section testpiece is skewed over it's length or if the contact lines along the specimen are not parallel. Although several equations have been produced (Baratta 1984), the net torque is difficult to establish. Allowing independent rotation of the loading contacts in the bend fixture and ensuring mating surfaces are true minimises any torsional stresses. To reduce such twisting, the test rigs bend fixtures incorporated independent rotation of the bottom rollers, a feature which was checked prior to each test using a fixed roller pitch angled jig. It however wasn't possible to implement independent rotation for the loading roller though it was envisaged that any error generated would be negligible.

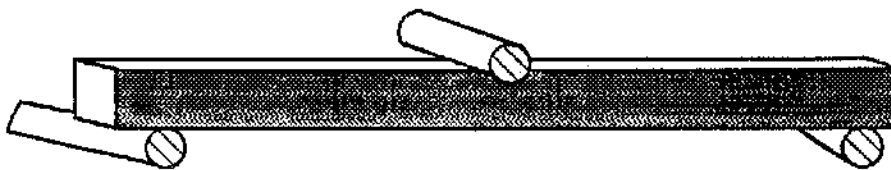


Fig 2.2.4 Twisting of rollers

Friction

For a surface load as assumed in three-point loading, horizontal line loads may contribute to the moment supplied by the vertical loads. These horizontal forces can arise from friction between the loading rollers and the testpiece because of the longitudinal surface strains induced during bending. When determining bend strength by simple beam theory, it is usual to assume that the supports and load points are frictionless; in reality they are not. To minimise frictional forces the bend fixture can be designed so that the rollers are freely allowed to rotate along the testpiece surface. If both roller and testpiece are hard a very low friction coefficient is attained. Both of these measures were adopted in the test rigs bend fixture.

2.2.3 Compression Testing

High compressive strength is a desirable property for some applications. Though useful for design purposes, compression testing does not often aid understanding of failure mechanisms. One of the major problems in testing materials with high compressive strengths is that, rather than break, the specimens tend to buckle, locally or globally. Another problem is that when the coupons are loaded by direct bearing on their ends, they tend to crush locally at low stress levels. Alignment is also a problem. A set of compression platens were manufactured for diametrical testing of the washer and cylinder sub-elements as shown in fig 2.2.5. The platens had recesses in which to insert the sub-elements and thus eliminate local crushing. Euler buckling is also eliminated by using short thick sub-elements. The support fixtures for the bend jig were interchangeable, to allow support of the bottom compression platen.

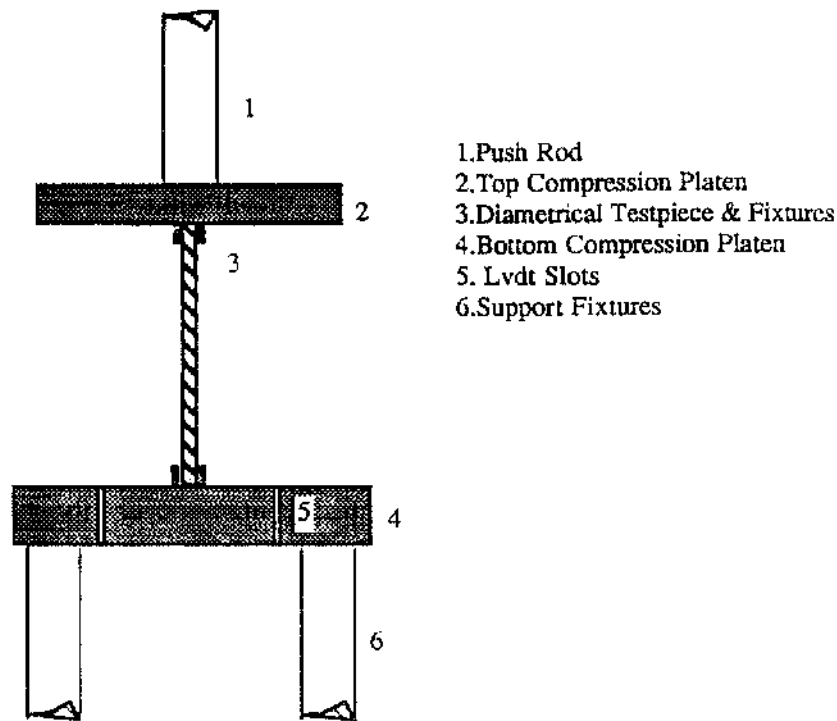


Fig 2.2.5 Compression platens for testing the washer and cylinder sub-elements

2.2.4 Heating System

The major design requirements for the heating system were that it could operate either in a short burst or thermal cycling mode. The heating facility had to be capable of achieving a uniform temperatures of 1273K (1000°C) in an air environment over the length of the testpiece to within a tolerance of ± 2 K of the set test temperature. The heat chamber also had to be versatile, in order to accommodate various testpieces, together with their loading jigs and fixtures, and fit into a universal test machine.

Existing methods of generating 1273K include conventional heating, which uses conduction or convection to transfer all the necessary energy to the component. In conventional heating the mechanism of energy transfer involves direct contact between the source and the component. Therefore, the energy can only be delivered to the surface of the component being heated. Recent alternatives, such as thermal radiation from infrared

lamps, differ in two important respects from the conventional modes: no medium is required and the energy transfer is proportional to the fourth power of the temperature of the bodies involved. Also, depending on the absorptivity of the material, the radiation may penetrate beneath the surface to deliver energy to the interior of the component. Several suitable methods for meeting the design requirements were investigated, eg:

- a) Radiation heating using resistance elements eg silicon carbide, molybdenum disilicide etc.
- b) Induction heating from an RF generator
- c) Radiation heating by IR lamps ("optical heating")

a).Resistance Heating

Conventional base metal heater wires such as molybdenum, tungsten and "Kanthal" have been successfully used in heating systems up to +1273K. A proven method for steady state operation, they are however not particularly suitable for generating the fast heating rates required for thermal transient tests. As a contingency measure, a 5kW three-zone cylindrical-split furnace was manufactured by Mayes Ltd to GU specifications. The furnace had a heated length of 380mm and a bore diameter of 125mm. A maximum temperature of 1273K is generated by three independent Kanthal resistance-fed zones controlled by a triple thyristor regulator and a proportional temperature controller. The resistance furnace and temperature control unit are shown in Appendix A1.

b).Induction Heating

Induction heating is relatively clean and efficient with much of the power going directly into the workpiece. Heating times are usually short- a few minutes for typical specimen sizes. The temperature profile across the testpiece can be tailored by varying the number,

diameter and spacing of the induction coil loops.

An existing but unused induction generator was recommissioned. This was estimated to have a power consumption of 12-15kW, at a radio frequency of 470kHz. Both metallic and monolithic ceramic were successfully heated. A circular water-cooled coil having a diameter of 75mm, with 5 turns separated by an average space of 7mm was initially used. With small metallic testpieces, temperatures of 1673K were achieved.

Direct induction heating of ceramic materials, which are not electrically conducting, is not feasible. To overcome this, a conductive "susceptor" is inserted within the coil and closely coupled to the testpiece. A metallic or nonmetallic susceptor can be used provided that it can be heated above the test temperature. Temperatures of 1273K were demonstrated on silicon carbide sections using a metallic tube as susceptor. A prototype design based on the dimensions of the sub-element geometries including fixtures was manufactured. A rectangular copper cooling coil grouped the insulating material and rectangular metallic susceptor. The induction generator and prototype design is shown in Appendix A1.

c).Optical Heating

Infrared lamps generally consist of a filament of tungsten or nickel-chromium alloy which can be heated electrically to a temperature substantially above the desired test temperature. These tubular emitters provide a fast, controllable method of heating with the temperature level determined by the applied voltage. To verify the heating capabilities of the IR lamps, six 'long' vertical 1kW lamps were first used to generate a heated zone of length 300mm with a working diameter of 100mm. The demonstration lamps shown in fig 2.2.6, came supplied with their own lamp holders and specular anodised aluminium reflectors. The lamps were positioned axisymmetrically around a small metallic testpiece to create a closed uninsulated heat chamber. Power consumption of 3kW and 6kW gave

temperatures of 1073K and 1273K respectively. The time taken to reach a design temperature of 1273K was relatively short but oxidisation occurred on the uncooled reflectors if the maximum temperature was held longer than 120 seconds. However the tests did verify the lamps capabilities of rapidly reaching the design temperature for a short burst mode of operation.

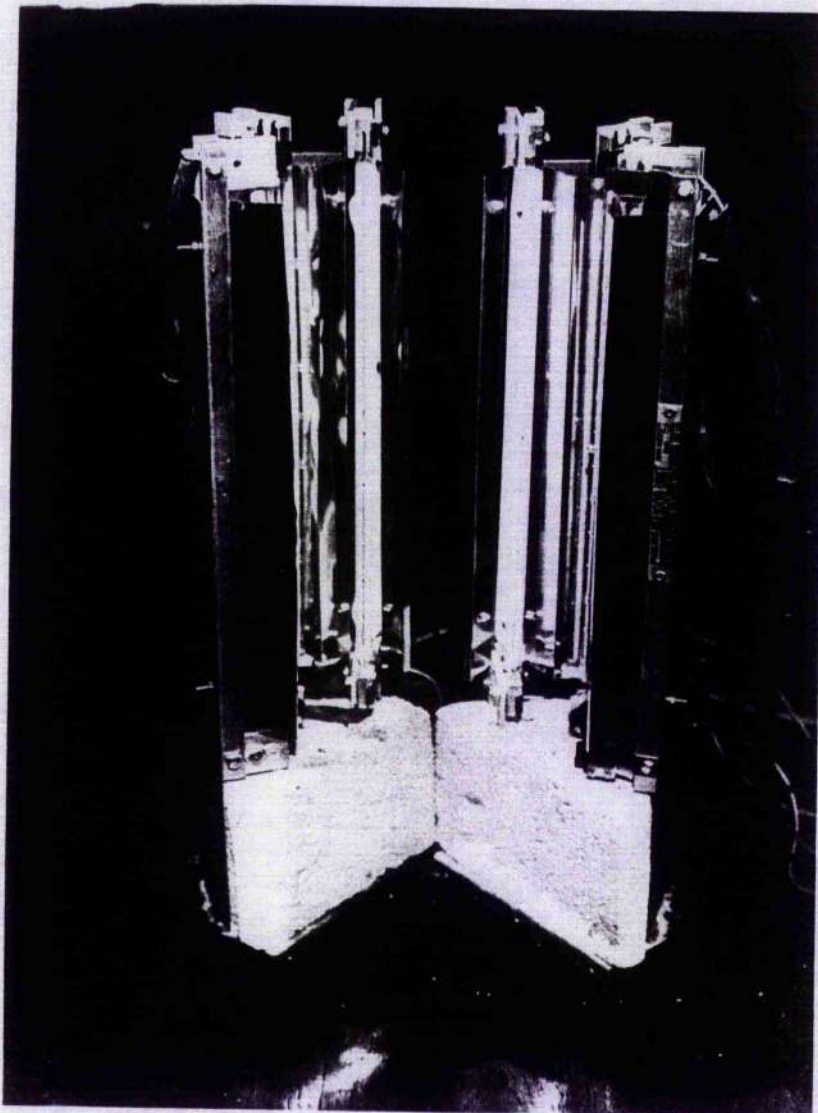


Fig 2.2.6 Vertical Heat Lamps

Infrared lamps have been successfully used in the chemical industry for curing of polyimides and in the bottling process. Stephanie & Rickerl (1991) developed a polyimide curing process using radiant tube technology and cut down the cycle time from hours to minutes. In the bottle process, a reheat time of seconds was vital in improving the large volume production output. The emitters used are available in a wide range of power, sizes and styles (Research Inc) which can generate extremely fast temperature rates. This mode of heat transfer was chosen for the heating system in the current work.

2.2.5 Radiation Heating by Infra-Red Heat Lamps

Radiation is the transfer of heat from a hot body to a cooler body without appreciable heating of the intervening space, the energy being transferred in the form of electromagnetic waves. Electromagnetic waves are propagated at a speed of $3 \times 10^8 \text{ms}^{-1}$, by the interaction of magnetic and electrostatic fields and, according to their wavelengths, produce widely differing effects. The longer wavelengths ($\sim 2\text{km}$) are radio waves, the extremely short wavelengths (10^{-11}m) are gamma rays.

About halfway between these two extremes ($0.4\mu\text{m}$ to $0.75\mu\text{m}$) lies the range of wavelengths by which heat is transmitted. Since this radiation occupies a range of frequencies just below that of red light, it is often referred to as "infrared".

Infra-red radiation, like light, travels in straight lines in a homogeneous medium and obeys the ordinary rules of photometry. That is, the intensity of the radiation received on a body from a heat source varies inversely as the square of the distance from the body to source and is proportional to the cosine of the angle of incidence on the body. Infra-red radiation, also like light, is absorbed by dark, rough surfaces and reflected by light smooth surfaces. The efficiency of radiation transfer depends on the boundary conditions, eg, the temperature and emissivity of the surrounding walls and the target where the

transfer of heat is desired. The total emissive power, E_p of a blackbody is given by the Stefan-Boltzmann equation as

$$E_p = \sigma_{sb} T^4 \quad 2.2.4$$

where σ_{sb} , the Stefan-Boltzmann constant, is $5.6697 \times 10^{-8} \text{ W/m}^2 \cdot \text{K}^4$

In practice, bodies are not 'black'. For real sources, more commonly known as gray bodies, E is less than that of a black body. A polished metal surface, for example, reflects most of the radiation falling on it. Hence the equation must be modified by the inclusion of a factor which takes account of this and is termed emissivity (ϵ). Equation (2.2.4) also assumes that each body receives all the radiation from the other but, unless one body completely encloses the other, this will not be the case. Account must be taken of the extent to which one object 'sees' the other. The calculation of such "viewfactors" can be rather complex.

The rate of radiation heat flow $\frac{\partial q}{\partial t}$ between two gray bodies thus becomes

$$\frac{\partial q}{\partial t} = \epsilon A_1 F_{12} \sigma (T_1^4 - T_2^4) \quad 2.2.5$$

where ϵ is the emissivity of the radiated body, A_1 is the surface area of the radiating source (lamp), F_{12} is the viewfactor, and T_1 is the absolute temperature of the source (lamp temperatures were 2000-2500K) and T_2 is temperature of the body being heated (the load). The viewfactor is a measure of how much radiation from surface 1 reaches surface 2. If surface 1 is the lamp and surface 2 the load, the viewfactor will be dependent on reflector and lamp geometry.

Reflection of radiant thermal energy from a surface can be described with the assistance of two ideal diagrams shown in fig 2.2.7.

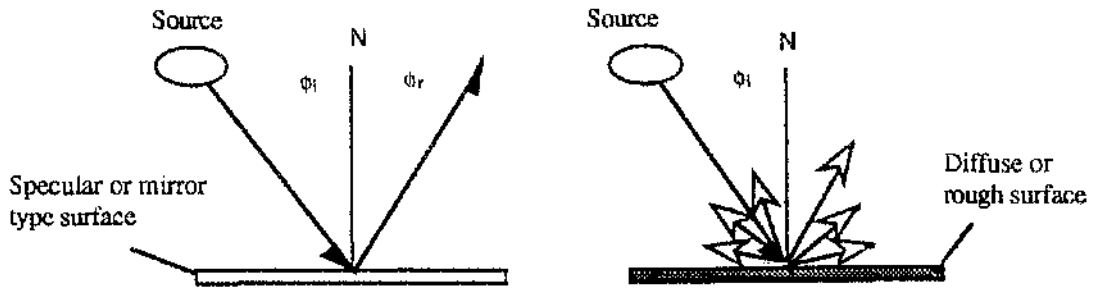


Fig 2.2.7 Specular and Diffuse surfaces

The ideal specular reflector is shown in fig 2.2.7(a) in which the angle of incidence ϕ_i is equal to the reflected angle ray ϕ_r . For the diffuse reflector, fig 2.2.7(b) the magnitude of the reflected energy in a specific direction ϕ_r , is proportional to the cosine of ϕ_r , ϕ_r being measured from the normal N.

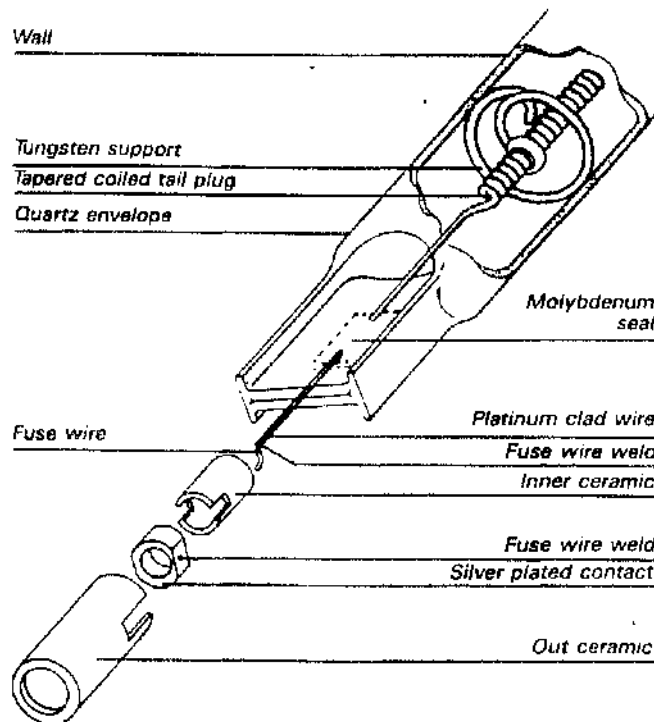


Fig 2.2.8 Design of infra-red lamp

Infra-red lamps usually consist of a tubular quartz envelope filled with an inert gas, such as argon or halogen, having a tungsten wire filament that emits radiant energy in proportion to the applied voltage. The low mass wire is supported along its length by tantalum disks or tungsten wire to prevent contact with the quartz envelope as shown in fig 2.2.8. During heating, large temperature differences exist between the filament and the component but within a few seconds of being turned on, full radiant energy is transmitted to the part. The limiting factor in lamp energy output is the end seal that supports the filament, contains the inert gas and provides for an external power connection. Standard seals are limited to a temperature of approximately 616K. Operation above this level leads to oxidation, resistance heating and eventual burnout. The lamps are generally recommended to be horizontally positioned for maximum life, though for short periods of use, the lamps may be placed vertically. Fig 2.2.9 shows typical lamp performance data.

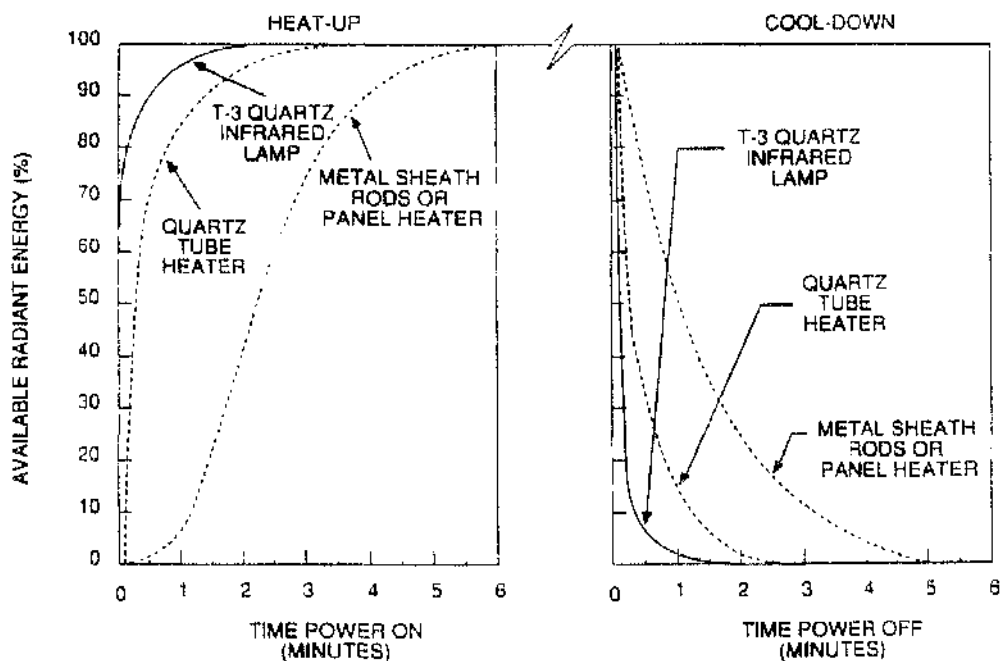


Fig 2.2.9 IR lamp performance rates

2.2.6 Vertical Prototype Designs

The lamps used in the concept demonstrator were 'long' in comparison to the sub-element testpieces and were replaced in the prototype by shorter lamps having similar specification but operating on half the voltage (120V). Two initial designs for a prototype heat chamber were proposed:

- a) IR lamps inserted in a specular parabolic surface around a water cooled aluminium housing
- b) IR lamps axisymmetrically positioned and mounted onto a uncooled reflective surface.

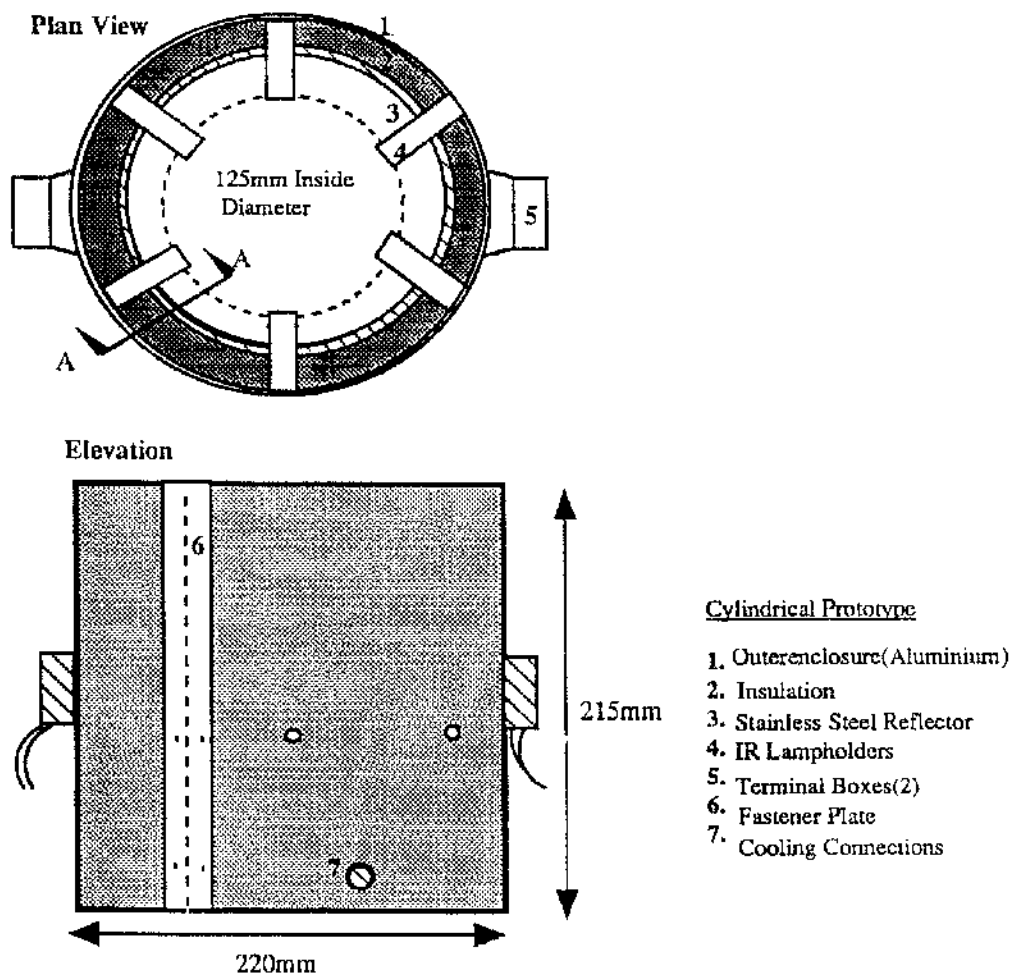
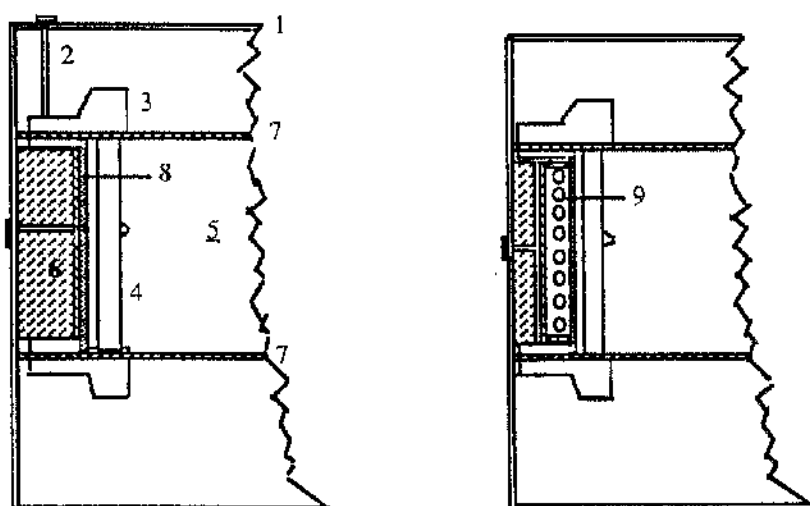


Fig 2.2.10 Cylindrical Prototype Furnace (Lamps, Vertical Burning Position)

The latter design offers simplicity in manufacture and, based on advice from Severn Furnaces Ltd, was used as the first prototype. Since the sub-element testpieces would have a maximum dimension of 100mm, an uninsulated prototype heat chamber was designed as shown in fig 2.2.10. The heat chamber had a cavity of approx 1 litre (100mmx100mm), capable of housing each geometric testpiece and their necessary jigs and fixtures. Lamps were axisymmetrically positioned vertically around a cylindrical stainless steel specular reflector.



uncooled heat chamber

cooled heat chamber

1. outer casing
2. spacer(6)
3. ceramic lampholder
4. IR heat lamp Lamps(6)x500W=3KW
5. heat chamber Volume=1.4lLitres, Temperature=1000C
6. kaowool insulation
7. inner enclosure
8. stainless steel reflector
9. cooling coils

Fig 2.2.11 Quarter Section A-A -Redesign of the heat chamber interior to include cooling

A temperature of 1273K was achieved on a dummy metallic testpiece but again this led to extreme discolouring and oxidizing of the specular reflectors and lamp contacts. The lamp holders, fastened onto the reflector and steel spacers, also allowed heat to be transferred

via conduction to the outer casing. The amount of conductive heat transfer through the reflector wall to the outer aluminium casing softened the original electrical insulation support grommets, causing concern for short circuiting. To solve these problems, a cooling water coil and alumina tubing, housed in modified brass compression fittings used as grommets, were added to the prototype as shown in fig 2.2.11. Also, to minimise heat conduction to the cabling in the outer casing, a circular terminal channel was built around the outer casing perimeter with an air gap of 10mm between adjacent faces. Contact between the cooling coil and reflector however wasn't ideal, due to the method of fastening. Fig 2.2.12 shows the uncooled cylindrical prototype furnace with the top and bottom covers removed.

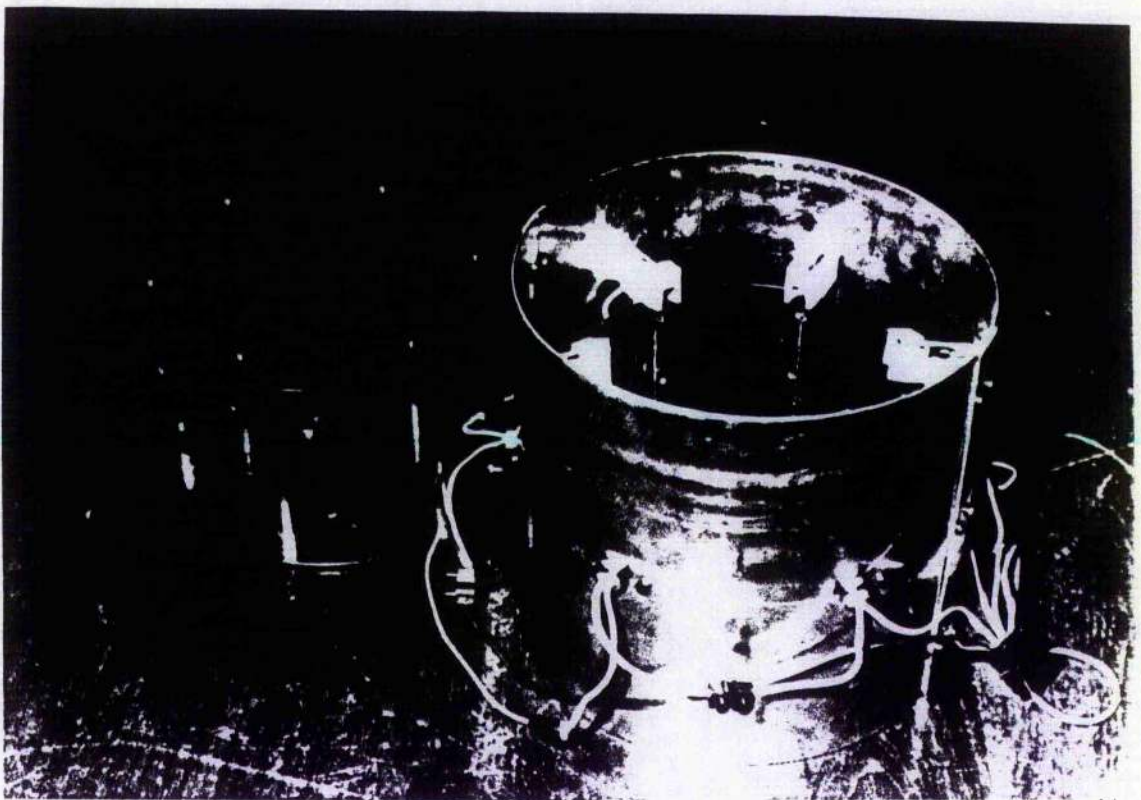


Fig 2.2.12 Vertical Cylindrical Furnace

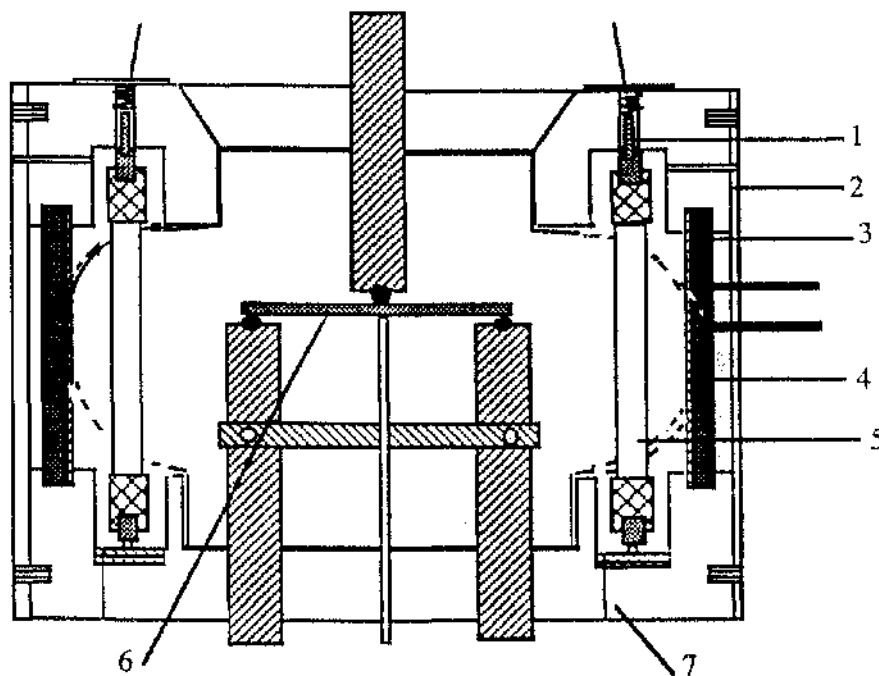
A better option would use a welded joint instead of set-pins but the latter allowed development and testing of the prototype to continue. An inner cooling coil was also inserted to the top surface of the heat chamber to prevent buckling of the outer casing. Tests achieved temperatures of 973K in around 90 seconds and 1273K in about 300 seconds but operating the furnace on full power created thermal shocking and cracking of the ceramic lamp ends. A more moderate temperature ramp could be achieved via a temperature controller. However, maintaining a continuous working temperature of 1273K for twenty minutes (as required for the materials test) proved impossible since oxidation of the lamp connectors led to local hot spots and eventual arcing. As the lamps are arranged in pairs (each operable at 120V) failure of one lamp caused its partner to switch off, further reducing the heat generated inside the chamber.

When the lamp connectors were stripped and examined, it was apparent that failure to maintain contact stemmed from annealing of the pop-rivet on the holder which acts as a pivot for the spring steel which contacts the lamp ends. The rivets were bored out and replaced with a stiffer fastener. Insulation was also inserted into the gap between the lamp holders and the contacts to increase the time before the contacts reached the critical temperature for failure. These modifications resulted in an improvement in the running time of several minutes, but the problem remained of not achieving the proposed test time condition. The solution was to cool the lamp contacts. Proposed methods of cooling the lamp contacts included;

- a) Individually enclosing the lamps in a transparent silica or quartz envelope and purging with compressed air;
- b) Inserting a single envelope of the same material and purging the cavity between this and the outer wall with compressed air.

The latter was preferred due to the difficulty of providing a fully enclosed envelope for the lamps and holders. To improve cooling of the reflector, the cooling coil was replaced with a copper water jacket. The reflector then acts as an inner sleeve, the ends kept together by compression from the inner cavity wall of the jacket. This allows the reflector to be easily replaced.

An alternative vertical redesign was later proposed. It incorporated the existing water jacket and specular reflector, housed in an aluminium body through which water and air flowed to keep the structure and lamp contacts cool during operation, as shown in fig 2.2.13. However the final vertical heat chamber was never manufactured.



Final Vertical Prototype Design

- 1. Electrical Contacts
Cooled Inside Al Body
- 2. Aluminium Housing
- 3. Water Jacket
- 4. Reflector
- 5. IR Lamp
- 6. Testpiece And Fixtures
- 7. Air Supplies

Fig 2.2.13 Final Vertical Prototype Design

2.2.7 Horizontal Prototype Design

The decision to abandon the initially attractive "vertical heating" array was made in the light of the following factors:

- a). Theoretical comparison of two modes (vertical and horizontal) favoured the horizontal design, which is more compact.
- b). This compact design reduces the amount of heat needed to achieve the working temperature, since the thermal mass inside the heat zone has been minimised.
- c). The tendency of the hot gases to rise vertically and flow over and damage the lamp contacts is reduced if the lamps are horizontal.
- d). A working model used for tensile testing of ceramic composites at elevated temperatures existed at RR Bristol (Hillyer).

Given these factors, and the empirical design experience gained in using the lamps so far, emphasis was shifted to designing an optical horizontal heating array. To complement the empirical design, theoretical calculations were done, based on work undertaken by Ramamurphy et al (1990) and Jamaluddin and Fiveland (1990). An exact solution to the radiation heating problem would be very complex but some simplification is possible. The radiosity method can be applied to the radiation heat exchange between the load, the furnace walls and the radiant heat lamps. The calculations are based on a known heat flux on the outer surfaces of the infra-red heat lamps, with known surface temperatures on the load and furnace walls. For each internal surface of the furnace and the load the radiosity J (where J is the sum of the emitted and the reflected radiant energy fluxes from a surface) can be expressed by;

$$\sum_{j=1}^Z [\delta_{kj} - (1 - \epsilon_k) F_{k-j}] J_j = \epsilon_k \sigma T_k^4, \quad 1 \leq k \leq Z - T \quad 2.2.6$$

For the heat lamps, the radiosity equation is;

$$\sum_{j=1}^Z [\delta_{kj} - F_{k-j}] J_j = q_{\text{tot},k} \quad Z-T \leq k \leq Z \quad 2.2.7$$

where Z is the number of heat zones, T number of radiant tubes, δ_{kj} is the Kronecker delta ($\delta=0, k \neq j; 1, k=j$), ϵ is emissivity, F_{k-j} is a configuration factor between the k-th and j-th surfaces, J is radiosity at a surface and k is thermal conductivity. The furnace dimensions and parameters used as input data are listed in table 2.2.7.

Furnace dimensions

Length (L)	135mm	Lamp Heat Flux	55000W/m ²
Width(W)	25mm	Lamp emissivity	0.8
Height(H)	170mm	Heat transfer coefficient	1W/m ² K
Ambient Temperature	25C	Load emissivity	0.7
Furnace walls emissivity	0.1	No of Heat Lamps	8

Table 2.2.7

Using equations (2.2.6) and (2.2.7) the radiosities at each surface can be established from

$$q_{\text{tot},k} = \frac{\epsilon_K}{(1-\epsilon_K)} [\sigma T_K^4 - J_k] + h_k [T_K - T_{g,K}] \quad 2.2.8$$

From equation (2.2.8) the temperature of the heat lamps T_K can be obtained by rearranging the terms. The heat losses through the furnace walls q_w can be calculated under steady state one dimensional conditions using Fourier's law of heat conduction, given as

$$q_w = -k \frac{\partial T}{\partial x} \quad 2.2.9$$

The split horizontal radiant furnace is shown schematically in fig 2.2.14. Since the load is heated symmetrically from the top and bottom, only one section need be modelled. The furnace houses a total of 8 infrared lamps (4 on each bank) equally spaced along the furnaces length. To verify the theoretical calculations, thermocouples were placed at several key positions.

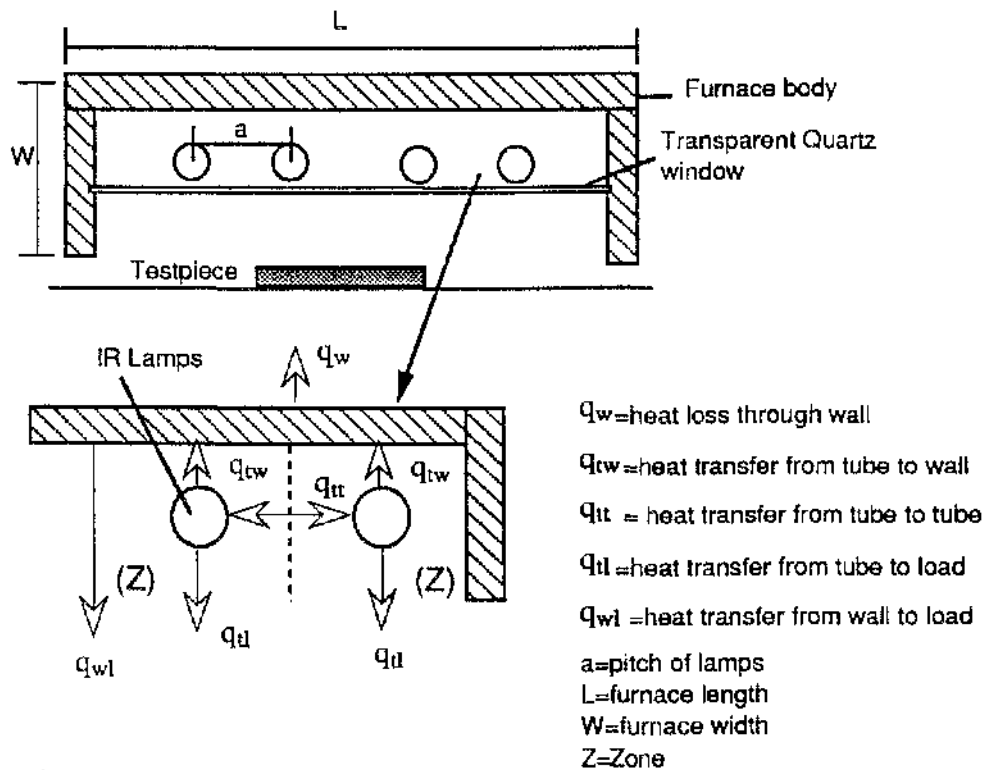
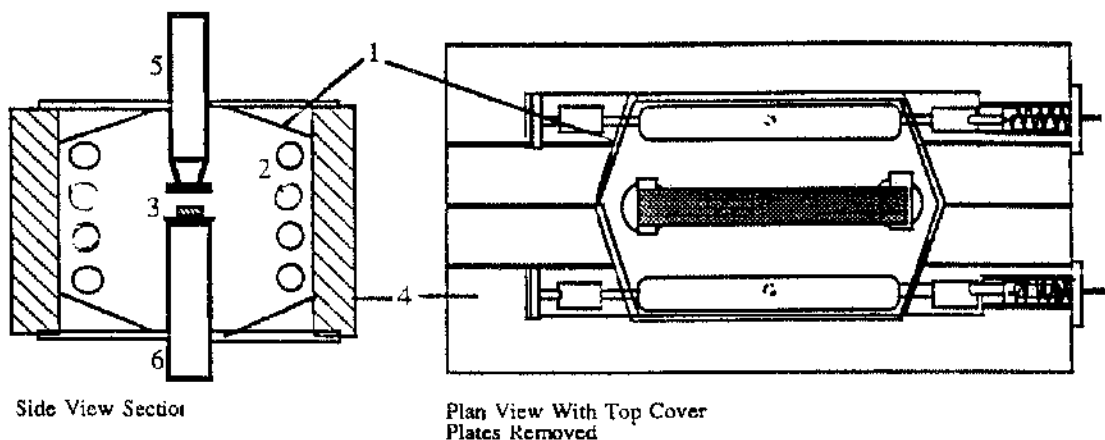


Fig 2.2.14 IR heat distribution inside horizontal prototype furnace

The horizontal furnace was manufactured in two symmetrical copper sections, mated around the testpiece and fixtures, with top and bottom cover plates forming a closed chamber. The compact split design means that the specimens surface is more accessible for the attachment of the control and measurement transducers. Each symmetrical section of the furnace is further split into two sections to ease machining, as shown in fig 2.2.15.

The lower part contains the electrical contacts and services, with the top part having the necessary breadth to accommodate the flexure testpieces and loading fixtures. Cold water from the workshop main was adequate to maintain a safe temperature in the copper block and reflector. Cooling is enabled by a cavity in the lower copper structure. The lamp contacts are both conductively and convectively cooled, the latter via compressed air channelled under the aluminium reflector from a central inlet port.

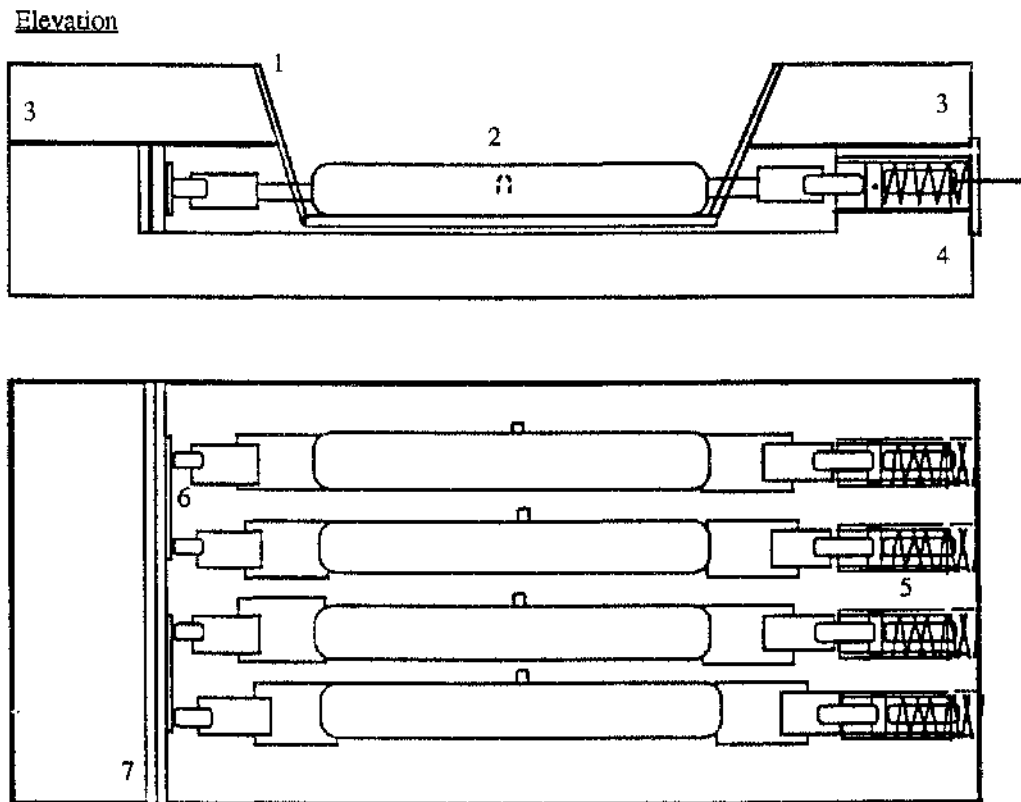


1. Top/Bottom Copper Plates With Aluminium Reflectors
2. IR Heat Lamps
3. Testpiece
4. Copper Furnace Body
5. Push-rod
6. Support Column

Fig 2.2.15 Operating view of split horizontal furnace

Exhaust air is allowed to escape from the lamp contacts into the heat zone and exit via the gap between the fixtures and the top and bottom cover plates. Anodised aluminium reflectors are attached to the base of the copper blocks using epoxy resin, while the side reflectors are removable to allow the lamps to be inserted. A close fit around the lamp contacts by the reflector minimises reradiation heating of the contacts. The design has a power rating ranging from 4kW-8kW.

Assuming that the thermal mass inside the heat zone behaves as a black-body, a power consumption of 4kW is theoretically sufficient to achieve the working temperature of 1273K in the flexure testpieces. This was proven experimentally. Keeping the cavity of the furnace compact, with reflector walls inclined around the testpiece overcomes the short-comings in the heated length, the specular walls reflecting radiant energy over the entire workpiece as shown in fig 2.2.16 and 2.2.17.



Plan View Of The Lamps Orientation
With Top Section Removed

- 1.Reflector
- 2.IR Lamp Array
- 3.Side Surfaces
- 4.Main Body
- 5. Spring Contacts
- 6. Dual Electrical Contacts
- 7. Insulation

Fig 2.2.16 Lamp orientation of split horizontal furnace

Trials demonstrated the furnace was repeatedly capable of ramping the workpiece temperature from ambient to 1273K in 10min and soaking at this temperature for a further 10min. The furnace was initially placed around a metallic testpiece geometrically similar to the bar sub-element, together with the support and loading fixtures. This mimics the total thermal mass that will be heated in the proposed isothermal test. The trials were satisfactory, apart from the tendency of the side reflectors to lose adhesion to the copper structure. This was attributed to irregularities between the two material interfaces creating improper bonding, exacerbated by differential expansion due to the different thermal expansion coefficients of each material.

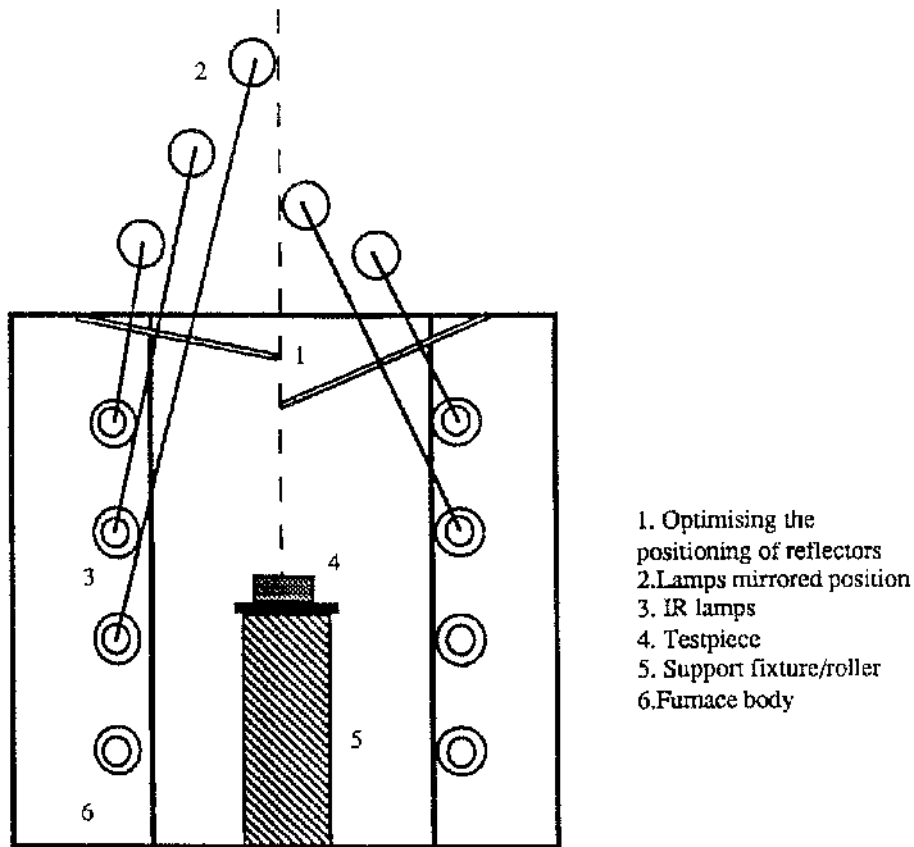


Fig 2.2.17 Radiant focusing onto the testpiece

The situation was slightly improved by the use of a high temperature adhesive mixed with particles of copper but the problem was only finally solved by a redesign of the side

reflectors. The furnace used 2kW for each array, but has the potential to achieve greater elevated temperatures by using more power, (the furnace was initially designed to operate from 4kW-8kW). Evidence in support of this theoretical prediction was given on initial trials involving a small thermal mass, equivalent to the bar sub-element, which reached temperatures of +1573K. The practicality of this optical method at generating very fast heating rates is thus proven.

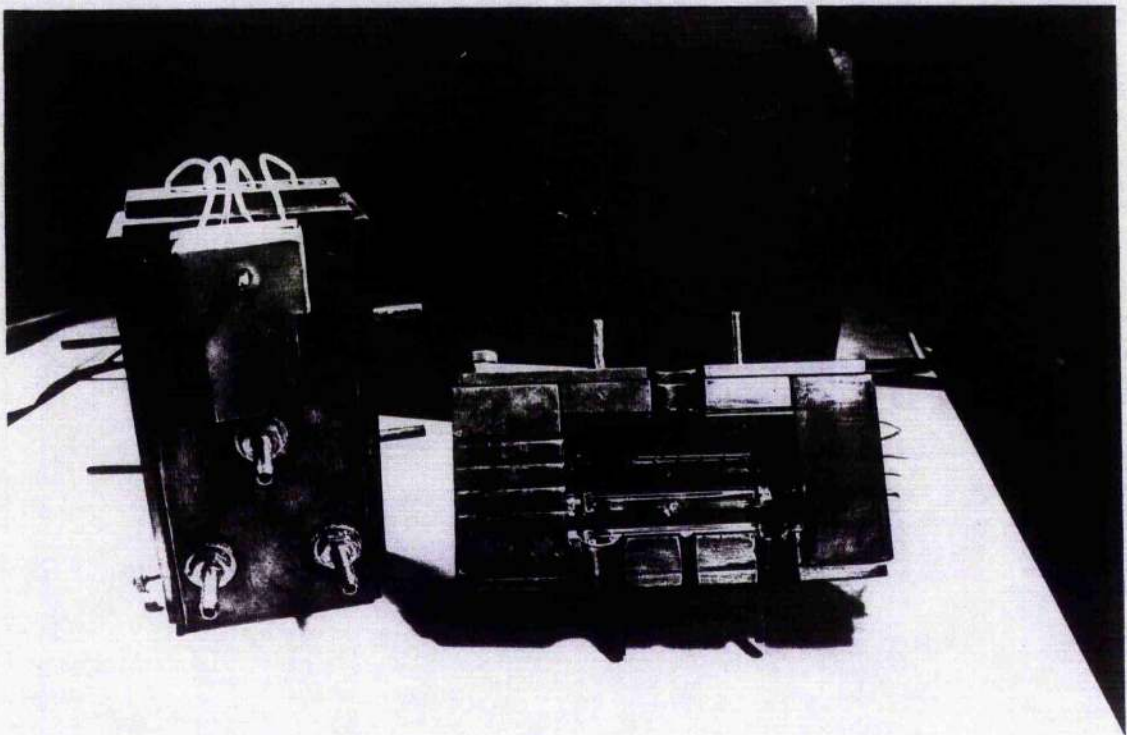


Fig 2.2.18 Split Horizontal Furnace

2.2.8 Calibration Of The Horizontal Prototype

It is difficult to measure the surface temperature of ceramics in a high temperature environment using thermocouples. This is partly due to the difficulty of processing ceramics and affixing thermocouples. Even if they could be fitted successfully, the

protruding thermocouples would require shielding from direct radiation heating, which would otherwise cause gross errors in temperature measurement. Surface temperatures of ceramics at fixed points in a high temperature environment were measured by making holes in the ceramic testpiece into which thermocouples were embedded. The embedded thermocouples can be fixed with Al_2O_3 -type filling materials. Since the manner in which the testpiece is heated is symmetrical, only one side of the testpiece need be instrumented.

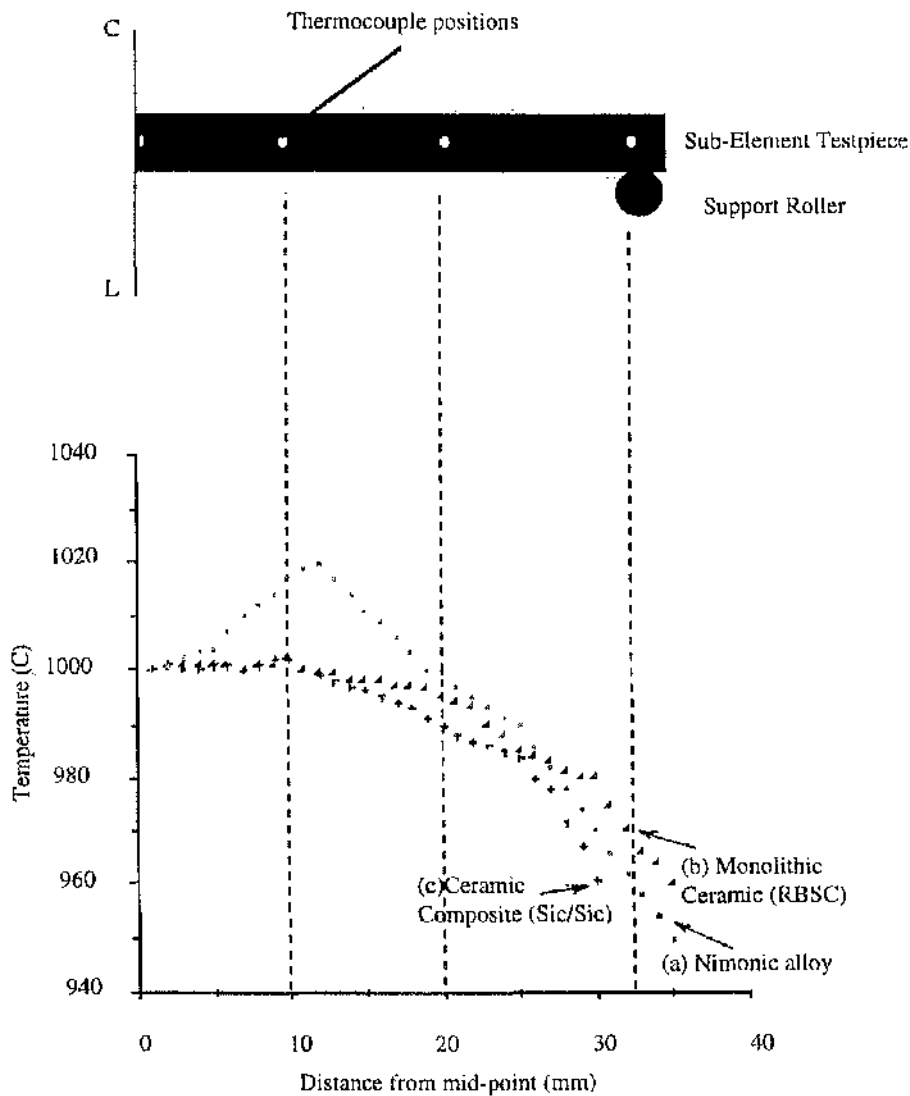


Fig 2.2.19 Temperature gradients along the testpiece

Calibration of the small optical furnace was done with embedded TypeK (chromel/alumel) thermocouples placed in a steel specimen at a pitch of 12.5mm, 25mm and 35mm from the centre. The testpiece was ramped to a set point (sp) temperature of 1273K at a rate of 127K/min, the sp temperature being controlled via a PID temperature controller.

Temperature monitoring of the metallic testpieces, after a short soaking period, indicated the temperature gradient shown in fig 2.2.19 graph(a). This shows the temperature increased by +20K at 12.5mm from the control position, remaining uniform ± 1 K in the region from 12.5mm-25mm before descending by 45K at 35mm from the sp position. The symmetric temperature profile was caused by the push rod and support columns extracting heat via conduction from the heat chamber, with the central push rod also casting a 'shadow' over the central region. Nimonic bars coated with thermal indicating paints (calibration TP11) were used as a check on the thermocouple readings. The temperature profile for a SiC/SiC specimen with holes of the same pitch as above, was similar to that generated on the metallic testpieces, fig 2.2.19 graph(c). Methods to reduce the temperature gradient included:

- a). Preventing the lamp cooling air supply from entering the heat chamber, by providing alternative outlets.
- b). Extending the duration of the soak period.
- c). Reducing the push-rods thermal mass
- d). Replacing the nimonic rollers with rollers of lower thermal conductivity.
- e). Replacing the specular top/bottom reflectors with diffuse surfaces.

Since the largest gradient existed near the end rollers, the effects of the lamp cooling air flow entering the heat chamber near the testpiece end seemed significant. Rerouting the air flow away from the chamber, by inserting air outlets in the top and bottom plates,

together with extending the soaking period, was tried. This gave little improvement, emphasizing that convection losses were negligible in comparison to the heat gained by radiation.

Calculations for the uniaxial flexure test predicted that a load of a few hundred Newtons would be required to fracture the corresponding sub-elements (with the exception of the washer and cylinder sub-elements). The existing design of the Nimonic push-rod was therefore extremely conservative. Taking account of the materials yield strength at 1273K and of buckling showed that the section could be reduced to a few millimetres. A factor of safety was applied and the cross section was redesigned to give a reduction of 40% in mass. This also reduced the heat loss by conduction. The nimonic rollers were replaced with two monolithic ceramic materials, viz Silicon Nitride and Recrystallised Alumina, which have better insulating qualities than the Nimonic alloy. Tests incorporating the reduced push-rod and ceramic rollers showed an improvement in the temperature profile over the central portion of the testpiece, the temperature being steady to within a few degrees up to 25mm from the centre, as shown in fig 2.2.19 graph(b). Both the ceramic rollers gave similar performances so SiN was chosen on the basis of its better mechanical properties.

Inserting 'rough' surfaces of refractory materials in the top sections of the furnace in order to reflect the radiant heat diffusely to the testpiece was tried but with little effect. In short, to completely eliminate the thermal gradient and produce a uniform steady state temperature over the entire testpiece may be impractical¹, however computational analyses (McCafferty, 1993) predict that microcracking and damage will be restricted to a region no greater than 2/3 of the half span and so thermal uniformity over a distance of 23.3mm from mid-point may be satisfactory. Attention was therefore focused on a 'gauge length' of ± 25 mm from mid-point. With the modifications above, 25mm from the set-

¹ Heated length of IR lamp should ideally be longer than the testpiece

point (sp) position, from which the temperature control is taken, shows +15K above the mid-point temperature given a tolerance of $\pm 7.5\%$ of sp temperature.

The small optical furnace, although not fulfilling the RR requirement entirely, continued to be used for developing and investigating optical heating technology

2.2.9 Final Horizontal Furnace Design

Efforts to create a uniform temperature of 1000C in a air environment, failed to achieve the acceptable temperature tolerance of $\pm 2K$ required for testing the sub-element testpieces. This failure was attributed to the heated length of the Infra-red heat lamps being 'short' in comparison to the length of the bar sub-elements. Although this was appreciated in advance, it had been envisaged that this would be overcome, at the expense of a longer soak period, by keeping the cavity of the furnace compact, with specular reflector walls inclined around the testpiece. Unfortunately the heat loss via the push rod and support fixtures still remained significant even after their thermal mass had been substantially reduced. Arguments as to whether a $\pm 7.5K$ temperature gradient could be tolerated remain unsolved and as a failsafe a larger furnace was designed. The experience gained from the small optical furnace allowed several improvements to be incorporated into the 'larger' furnace, eg:

- a). Insertion of a transparent quartz plate in front of the lamp rows to allow cool air to flow over the lamps and contacts and enhance the working life and performance of the lamps (maximum operating temperature of the heat lamps is quoted as 1500K in an uncooled state)
- b). Chrome plating of the interior walls to eliminate any need to bond reflectors onto the furnace body.
- c). 'Saffil' high temperature insulating board to remove the need for the top and

bottom sections of the furnace to be modified to suit different testpieces. (If the quartz plates are in operation, these will also act as diffuse reflectors). Figure 2.2.20 shows the interior view of the 'large' optical furnace

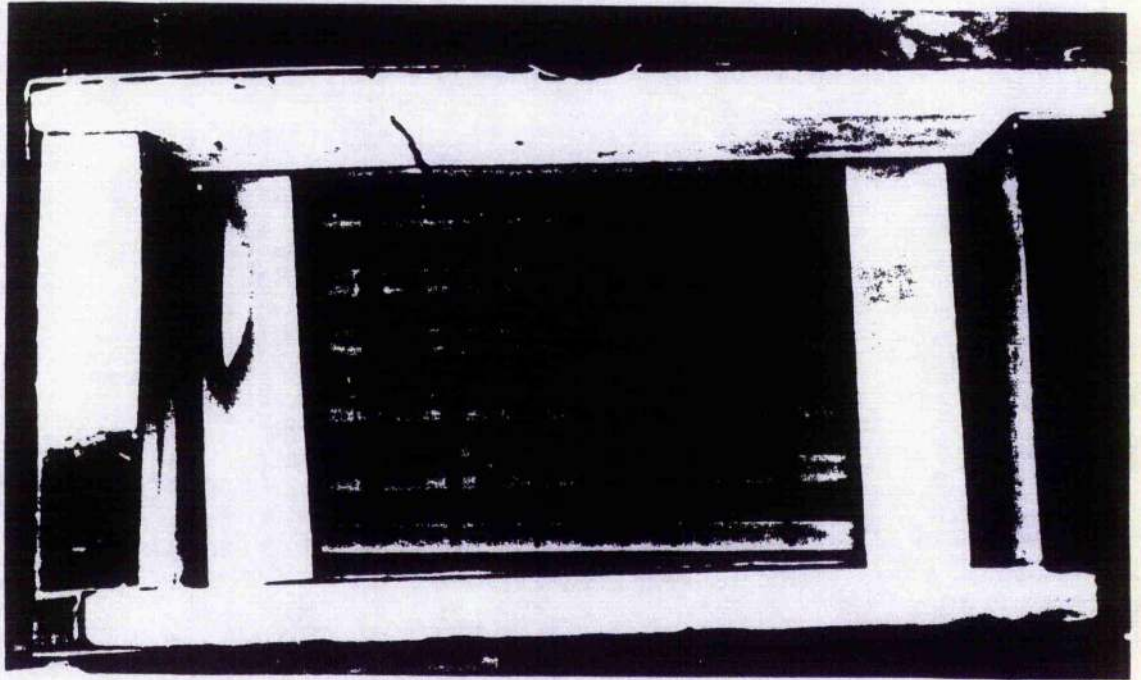


Fig 2.2.20 The 'large' optical furnace showing the lamps enclosed with a quartz window and surrounded with Saffil insulation

Calibration of the large optical furnace design made use of a "dummy" piece of cut-off SiC/SiC material for enclosing the control sensor. This eliminates the need to implant sensors into the actual testpiece. Tests using the dummy piece (placed close to the mid-point position of the testpiece) and embedded sensors, showed the two monitoring methods to be in agreement with each other (see section 2.3.2). Fig 2.2.21 shows the optical furnace located on the test-rig.

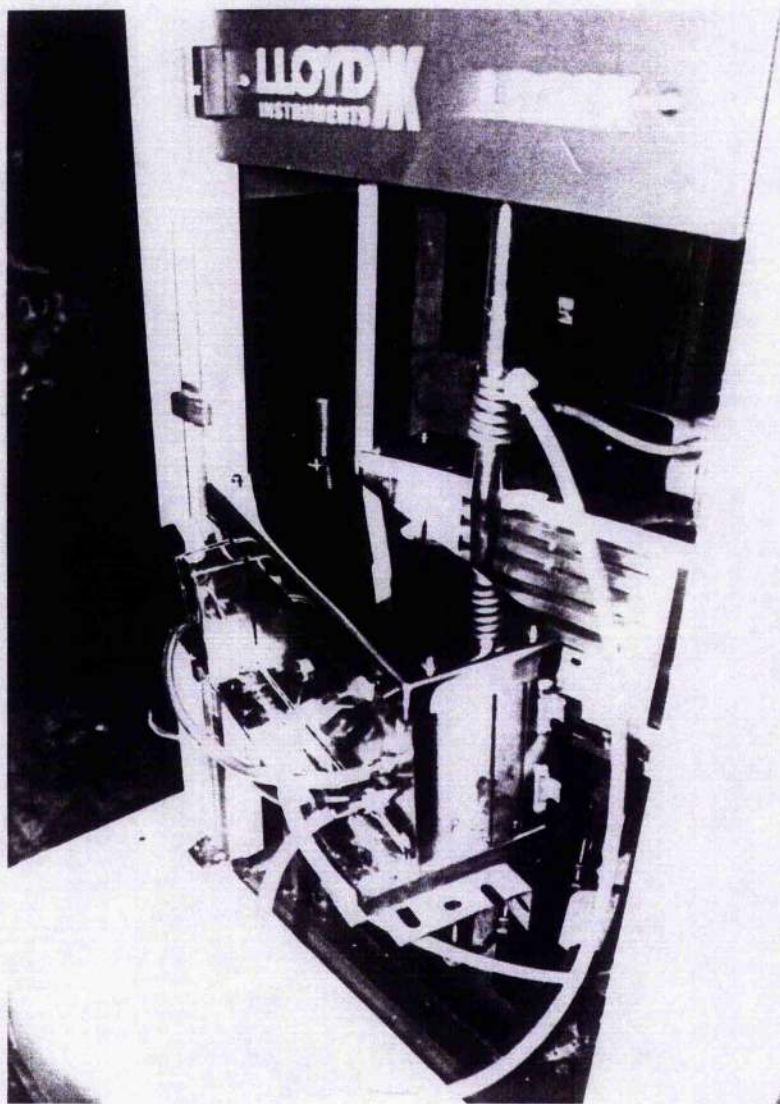


Fig 2.2.21 Optical furnace on the test rig

2.3 Instrumentation & Control

Instrumentation is required both to determine the thermomechanical state of the testpiece and to provide feedback for the closed loop control of the loading jig. Since the thermomechanical tests to be conducted were generally 'simple' flexure and compression tests, the mechanical variables could be measured and controlled by conventional load cells and LVDT's (which must obviously be located outside the furnace cavity). At ambient temperatures, this is a routine matter but both the absolute levels and temporal gradients of temperature required by the test program produce special difficulties. A number of different technologies were therefore considered for temperature measurement at 1273K and above, including:

- a) Thermal imaging cameras
- b) Optical pyrometry
- c) Fibre optic thermometry
- d) Conventional thermocouples
- e) Thermal indicating paints

To employ either the thermal imager or optical pyrometry equipment would require an access window to be included in the furnace cavity. Accommodating an optical window in the compact furnace, large enough to see and thus measure the full length of the flexure testpiece, is problematic. Moreover the price of the thermal imager is in the order of £100k and radiation heating makes optical pyrometry impractical, so the problem did not arise. Fibre optic thermometry has the advantage of measuring temperatures down to a accuracy of 0.01K, though it is expensive in comparison to conventional thermocouples or resistance temperature detectors (RTD's). Since the tolerance level which was to be considered acceptable was in the region of $\pm 2\text{K}$ and the practicality of the number of sensors that would have to be purchased, conventional thermocouples were chosen.

Thermal indicating paints were used to assist the temperature measurement and calibration of the furnace designs

2.3.1 Displacement Measurement and Control

To measure the mid-point deflection of the flexure testpieces tensile surface, a LVDT was used. In-plane displacement was measured directly via an alumina rod attached to transducers placed outside the heat chamber. An additional LVDT situated on the sub-element above the support roller allows measurement of the materials 'lift'. Differential measurement between the two transducers gives the absolute displacement as shown in fig 2.3.1

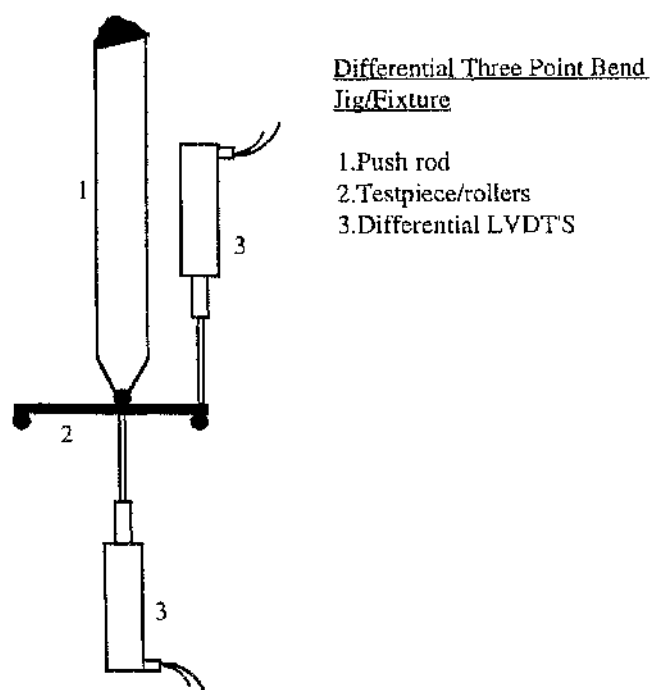


Fig 2.3.1 Differential LVDT set-up

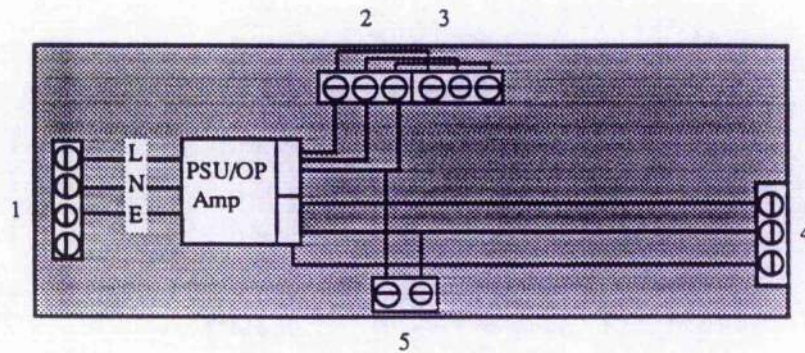
The initial choice of transducer was governed by the degree of repeatability, linearity and sensitivity that was considered necessary for accurate measurement (E.Herceg (1983))

and E.Doebelin (1983)). The unknown factor, which makes a final selection difficult was the likely displacement of each different sub-element. Based on Dupont Lanxide property data for a similar composite structure, two groups of AC powered transducers having a nominal linear range of $\pm 0.2''$ and $\pm 0.3''$ were used. To power the AC LVDT's a dual channel microprocessor based readout/controller was used.

Proof tests to check the repeatability and reliability of the instrumentation were carried out on a JJ Lloyds T30K test machine. The test machine had analog bipolar outputs: $\pm 10V$ for directly measuring the load and displacement. The LVDT controller operated in a similar bipolar manner of $\pm 2.5V$. Simple 3-point bend tests were conducted at ambient conditions on a range of 'known materials' including Steel, Pyrex, and Tufnol. The analog output from the machine and the LVDT controller were plotted against each other to ensure parity and provide confidence in the measurements. The T30K test machine had only manual load and displacement control and only provided output ports for measurement (not control). Although it could be upgraded for control purposes, it was decided to replace the machine with a controllable LR30K machine with interchangeable loadcells and autoranging digital readout of 10000 counts.

AC transducers generally operate on an excitation of $3V_{rms}$ (nominal), oscillated by the LVDT controller. The controller also delivers an analog $\pm 5V_{dc}$ full scale supply, which can be used as an input to the "external extensometer" pins in the universal test machine, to control the displacement of the crosshead. The extensometer pins take a unipolar voltage input of either 0-2Vdc or 0-10Vdc. Adjusting the ac gain, voltage and sensitivity levels in the microprocessor controller allows a suitable displacement range to be chosen to suit either of the unipolar input ranges of the test machine. A RS232 communication interface on the test machine allowed direct control of the displacement and/or the load via a software package used on a IBM PC system. However flexure proof tests, this time on brittle monolithic and ceramic composites with a maximum displacement of $\sim 0.1mm$, generated only a few millivolts from the transducer which is insufficient to drive the 12 bit

A/D converter (ADC) more than a few steps. Amplification of the output signal by a small adjustable op amp as shown in fig 2.3.2, didn't improve the resolution of the load-displacement response but contributed to diagnosis of the problem.



Power Supply Unit/Op Amp

- 1. 240v ac supply
- 2. $\pm 15V/0v$ PSU to transducer
- 3. Available x'ducer link
- 4. Amp input/output, 0V links
- 5. 0v/Earth links

Fig 2.3.2 Adjustable Op Amp and 15Vdc supply circuit

The test machine has a 12 bit ADC which is capable of measuring down to 2.4millivolts for a $\pm 10V$ range. This gives a stepped response over the range at displacements typical of the ceramic specimens. What was required was a LVDT having a larger signal to displacement output. A more suitable transducer for measuring the small displacements typical of the ceramic material was a dc powered LVDT. The LVDT selected had a range of 0.05 inch and sensitivity of 200V/inch. The dc transducer also required a input of $\pm 15Vdc$ which utilised the ac controllers $\pm 5Vdc$ output supply via amplification as shown previously in fig 2.3.2.

2.3.2 Temperature Measurement and Control

Due to the difficulty of bonding thermocouples to ceramics to read true surface temperatures, the surface temperature is best extrapolated from thermocouples embedded into holes drilled to a preset depth in the material (ASTM STP470B (1990), CREIPI (1987), Hillyer (1990)). Plugging of the hole is usually not necessary provided the sensor fits tightly into the drilled hole. Commercially available chromel-alumel TypeK mineral insulated (sheathed) thermocouples of 1.0mm diameter having a maximum temperature capability $\sim 1473\text{K}$ were used for all the tests. The method of embedding the thermocouples is satisfactory for steady state conditions but the delay in the response of thermocouples and the consequent misreading of the temperature makes it undesirable for transient testing. The thermocouple holes may be created by diamond tipped drills on the ceramic composites but the harder monolithic ceramics required the use of CO_2 and YAG lasers. Lasers available in the department allowed both drilling and shaping of testpieces up to 4mm thick. Initial problems with vaporized material re-solidifying in the hole before removal were overcome by modifying the beam parameters and clear holes of various sizes were achieved. Embedded thermocouples placed along the length of a metallic bend bar were used to monitor any temperature variations of the heated testpiece.

Initial temperature monitoring using purpose built software (Labview) showed that measured values oscillating in some tests once the set point temperature had been reached. It had been assumed that the set point thermocouple was being affected by direct radiation as a result of it not being embedded deeply enough. However drilling deeper holes and providing additional ceramic shielding around the sensor showed no improvement.

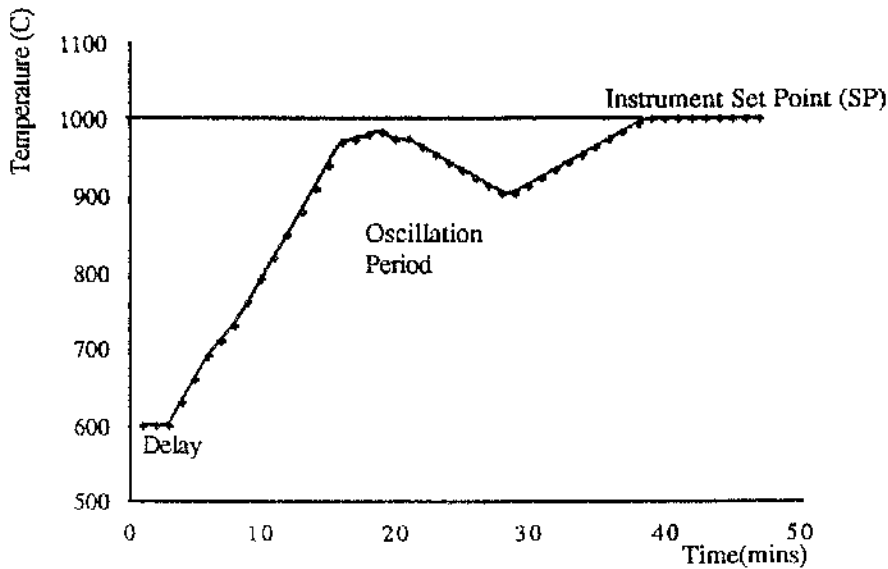


Fig 2.3.3 Self-Tune Control

The problem was traced to the PID temperature controller. Two of the inbuilt tuning algorithms- a so called 'self-tune' mode and 'adaptive-tune' mode allow the sensor control parameters to be automatically tuned. These are designed to prevent controlled variables from deviating outwith the set point position, and thus enable stable conditions to prevail (Buddery (1988)). 'Self-tuning' is a one shot algorithm, during which the controller inhibits all actions for a period in order to investigate the surrounding influences, before calculating the best proportional band (gain), integral time (reset), and the derivative time (rate) parameters to return to the instruments set point (1273K), as shown in fig 2.3.3. Adaptive-tune is a background algorithm which continuously monitors the error signal, though due to it's iterative nature, establishing satisfactory control may take a long time. In practice, self-tuning gave better stability for the times of the order of the test duration and was thus used for controlling the sp variable.

For steady state conditions the use of a dummy testpiece, of the same material under test, to house the temperature control sensor would eliminate the need to implant thermocouples into the actual testpiece. This was investigated. Embedded thermocouples in both a small dummy testpiece and in tested material, at mid-point position, were in general agreement after the soak period had elapsed. After calibration showed thermal gradients along the testpieces to be negligible, the temperature control sensor embedded in dummy testpiece was adopted throughout the test program as shown in fig 2.3.4.

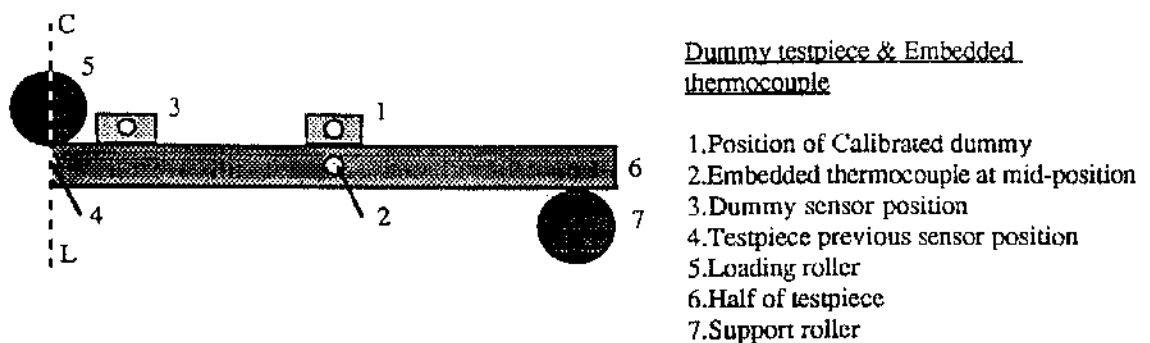
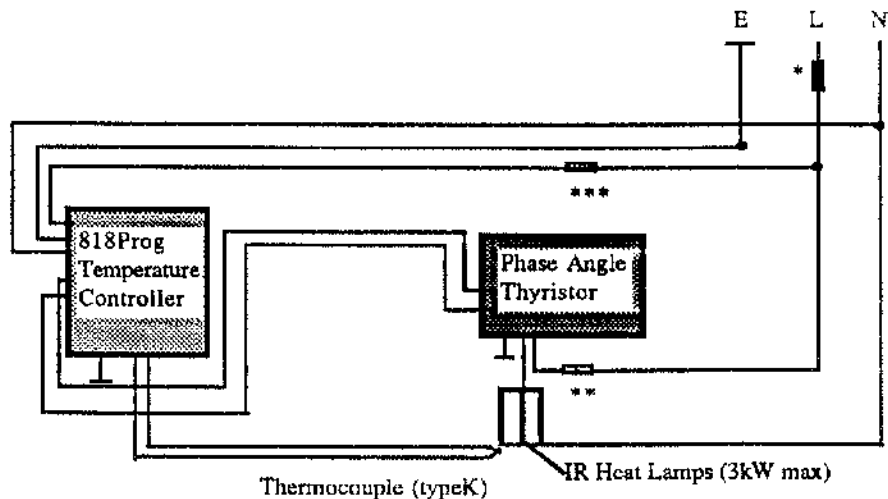


Fig 2.3.4 Embedded thermocouple in dummy testpiece

2.3.3 Furnace Heat Lamp Control

A Eurotherm programmable temperature controller and three single phase-phase angle thyristors were initially set-up to monitor and control the infra-red lamps. In the early stages of the project the amount of heat and thus the power required for achieving and maintaining temperatures of 1200K was unknown. Therefore the thyristor units were arranged to operate separately for a single phase load up to 25A or in conjunction for a 3 phase loading system (Langman (1987), Eurotherm (1990)). The single phased system is shown in fig 2.3.5.



- * Incoming fuse to protect cables
- ** 25A fuse
- *** Instrument fuse

Fig 2.3.5 Power control using a phased angle thyristor

To prevent thermal shock of the specimen and the lamp contacts it is necessary to ramp up the temperature slowly from room temperature. A rate of 127K/min up to the testing temperature of 1273K, maintained for 10 minutes 'soaking-time', was considered satisfactory.

2.3.4 Data Acquisition Systems

The choice of data acquisition software and hardware system was made after demonstrations from various vendors early in the project. The choice of system was governed by the sensors (Richard (1987)). Since ADC's on most boards operate on input voltages in the range of about $\pm 10V$, most sensors need some form conditioning for amplification, filtering and isolation (signal conditioning of the system is discussed under error sources). A versatile logging system was desirable, the capabilities of the system being;

- a) System could sample the channels in any order

- b) System sample with different gains on each channel-gains set in software
- c) System sample at high speed and still maintain the specified accuracy
- d) Is the board as accurate as it's ADC

National Instruments software package Labview satisfied these conditions and was chosen. Labview2 (LABoratory Virtual Instrument Engineering Workbench) is based on the concept of a virtual instrument (VI), a software file that looks like a laboratory instrument on-screen. Each VI comprises two parts; the front panel and the block diagram. The front panel is the user interface to the VI. It contains realistic looking (and acting) control items such as knobs, switches, slides and buttons as well as output items such as graphs and strip charts. These objects are intelligent - that is, a 'switch' knows how to behave, how to label itself; and most importantly, how to pass information to and from the underlying block diagram. The block diagram represents the program, with graphical objects representing programming elements. These are written in the G graphical language, based on the data flow model of programming, with enhancements and extensions to solve specific problems(Kodosky (1989), McCarty (1990))

The hardware chosen comprised of a multifunction I/O board for the Macintosh computer with a 12-bit ADC, up to 16 analog inputs, and two 12-bit DACs with voltage outputs. The multichannel extended resolution analog inputs are useful for signal and transient analysis and data logging, when directly coupled to the Labview2 application software package. Labview was first configured as a VI to enable data logging of load versus extension for simple tensile or bend tests on 'known materials' conducted at ambient conditions. On the completion of elementary trials, tests on composite model materials were introduced. The analog signals generated from the experimental tests are fed into a general-purpose breadboard, which incorporates temperature compensation and analog signal conditioning, before being passed to the M10-16 data acquisition board inside the Macintosh computer. The data acquisition system using Labview is shown in fig 2.3.7.

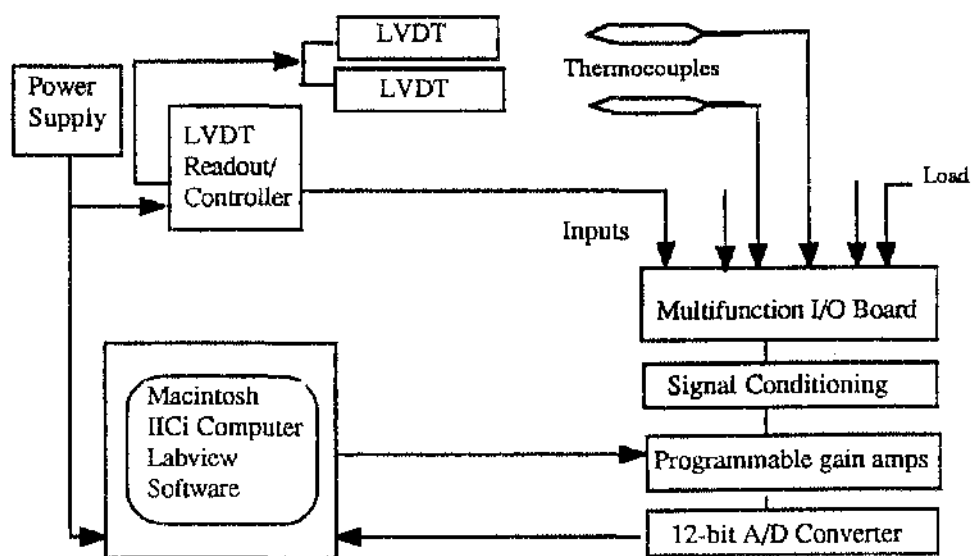


Fig 2.3.7 Data Acquisition using the software package Labview

Two types of data logging system can be produced with Labview, A single buffered and a double buffered system. The single buffered system displays to the screen only after the sampling is complete, whereas the double buffered system allows blocks of data to be retrieved and displayed without interrupting the acquisition. The former system, being the simpler of the two to be modelled, was initially built.

2.3.4.1 Single Buffering System

The data logging system was initially set-up to monitor four differential input channels, viz the load and cross-head displacement from the JJ Lloyd's test machine together with the mid-point and 'lift' transducers. This was later reduced to two channels, eliminating the cross-head displacement from the test machine due to uncertain readings that can be attributed to the compliance of the machine, and by directly subtracting the raw data from each other after the test is complete. Although the system worked satisfactory and allowed the user to get familiar with programming with icons, it didn't allow real-time display. A double buffered acquisition system was then designed.

2.3.4.2 Double Buffering system

A new 'user friendly' front panel was designed to control the enhanced data acquisition system. Expansion of the system, to monitor eight differential channels and to include possible analysis techniques, such as filtering, was undertaken. Enhancements to the existing software were carried out to include temperature monitoring. This enabled the temperature along the length of a testpiece to be monitored. The two virtual instruments, shown as Flexure and Temperature 'Icons', can be used separately in either single buffered or double buffered mode, or used jointly in the former to collect data.

An initial double buffered data logging system for displaying load versus displacement had the drawback that the process only displays the most recent block of data on the screen, the previous blocks being written to disc. This meant that updating the plot to show the complete history was impossible. Redesigning the block diagram to include a building block known as a shift register, which stores values from previous iterations, allows the n th and $n-1$, $n-2$, $n-3$ etc iterations to be concatenated. This allows the plot to be updated in realtime. The data logging systems are shown in Appendix A1.

2.3.4.3 Lloyd RControl Software System

In order to conduct flexure tests under displacement control, the dedicated software produced by Lloyd's had to be utilised, since 'Labview' could not exercise rights over the control of the axial movement. 'Labview' now functioned only as a data logger for temperature monitoring. The Lloyd software is equally acceptable, though maybe not quite as versatile as Labview, in fulfilling the task of logging the load-displacement data (having a similar 12 bit ADC). Tests conducted on the polyester composites and brittle monolithic ceramics sections using the displacement control software were satisfactory. The data logging system using Lloyds software is shown in fig 2.3.8.

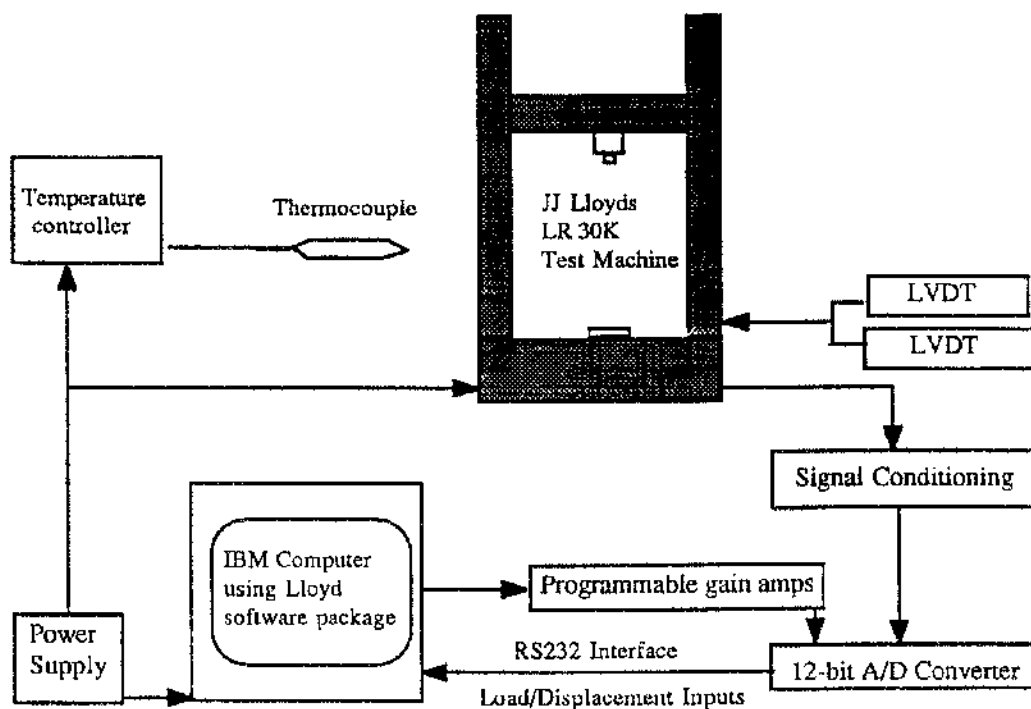


Fig 2.3.8 Data Acquisition system using Lloyd software

2.3.5 Data Logging Error Sources

Initially, noise pick-up was noticeable on the load-displacement readout. This was confirmed on the storage oscilloscope configured to trace small disturbance. The disturbance was identified as being due to *ground loops*. This problem is created if a signal circuit has more than one ground. If the multiple 'ground' points were at identical potentials, no problem would arise. However, the conductor on the A/D board that served as a ground generally carries unintentional currents and has some resistance; thus two points some distance apart will not have identical potentials.

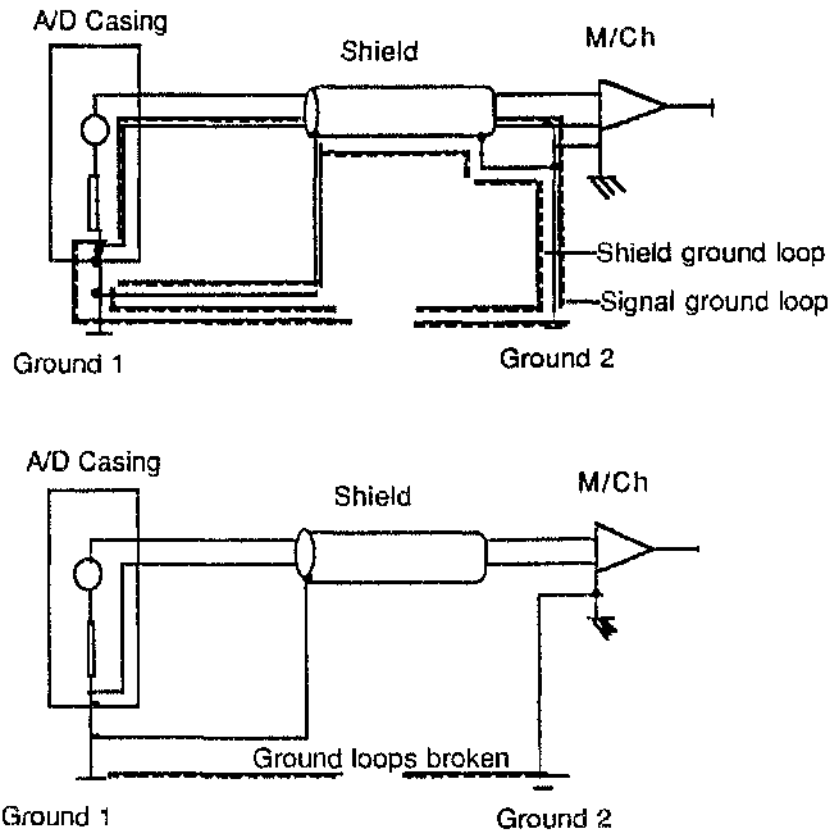
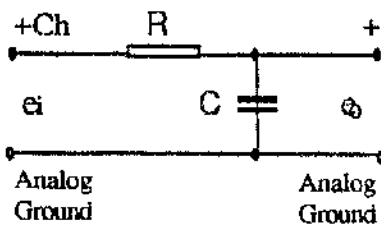


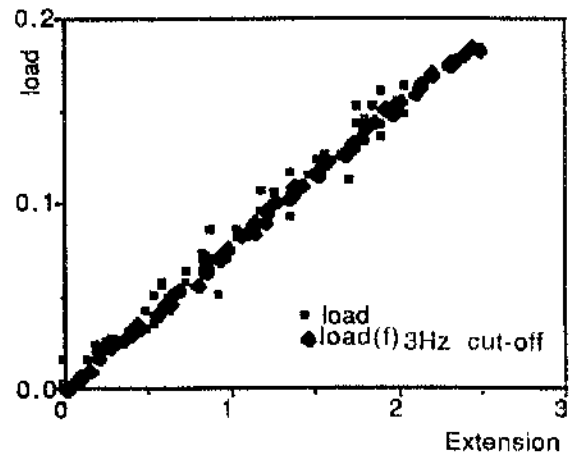
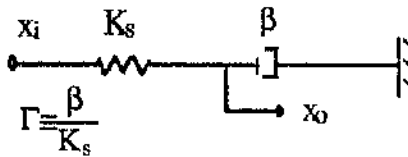
Fig 2.3.9 Ground loop problem and solution

Noise pick-up, shown on the oscilloscope as irregular saw tooth waveform was further reduced using twisted double screened cabling. The eight differential input channels were later housed in a fully screened and earthed rack shelf and the screwed terminal connections replaced with bnc screened connectors. Thus the 'signal-to-noise' ratio was improved considerably (Doebelin (1983)). Fig 2.3.9 illustrates in detail how the problem was rectified. The test machine output signals for load and crosshead displacement also contain noise generated by the gain amps. A simple RC low pass filter was inserted to give a cut-off frequency of 3Hz as shown in fig 2.3.10. This allowed sampling frequency of 1Hz to be attained without interference.

Electrical System



Equivalent Mechanical System



Transfer function governed by $\Gamma \equiv RC$

The cut-off frequency is governed by $f_c = \frac{1}{2\pi RC}$

Fig 2.3.10 Low pass filtering system

2.3.6 Equipment Calibration

To comply with RR Quality Control practice for all the experimental equipment used on the contract, an inventory record was kept. Details are given in GU experimental test laboratory's Test Programme Registrar (TPR). Included are details of test equipment accuracy, the experimental test programme for the sub-elements, the test procedures (including listing of national/international standards on which the test procedures were based) and calibration checks necessary for each test.

Chapter 3

Test Programme

3.0 Introduction

To facilitate the development and understanding of new ceramic composites, experimental testing was conducted in conjunction with computer modelling and design system development. Experimental investigations of composite materials and their properties provided the benchmarks for mathematical modelling of the components and materials. The mechanical behaviour of three composites: Dupont Lanxide 2-D laminated Nicalon-reinforced alumina ($\text{SiC}/\text{Al}_2\text{O}_3$), 2-D laminated polymer-reinforced polymer ("model materials") and Amercom 3-D braided Nicalon-reinforced silicon carbide (SiC/SiC) was investigated. The ceramics were investigated at room temperature and 1273K and the model material at room temperature only.

The generation of a materials database will allow predictive models to be developed and provide data for design purposes as outlined by Butler (1988). It is thus necessary to test components, either to failure (to verify the design analysis) or in a proof-testing mode (to assure an operational capability). It is also essential that the components are loaded in a similar manner to that they will experience in service, to mimic the operational stress conditions. The properties of the materials must be known, to enable prediction of performance under service conditions. The current situation in mechanical testing of advanced ceramic composites is characterised by a lack of standardisation. Problems associated with the uniaxial tensile testing of brittle materials resulted in the three-point flexure test being the preferred test method. Flexure tests were conducted on the JJ Lloyd LR30K test system incorporating interchangeable load cells under displacement control. The sequence of three-point flexure tests on the polymer composite and ceramic composite sub-elements, the bend bar, thickened (wedge) section and the t-section

addressed several key issues namely;

- a) The generation of a database for developing composite materials,
- b) Comparison of the non-dimensionalised load-displacement curves for the polymer and ceramic systems,
- c) Reduction of stiffness in the material, and thus the amount of damage that had been developed,
- d) Crack growth mechanisms and the Energy release rates.

3.1 Mechanical Flexure Tests

Although significant advances in the technology of non-destructive testing has been made in recent years its role in assessing new materials is still to be fully realised. Therefore the only certain way to ensure the quality and thus the consistency of a new material is to destructively test it as noted by Quinn (1991).

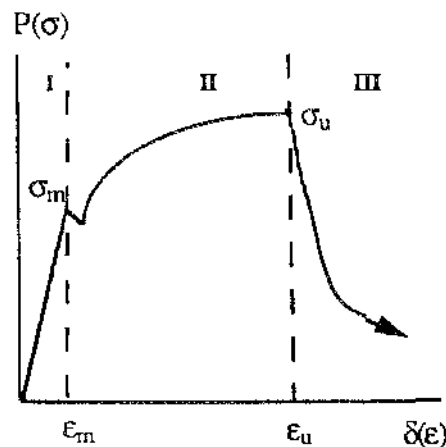


Fig 3.1 (a) Idealised load-displacement (stress-strain) graph under flexure loading

Figure 3.1 (a) shows the general features of the monotonic graph for a composite material. Experimental observations by Mecholsky (1986) of damage development and the monotonic load-displacement behaviour in unidirectional composites show three distinctive stages prior to failure. Stage I of the curve is linear elastic response before matrix cracking which occurs at a strain represented by ϵ_m , Stage II is a non-linear region with increasing load and displacement where multiple matrix micro-cracking occurs, with possible crack deflections at the fibre-matrix interface, up to a maximum strain of ϵ_u . Stage III of the curve is a region of decreasing load with increasing displacement where fibre pullout occurs. The monotonic flexure curves, for the tests undertaken, can therefore be used to determine the modulus of elasticity, stress at onset of matrix failure (OMF) σ_m , the stress and strain at ultimate flexure strength (σ_u, ϵ_u) and the strain to failure (ϵ_f).

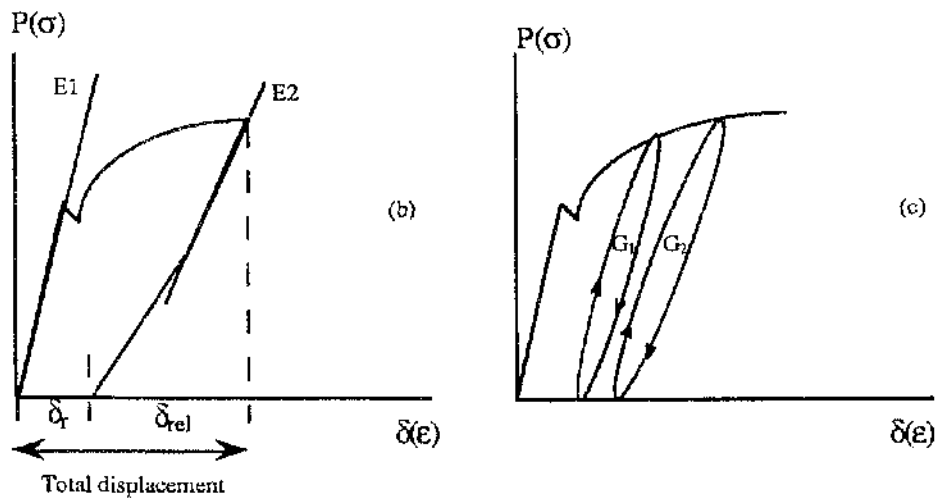


Fig 3.1 Cyclic load/unload curves, (b) allowing the determination of the load and unload modulus, reversible elastic and residual deformations, (c) to calculate the energy release rate (G)

To allow assessment of the the nature and the degree of micro-cracking through the thickness of the flexure testpieces, from the tensile to the compressive face of the structure, cyclic loading tests were conducted, in which the specimen was loaded to predetermined displacements, stopped and unloaded as shown in fig 3.1(b). To facilitate

the choice of unload/load cycles, cyclic tests were carried out after a monotonic test to failure had been undertaken for each of the three materials. This also established the elastic/inelastic boundary.

The strain energy release rate (G), associated with delamination growth, can be determined by integrating the area under each cyclic hysteresis loop (fig 3.1(c)), and used in fracture mechanics calculations. Cyclic load/unload tests allow the decay in the loading elastic modulus ($E1$) and the unloading modulus ($E2$) to be determined and used as a measure of damage. The reversible elastic deformation (δ_{rel}) and the residual deformation (δ_r) can be determined from each cyclic load/unload test shown in fig 3.1 (b). Work done by Inghels & Lamon (1991) on SiC/SiC and C/SiC composites allowed the complex nature of the composite materials elastic/inelastic response to be described using a reduced number of parameters. Their theoretical approach will be used.

3.1.1 Bend Bars

The function of the bend bar sub-elements was to determine basic mechanical properties of the polymer and ceramic systems and allow the assessment of damage from point-loading to be investigated. The elastic stress and strains were derived from a nominal cross-sectional area of bend bar having a breadth of 10mm and a depth of 3mm. The properties in the linear elastic region may be estimated from constituent properties by the rule of mixtures

$$E_c = E_f V_f B + E_m V_m \quad (3.1.1)$$

pioneered by Krenchel (1964). Here E_c is the composite modulus and $B=1, \frac{1}{2}$ for unidirectional, bidirectional (in-plane) respectively. Since the fibres in the composite lie at 90 degrees to one another they are classed as bidirectional and so $B=\frac{1}{2}$.

3.1.2 Model Material Bend Bars (MMBB)

Load-displacement curves obtained from the flexure tests conducted on the polymer/polymer composite testpieces are shown in figure 3.1.2. Model material bend bars 'MMBB1 and MMBB2' were loaded monotonically to determine a failure graph for the material. However since the model material bend bars possess a large degree of ductility, failure wasn't produced in the length of specimen tested. Bend bars MMBB3-6 were subjected to a sequence of cyclic tests up to various predetermined displacements, stopped and unloaded. With the model material, the deformation of the bar testpieces exceeded that allowed by simple beam theory and the deflection to failure was large. However, since the emphasis of the tests on these ductile materials was on displaying micro-cracking, which was clearly evident on the load-displacement graphs, the tests were useful. Data from the monotonic and cyclic load/unload flexure tests of the model material bend bars are tabulated in table 3.1 which shows an average elastic modulus of 3.97GPa. The material exhibited a linear load-displacement response up to the initiation of microcracking, which started at an average stress (σ_m) of 31MPa(46N) and strain (ϵ_m) of 7.3E-3.

Continued microcracking from $\epsilon_m=7.3E-3$ up to $\epsilon_m=15E-3$ produced a non-linear region. Upon further deformation the first major drop in load is observed at an average stress of 62MPa. The load drop is a result of the load carrying capacity of the composite being transferred to the fibres. This is the maximum flexure strength (σ_u) for the material. As the material is further strained, multiple matrix cracking progresses across the width of the specimen. Initially the number and length of microcracks increases with loading, and theoretically should eventually cover the entire cross-section of the specimen. This however wasn't observed in practice, saturation over the entire cross-section ('full saturation') being pre-empted by partial macro-cracking. This may be attributed in the bend bars to non-uniform stress fields. A stress level is however reached at which

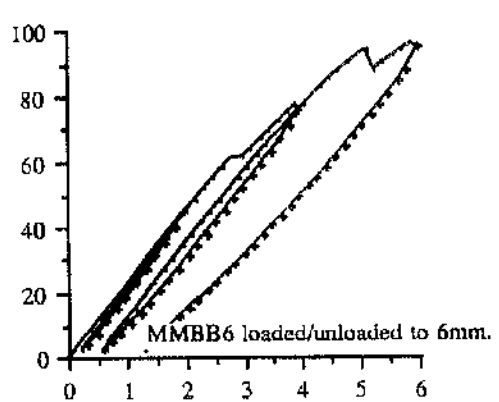
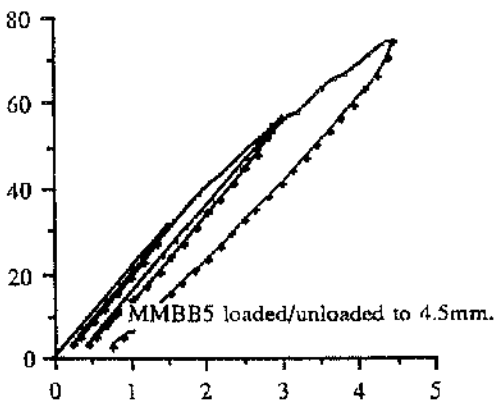
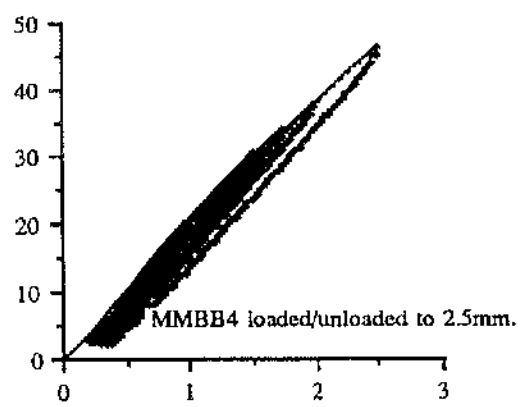
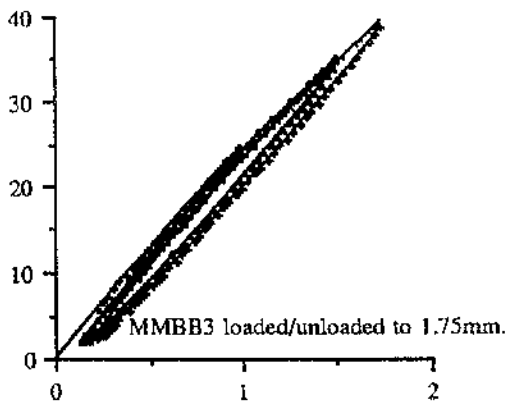
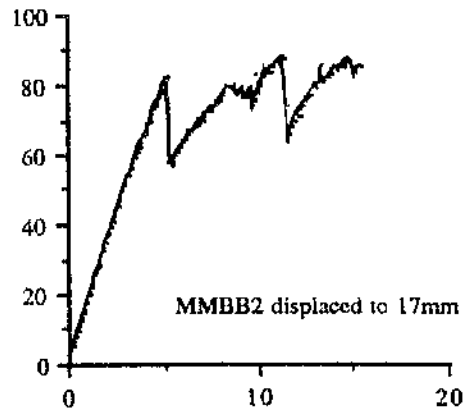
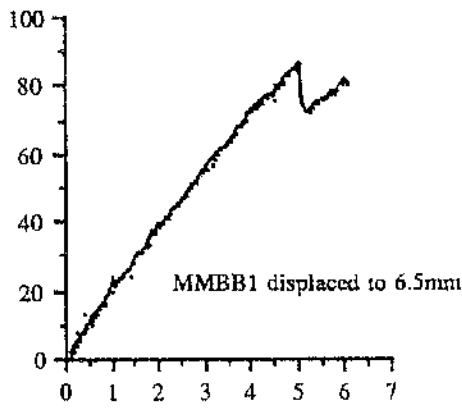


Fig 3.1.2 Load-displacement curves for Model Material Bend Bar (MMBB)

microcracking of the specimen saturates over part of the x-section ('partial saturation') and no further microcracking occurs. Failure stresses and strains for the model material bend bars couldn't be measured.

3.1.3 Dupont Lanxide Bend Bars (RSB)

Load-displacement curves obtained from the flexure tests conducted on the 2-D SiC/Al₂O₃ RSB sub-elements are shown in figure 3.1.3. Initially RSB001 was to be the reference failure plot. However the material was less stiff than expected from the Dupont Lanxide manufacturers data sheets. After some practical experience with the material, RSB007 was able to be taken to failure. RSB002-RSB008, including RSB007, were subjected to cyclic tests ie loaded up to predetermined displacements, stopped and unloaded. RSB008 was displaced to just above the onset of matrix micro-cracking before being unloaded. The tested SiC/Al₂O₃ composite bend bars had an average density calculated to be 2.74g/cm³ and an assumed fibre volume fraction (V_f) of 35% and Poisson's ratio of 0.29. Data from the monotonic and cyclic load/unload flexure tests of the Dupont Lanxide bend bars are tabulated in table 3.2 which shows an average elastic modulus of 132GPa. The material exhibited a linear elastic response up to the initiation of microcracking, which started, at an average stress (σ_m) of 156MPa(134N) and a strain (ϵ_m) of 1.07E-3. From the onset of microcracking up to the average maximum flexure strength (σ_u) of 380MPa the behaviour was non-linear. As with the model material bend bar, further strain caused the progression of multiple matrix cracking across the width of the specimen, the number and length of cracks increasing with loading. Full saturation again was pre-empted by partial macro-cracking. Flexure failure of the ceramic bend bar occurred at a strain (ϵ_f) of 0.032.

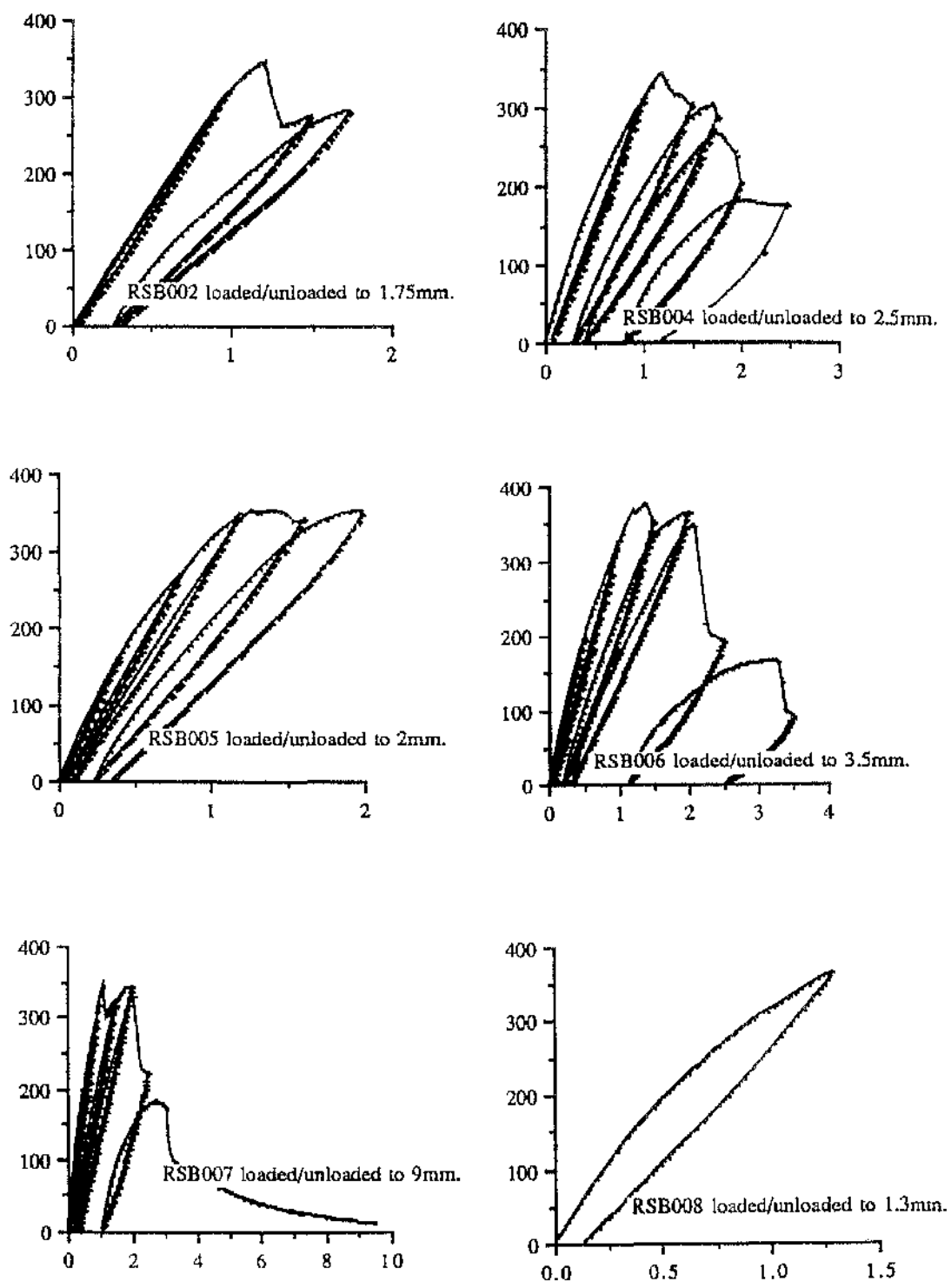


Fig 3.1.3 Load-displacement curves for Dupont Lanxide Bend Bars (RSB)

3.1.4 Amercom Composite Bend Bars

Load-displacement curves obtained from the flexure tests conducted on the Amercom SiC/SiC sub-elements are shown in figures 3.1.4. Amercom002 was taken to failure and used as the reference failure plot. Amercom001 was subjected to a 3 x load/reload cycles. Data from the monotonic and cyclic load/unload flexure tests of the Amercom bend bars are tabulated in table 3.2 which shows an average elastic modulus of 120GPa. The material exhibited a linear elastic load-displacement response up to the initiation of microcracking, which started at an average stress (σ_m) of 68MPa(57N) and a strain (ϵ_m) of $5.7E-4$. From the onset of microcracking up to the average maximum flexure strength (σ_u) of 138MPa the behaviour was non-linear. Flexure failure of the Amercom bend bar occurred at a strain of (ϵ_f) 0.033.

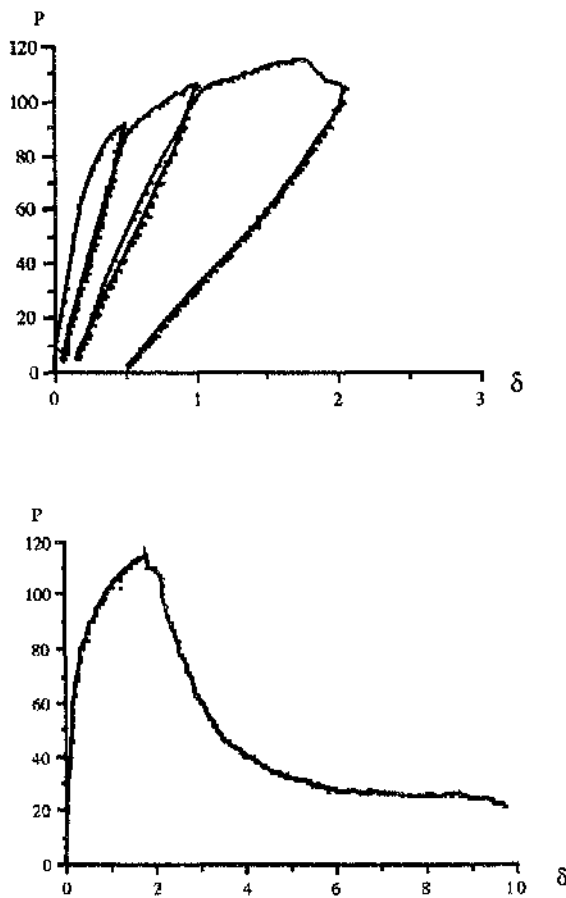


Fig 3.1.4 Amercom load-displacement curves.

3.1.5 Wedge Sections

The function of the thickened(wedge) sub-elements was to allow assessment of damage such as mode-2 (shear) delamination initiating from laminated changes in section.

3.1.6 Model Material Wedge Sections (MMWS)

Load-displacement curves obtained from the flexure tests conducted on the MMWS testpieces are shown in figure 3.1.6. 'MMWS1' and 'MMWS2' show monotonic flexure plots of load against displacement. As with the polymer model material bend bars, these wedge sections exhibited a large degree of ductility and the large deformation needed for failure wasn't reached for the length of specimen being tested. The elastic stress and strains were derived from a nominal cross-sectional area of a wedge section having a breadth of 10.75mm and a depth of 8.15mm.

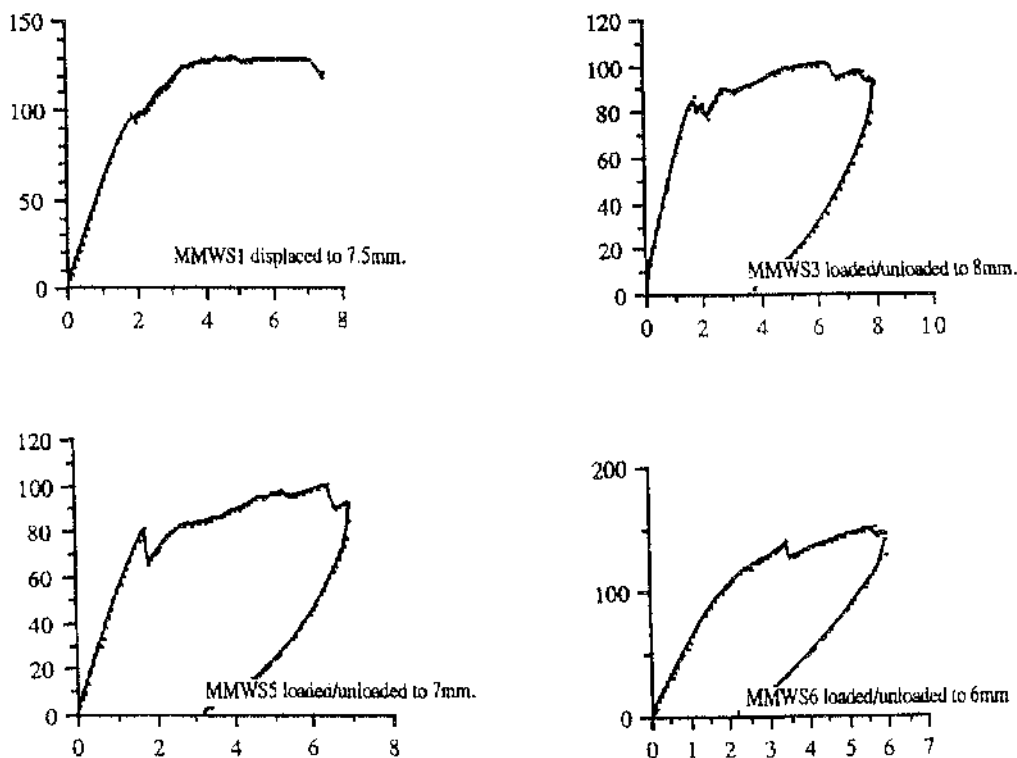


Fig 3.1.6 Load-displacement curves for Model Material Wedge Sections (MMWS)

Bend bars MMWS3-6 were subjected to a sequence of cyclic tests loaded up to various predetermined displacements, stopped and unloaded. Data from the monotonic and cyclic load/unload flexure tests of the model material thickened sections are tabulated in table 3.3 which shows an average stiffness of 53kN/m for a nominal elastic modulus of 4GPa. The material exhibited a linear elastic load-displacement response up to the initiation of microcracking, which started at an average stress (σ_m) of 56MPa(67N) and a strain (ϵ_m) of 0.014. From the onset of microcracking up to the average maximum flexure strength (σ_u) of 88MPa the behaviour was non-linear. Failure stress and strain levels for the model material thickened sections couldn't be measured.

3.1.7 Dupont Lanxide Reinforced Sections (RSR)

Load-displacement curves obtained from the flexure tests conducted on the RSR sub-elements are shown in figures 3.1.7. RSR001 was used as the reference failure plot. RSR002-RSB004 were subjected to a sequence of cyclic tests loaded up to various predetermined displacements, stopped and unloaded. The elastic stress and strains were derived from a nominal cross-sectional area of wedge section having a breadth of 10.16mm and a depth of 7.5mm.

Data from the monotonic and cyclic load/unload flexure tests of the Dupont Lanxide reinforced sections are tabulated in table 3.4 and show an average stiffness of 2MN/m, for a nominal elastic modulus of 140GPa. The material exhibited a linear elastic load-displacement response up to the initiation of microcracking, which started at an average stress (σ_m) of 310MPa(305N) and a strain (ϵ_m) of 2.2E-3. From the onset of microcracking up to the average maximum flexure strength (σ_u) of 441MPa the behaviour was non-linear. Flexure failure for the ceramic thickened section occurred at a strain of (ϵ_f) 0.03

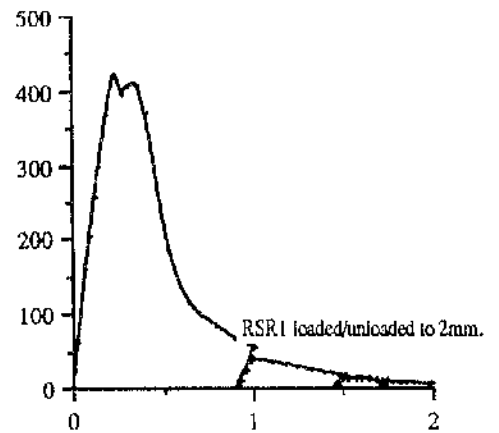
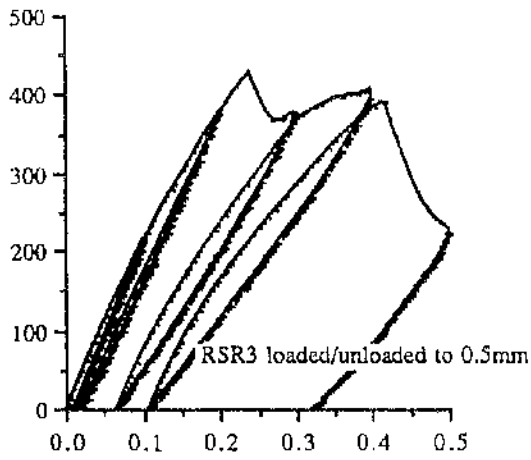
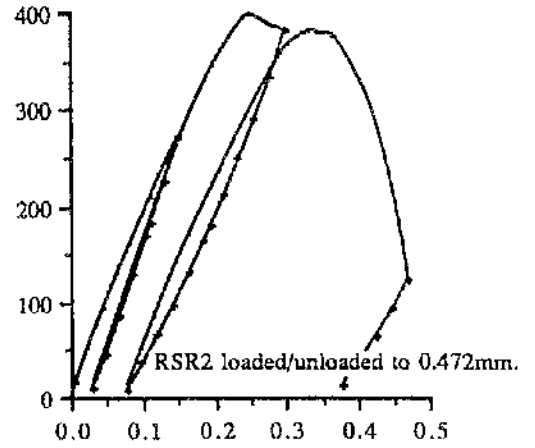
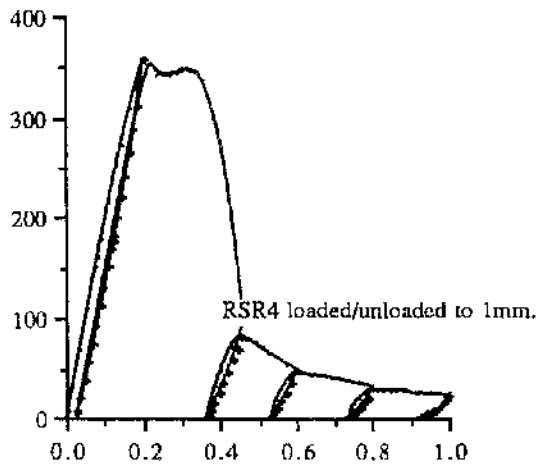


Fig 3.1.7 Load-displacement curves for Dupont Lanxide Reinforced Sections (RSR)

3.1.8 T-Sections

The function of the T-Section sub-elements was to admit assessment of damage such as mode-1 (tensile) delamination initiating from through thickness tension in the web.

3.1.9 Model Material T-Sections (MMTS)

Load-displacement curves obtained from the flexure tests conducted on MMTS testpieces are shown in figure 3.1.9. MMTS1 and MMTS2 show monotonic flexure plots of load against displacement. The elastic stress and strains were derived from a nominal cross-sectional area of t-section having a breadth of 10mm and a depth of 2.85 and a web of length 22.15mm. As with the polymer model material bend bars, the t-sections exhibited a large degree of ductility and the large deformation needed for complete failure wasn't achieved for the length of specimen tested. T-Sections MMTS3-8 were subjected to a sequence of cyclic tests, loaded up to various predetermined displacements, stopped and unloaded. MMTS4 and MMTS6 were manufactured from a different batch which had approximately half the stiffness of the other t-sections tested.

Measured values for the monotonic and cyclic load/unload flexure tests of the model material t-sections are tabulated in table 3.5 gave an average stiffness of 12.4kN/m for a nominal elastic modulus of 4GPa (MMTS4,MMTS6 excluded). The material exhibited a linear elastic load-displacement response up to the initiation of micro-cracking, which started at an average stress (σ_m) of 13MPa and a strain (ϵ_m) of 0.036. From the onset of microcracking up to the average maximum flexure strength (σ_u) of 26MPa the behaviour was non-linear. Failure stress and strain levels for the model material t-sections couldn't be measured.

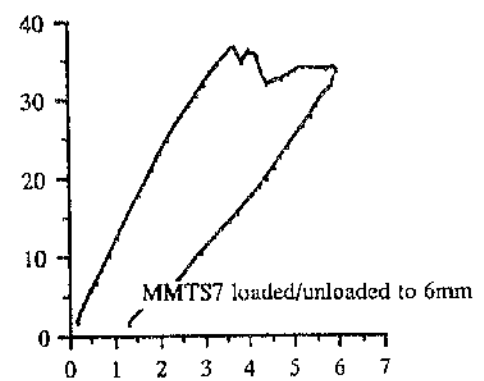
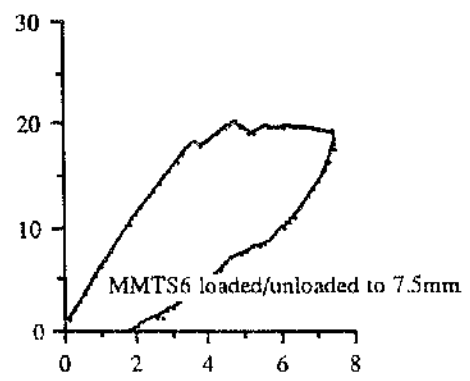
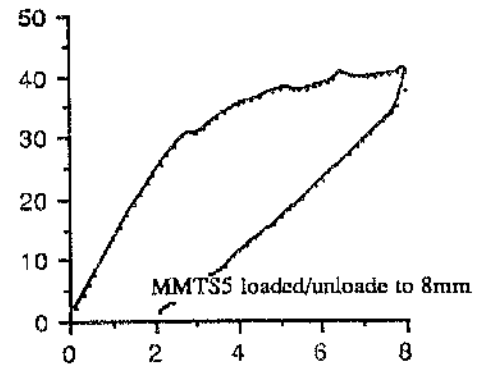
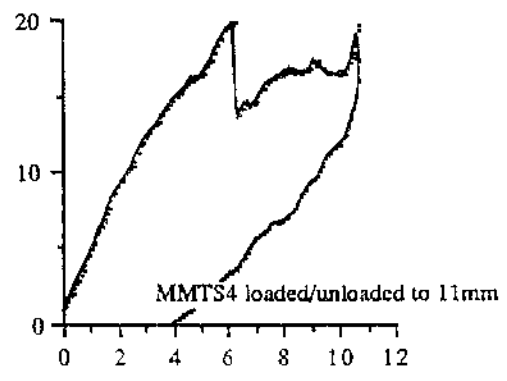
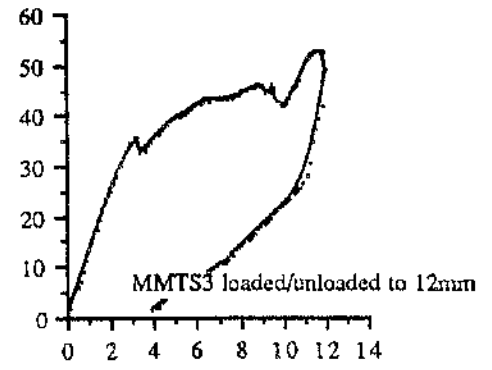
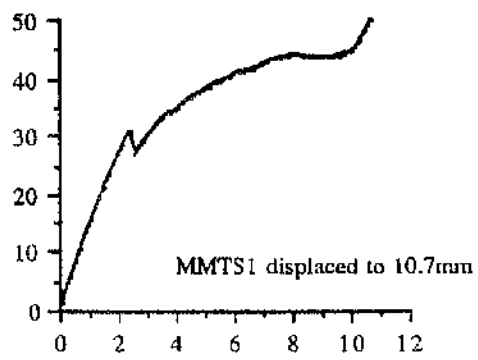


Fig 3.1.9 Load-displacement curves for Model Material T-Sections (MMTS)

3.1.10 Dupont Lanxide T-Sections (RST)

Load-displacement curves obtained from the flexure tests conducted on the RST sub-elements are shown in figures 3.1.10. RST001 was used as the reference failure plot. RST002-RSB003 were subjected to a sequence of cyclic tests loaded up to various predetermined displacements, stopped and unloaded. The elastic stress and strains were derived from a nominal cross-sectional area of t-section having a breadth of 10.16mm and a depth of 3.6 and a web of 11.8mm.

Data from the monotonic and cyclic load/unload flexure tests of the Dupont Lanxide T-Sections are tabulated in table 3.6 which shows an average stiffness of 828kN/m, for a nominal elastic modulus of 140GPa. The material exhibited a linear elastic load-displacement response up to the initiation of micro-cracking, which started at an average stress (σ_m) of 30MPa(121N) and a strain (ϵ_m) of 2.1E-4. From the onset of microcracking up to the average maximum flexure strength (σ_w) of 49MPa the behaviour was non-linear. Flexure failure for the ceramic T-section occurred at a strain of (ϵ_f) 8.6E-3.

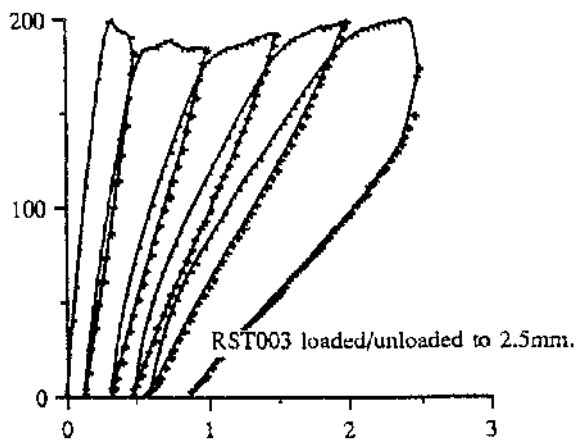
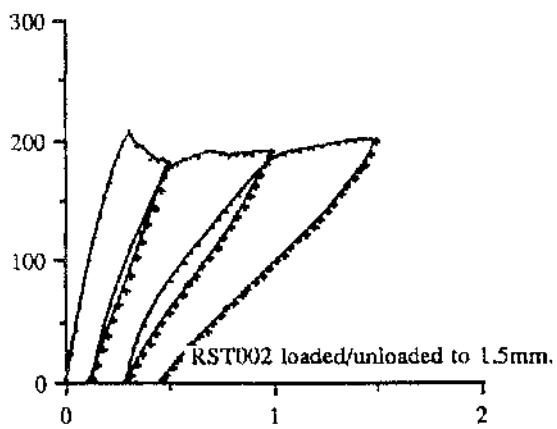
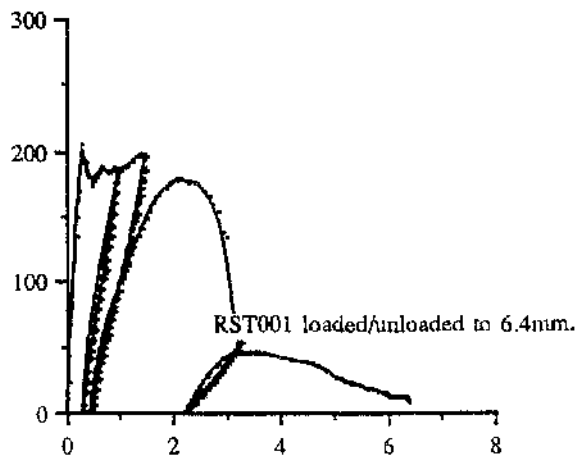


Fig 3.1.10 Load-displacement curves for Dupont Lanxide T-Sections (RST)

<u>Test No</u>	<u>E1 (GPa)</u>	<u>K1 (N/mm)</u>	<u>E2 (GPa)</u>	<u>K2 (N/mm)</u>	<u>OMF (MPa)</u>	<u>No Cycles</u>
MMBB1	3.53	18.59	-	-	29	1
MMBB2	3.33	16.98	-	-	30	1
MMBB3	4.43	25.0	4.43	25.00	28	1
	4.34	24.52	4.30	24.31		2
	4.28	24.20	4.27	24.13		3
MMBB4	4.21	21.58	4.17	20.96	31	1
	4.21	21.58	4.15	21.26		2
	4.13	21.20	4.10	21.03		3
	4.05	20.76	4.03	20.65		4
	3.95	20.26	3.94	20.19		5
MMBB5	4.13	21.95	4.13	21.95	33	1
	3.64	19.36	3.89	20.70		2
	3.75	19.94	3.52	18.70		3
MMBB6	4.27	24.57	4.27	24.57	32	1
	4.07	23.37	3.80	21.83		2
	3.81	21.87	3.29	18.92		3
MMBB7	4.03	22.39	3.90	21.67	33	1
	3.74	20.76	3.36	18.65		2
	3.48	19.32	2.73	15.19		3

Table 3.1 Model Material Bend Bar (MMBB)

Test No	E1 (GPa)	K1 (N/mm)	E2 (GPa)	K2 (N/mm)	OMF (MPa)	No Cycles
RSB001	110	346	xx		164	1
	101	318				2
RSB002	102	321	101	318	173	1
	100	314	84	265		2
	97	305	81	256		3
RSB003	145	456	109	344	165	1
	115	362	92	288		2
	113	355	87	275		3
	98	308	71	224		4
	79	248	-			
RSB004	132	416	111	350	156	1
	101	318	95	301		2
	95	298	89	282		3
	91	286	74	233		4
	72	226		233		5
RSB005	140	440	137	431	143	1
	127	400	114	358		2
	110	346	99	311		3
	95	299	92	289		4
	88	277	81	256		5
RSB006	142	460	134	420	136	1
	132	419	109	344		2
	107	342	98	307		3
	95	318	85	266		4
	89	311	59	187		5
	70	243	27	92		6
RSB007	140	450	135	424	151	1
	133	421	108	341		2
	111	358	77	243		3
	108	368	63	198		4
	100	355	60	188		5
RSB008	141	430	109	342	157	1
RSB009	Not Tested					
Am001	114	355	60	188		1
	65	202	36	113		2
	53	166	20	62		3
Am002	127	397				1

Table 3.2 Dupont Lanxide Bend Bars (RSB)/Amercom(Am)

<u>Test No</u>	<u>E1 (GPa)</u>	<u>K1 (N/mm)</u>	<u>E2 (GPa)</u>	<u>K2 (N/mm)</u>	<u>OMF (MPa)</u>	<u>No Cycles</u>
MMWS1	x	56.5	-	-	78	1
MMWS2	x	54	-	-	64	1
MMWS3	x	53.9	x	20.8	62	1
MMWS4	x	45	x	26.2	60	1
MMWS5	x	51	x	23.3	56	1
MMWS6	x	58.9	x	36.39	81	1

Table3.3 Model Material Wedge Section (MMWS)

<u>Test No</u>	<u>E1 (GPa)</u>	<u>K1 (N/mm)</u>	<u>E2 (GPa)</u>	<u>K2 (N/mm)</u>	<u>OMF (MPa)</u>	<u>No Cycles</u>
RSR001	x	1925	x	520	312	1
	x	640	x	306		2
	x	312	x	212		3
	x	200	x	133		4
RSR002	x	2103	x	2195	318	1
	x	2094	x	1659		2
	x	1811	x	1156		3
RSR003	x	2127	x	2312	290	1
	x	2319	x	2075		2
	x	2118	x	1557		3
	x	1967	x	1319		4
	x	1972	x	1180		5
RSR004	x	1915	x	1931	305	1
	x	1938	x	925		2
	x	1450	x	675		3
	x	1025	x	428		4
	x	905	x	260		5

Table3.4 Dupont Lanxide Wedge Section (RSR)

<u>Test No</u>	<u>E1 (GPa)</u>	<u>K1 (N/mm)</u>	<u>E2 (GPa)</u>	<u>K2 (N/mm)</u>	<u>OMF (MPa)</u>	<u>No Cycles</u>
MMTS1	x	13.4	-	-	23	1
MMTS2	x	12.4	-	-	24	1
MMTS3	x	12.47	x	5.84	25	1
MMTS4*	x	4.11	x	2.5	13	1
MMTS5	x	12.08	x	6.6	22	1
MMTS6*	x	5.23	x	3.32	13	1
MMTS7	x	11.5	x	6.79	25	1
MMTS8	x	12.54	x	10.27	23	1

Table3.5 Model Material T-Section (MMTS)

* Different Batch of material

<u>Test No</u>	<u>E1 (GPa)</u>	<u>K1 (N/mm)</u>	<u>E2 (GPa)</u>	<u>K2 (N/mm)</u>	<u>OMF (MPa)</u>	<u>No Cycles</u>
RST001	x	839	x	253	116	1
	x	525	x	175		2
	x	433	x	49		3
	x	95	x	-		4
RST002	x	868	x	462	119	1
	x	664	x	258		2
	x	643	x	179		3
RST003	x	776	x	477	128	1
	x	703	x	262		2
	x	519	x	179		3
	x	433	x	136		4
	x	344	x	90		5

Table3.6 Dupont Lanxide T-Sections (RST)

3.2 Thermomechanical Flexure Tests

Flexural testing is necessary at elevated temperatures to provide a ceramic material properties database relevant to design and application in the proposed high-temperature application. This also assists basic understanding of deformation and failure mechanisms. The same deficiencies in standardisation of testing methods apply at high temperature as at ambient conditions. The apparatus used at room temperature for flexure testing was also designed to be used (with the addition of a furnace of course) for high temperature testing, to allow direct comparison of the results.

3.2.1 Dupont Lanxide Bend Bars (RSB)

Load-displacement curves obtained from the flexure tests conducted on the RSB sub-elements at 1273K are shown in figure 3.2.1 RSB010 and RSB011 were taken to failure. RSR013-RSB018 were subjected to a sequence of cyclic tests at 1273K, loaded up to various predetermined displacements, stopped and unloaded.

Data from the monotonic and cyclic load/unload flexure tests of the Dupont Lanxide bend bars at 1273K are tabulated in table 3.7 and show an average elastic modulus of 127GPa. The material exhibited a linear elastic load-displacement response up to the initiation of microcracking, which started at an average stress (σ_m) of 149MPa(128N) and a strain (ϵ_m) of 1.06E-3. From the onset of microcracking up to the average maximum flexure strength (σ_u) of 420MPa the behaviour was non-linear. As with the model material bend bar, when Dupont Lanxide was further strained, multiple matrix micro-cracking continued across the width of the specimen, the number and length of cracks increasing with loading. High temperature flexure failure for the ceramic bend bar occurred at a strain of (ϵ_f) 0.033.

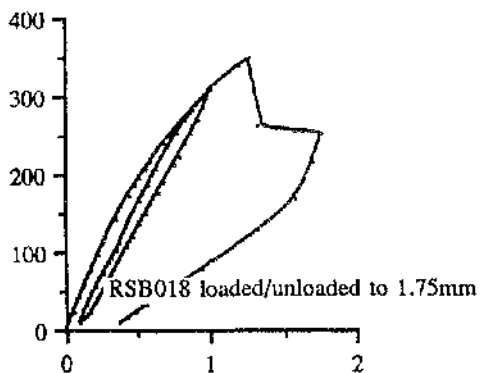
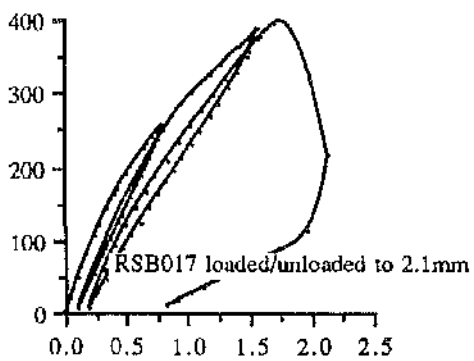
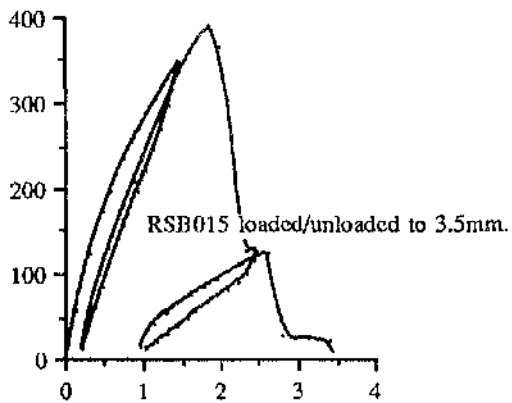
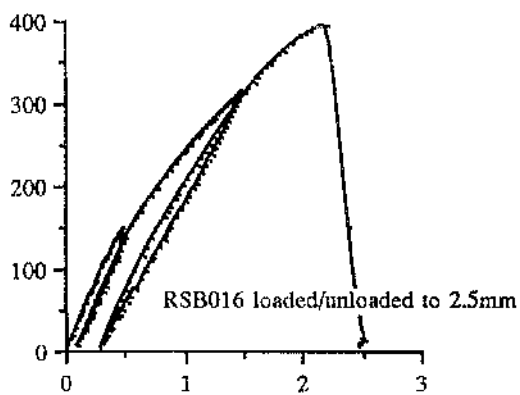
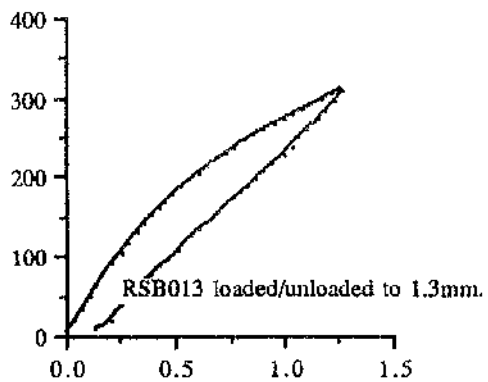
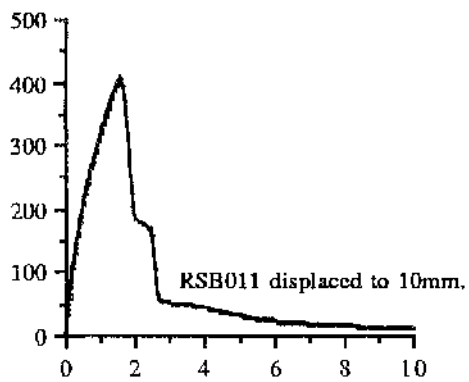


Fig 3.2.1 Load-displacement curves for Dupont Lanxide Bend Bars (RSB) at 1273K

3.2.2 Amercom Composite Bend Bars

The monotonic load-displacement curve for Amercom 003 tested at 1273K up until failure is shown in figure 3.2.2. Data from the monotonic flexure tests of the Amercom bend bar is tabulated in table 3.7 which shows an average elastic modulus of 85GPa at 1273K. The material exhibited a linear elastic load-displacement response up to the initiation of microcracking, which started at an average stress (σ_m) of 52MPa(45N) and a strain (ϵ_m) of 8.12E-3. From the onset of microcracking up to the average maximum flexure strength (σ_u) of 76MPa the behaviour was non-linear. High temperature flexure failure of the Amercom bend bar occurred at a strain of (ϵ_f) 0.04.

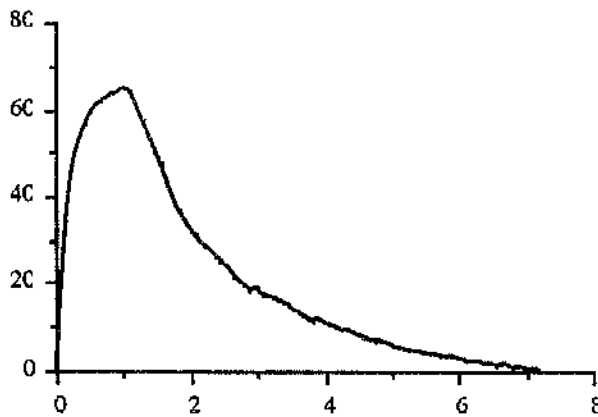


Fig 3.2.2 Amercom bendbar displaced to failure at 1273K

3.2.3 Dupont Lanxide Reinforced Sections (RSR)

Load-displacement curves obtained from the flexure tests conducted on the RSR sub-elements at 1273K are shown in figure 3.2.3. RSR005 was taken to failure. RSR006-RSB008 were subjected to a sequence of cyclic tests at 1273K loaded up to various predetermined displacements, stopped and unloaded.

Data from the monotonic and cyclic load/unload flexure tests of the Dupont Lanxide thickened sections are tabulated in table 3.8 which shows an average stiffness of

1361kN/m, equivalent to an average elastic modulus of 94GPa at 1273K. The material exhibited a linear elastic load-displacement response up to the initiation of microcracking, which started at an average stress (σ_m) of 238MPa and a strain (ϵ_m) of $2.5E-3$. From the onset of microcracking up to the average maximum flexure strength(σ_u) of 352MPa, the behaviour was non-linear. High temperature flexure failure for the ceramic thickened section occurred at a strain of (ϵ_f) 0.03.

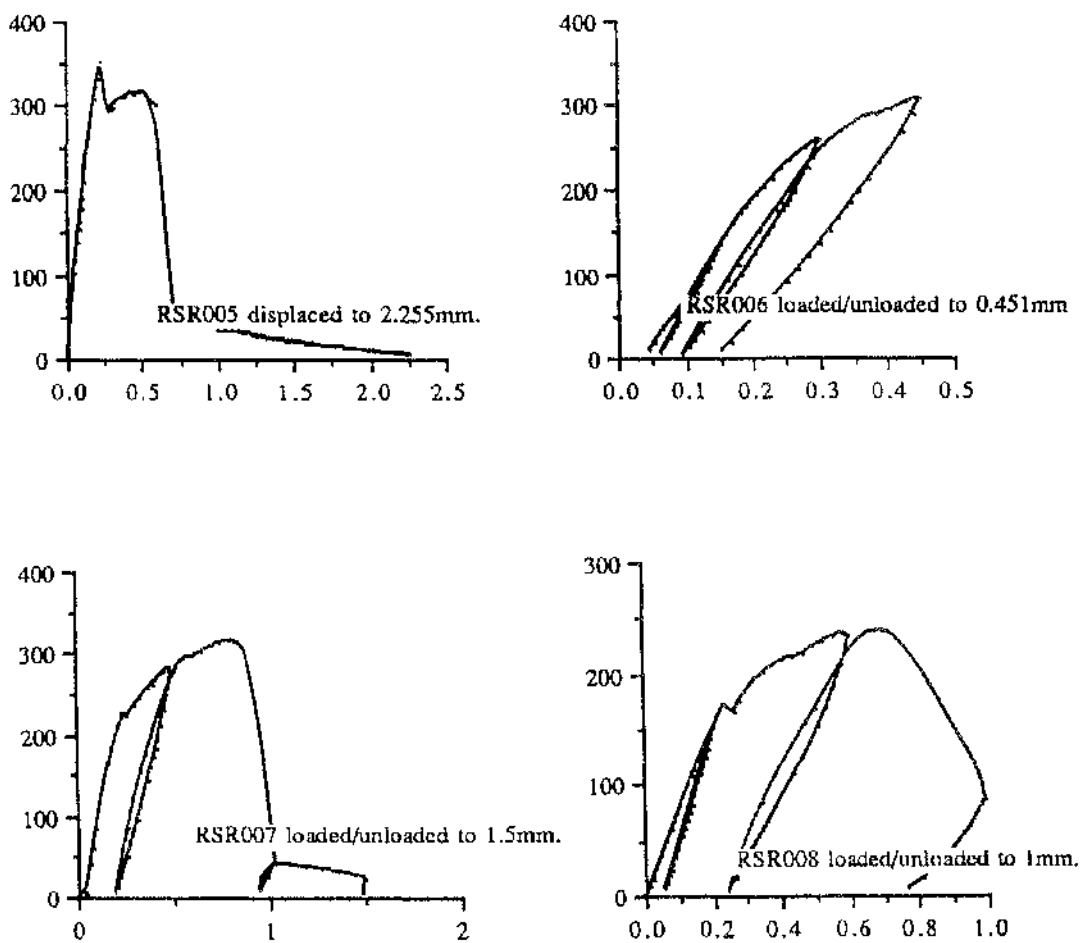


Fig 3.2.3 Load-displacement curves for Dupont Lanxide Wedge Sections (RSR) at 1273K

3.2.4 Dupont Lanxide T- Sections (RST)

Load-displacement curves obtained from the flexure tests conducted on the RST sub-elements at 1273K are shown in figure 3.2.4. RST004 and RST005 were taken to failure. RST006-RST008 were subjected to a sequence of cyclic tests at 1273K, loaded up to various predetermined displacements, stopped and unloaded.

Data from the monotonic and cyclic load/unload flexure tests of the ceramic T-Sections are tabulated in table 3.9 which shows an average stiffness of 705kN/m, equivalent to an average elastic modulus of 119GPa. The material exhibited a linear elastic load-displacement response up to the initiation of microcracking, which started at an average stress (σ_m) of 29MPa and a strain (ϵ_m) of 2.4E-4. From the onset of microcracking up to the average maximum flexure strength (σ_u) of 44MPa the behaviour was non-linear. High temperature flexure failure occurred at a strain of (ϵ_f) 8.4E-3.

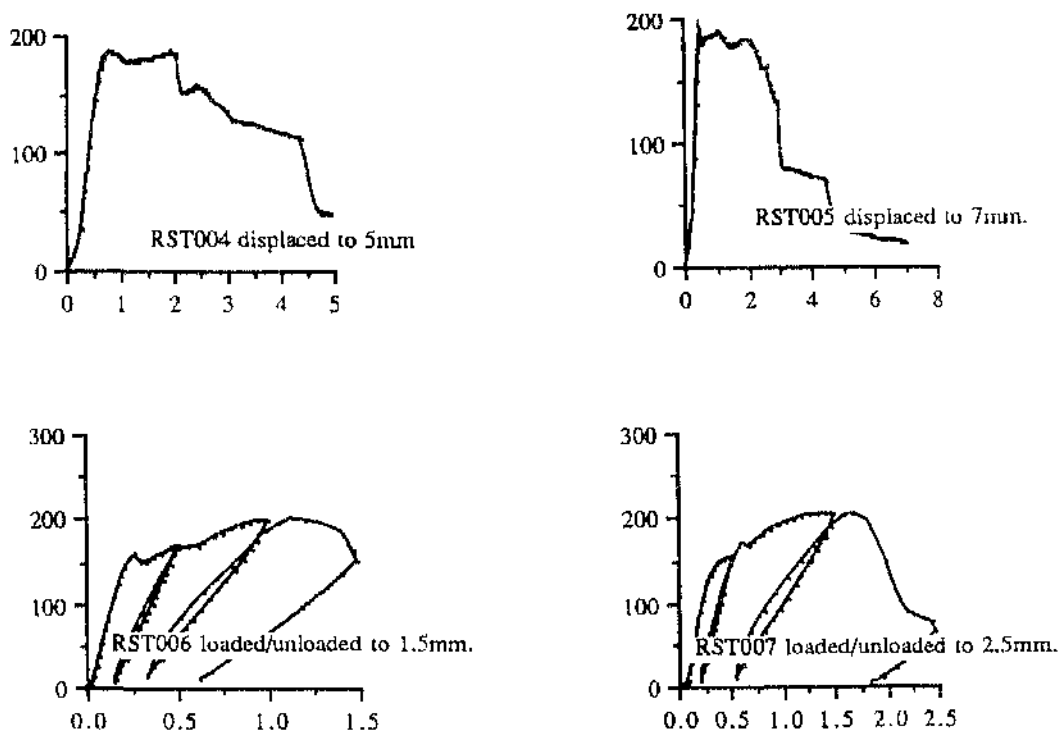


Fig 3.2.4 Load-displacement curves for Dupont Lanxide T-Sections (RST) at 1273K

3.3 Discussion

The ceramic composite materials behaved similarly to the experimental observations conducted by Mecholsky (1986) undergoing three distinctive stages prior to failure: a linear elastic response before matrix micro-cracking, a non-linear region with increasing load and displacement where multiple matrix cracking occurs and a region of decreasing load with increasing displacement where micro-cracking reaches saturation and fibre pullout occurs. The model material composites showed only Stages 1 and 2. The three model material polymer/polymer composites the bend bar, the thickened section and the t-section stress and strain levels to failure couldn't be measured since the materials exhibited a large degree of ductility. Tables 3.1-3.9 show the measured values obtained from each test.

The key mechanical properties of ceramic composites include the elastic constants, including Young's modulus, the rigidity and Poisson's ratio. From the three-point monotonic and cyclic flexure tests a number of key mechanical properties were measured including the rigidity or stiffness (K) from which the modulus in the inplane direction (E_1) can be established. For complex geometries, such as the thickened section and the t-section, establishing an *exact* elastic modulus is problematic. An approximate modulus, obtained from the bend bar can be used to analyse these structures. The onset of matrix failure (OMF), in particular the stress at which the micro-cracking commences σ_m , is an important property for developing and understanding new composite materials. This critical design limit for turbine components (Butler & Lewis (1991)) was calculated from each P- δ graph. Average stress σ values were derived from

$$\sigma = \frac{3 PL}{2bd^2} \quad (3.3)$$

for a given load. From this and the elastic modulus of the material, the strain ϵ values were calculated.

The inelastic strain components of a cyclic test can be determined from residual displacements measured from each cyclic P- δ graph (section 4.6). Also calculated, but not tabulated in chapter 3, were the strain energy release rates (G), calculated by the assistance of the software package Mathematica by integrating the areas under each hysteresis curve. After a series of tests were complete, the crack length was measured.

3.4 Conclusions

An approximate modulus, obtained from the bend bar, was used for the thickened section and the t-section since calculating an *exact* elastic modulus was problematic. Apart from the incompleteness of the materials database, the stiffness (K) for these complex geometries are sufficient in allowing their performance to be established and compared. Measuring the crack length (a_c) accurately for these geometries was also prone to error and in many cases, the data tables omitted these values since the number of tests conducted was considered to be insufficient. The Amercom 3-D braided SiC/SiC composite tests were halted due to the poor quality and porosity of the material. Due to the small quantity of each batch (<12) of material tested, a statistical approach (Weibulls modulus) wasn't appropriate.

Test No	E1 (GPa)	K1 (N/mm)	E2 (GPa)	K2 (N/mm)	OMF (MPa)	No Cycles
RSB010	130	352	-	-	150	1
RSB011	140	439	-	-	150	1
RSB012	Not Recieved					
RSB013	124	387	84	262	152	1
RSB014	Not Recieved					
RSB015	125	390	81	252	145	1
	83	259	24	73		2
	40	125	13	40		3
RSB016	107	323	106	321	139	1
	105	320	83	252	-	2
	98	298	38	114	-	3
RSB017	133	427	109	352	155	1
	123	396	82	265	-	2
	112	359	27	86	-	3
RSB018	129	403	105	368	150	1
	116	362	56	174		2
RSB019	Not Tested					
RSB020	Not Tested					
Am003	85	267			52	1

Table 3.7 Dupont Lanxide Bend Bar (RSB)/Amercom(Am) at 1000C

Test No	E1 (GPa)	K1 (N/mm)	E2 (GPa)	K2 (N/mm)	OMF (MPa)	No Cycles
RSR005	x	1705	-	-	270	1
RSR006	x	1393	x	1393	192	1
	x	1366	x	1193		2
	x	1216	x	978		3
RSR007	x	1355	x	870	184	1
	x	1036	x	422		2
	x	330	x	-		3
RSR008	x	992	x	982	177	1
	x	985	x	602		2
	x	583	x	347		3
RSR009	}	}Not Tested				
RSR010	}					

Table 3.8 Dupont Lanxide Wedge Section (RSR) at 1000C

Test No	E1 (GPa)	K1 (N/mm)	E2 (GPa)	K2 (N/mm)	OMF (MPa)	No Cycles
RST004	x	528	x	-	105	1
RST005	x	683	x	-	150	1
RST006	x	830	x	455	123	1
	x	641		265		2
	x	399		161		3
RST007	x	777	x	494	125	1
	x	534	x	195		2
	x	243	x	96		3
RST008	}					
RST009	}	}All Not Tested				
RST010	}					

Table 3.9 Dupont Lanxide T-Section (RST) at 1000C

Chapter 4

Test Programme Initial Observations

4.0 Introduction

To confirm the validity of the model material, various model and ceramic sub-elements were subjected to monotonic and cyclic loading and the results non-dimensionalised and compared. The load-displacement (stress-strain) responses were normalised by their microcracking stress σ_m and strain ϵ_m values. This work must be complemented by the development of high-temperature test procedures which allow the identification and specification of appropriate design parameters. Dupont Lanxide (SiC/Al₂O₃) and Amercom (SiC/SiC) ceramic composite sub-elements tested at ambient conditions and 1273K are compared for monotonic and cyclic load tests.

Only one measurement of strength or life can be made for one specimen and so it is very difficult to compare evolving damage states between two specimens tested to failure. However stiffness can be measured frequently during damage development, and can be measured without destroying the material. Cyclic load/unload tests allow the decay in the loading elastic modulus (E1) and the unloading modulus (E2) to be determined and are used as a measure of damage in the sub-elements.

As a precursor to the stress analysis of the sub-elements geometric solid modelling of the sub-elements was carried out using Catia FE solver ABAQUS v 5.2 1st order plane strain elements. The residual deformation (δ_r) behaviour and the strain energy release rate (G), associated with delamination growth, was determined from each cyclic load/unload test. Crack initiation and propagation through the sub-element geometries were examined after bend testing using optical and a scanning electron microscopes.

4.1 Non-Dimensionalised Comparative Graphs

The Butler model composite is compared to the ceramic composite in figure 4.1(a). Although each system differs in absolute terms, by non-dimensioning the load and displacement by their micro-cracking load (P_m) and displacement (d_m) the responses are found to be similar as shown in fig 4.1(b). Though the ceramic composite system is 'stiff and strong' and the polymer composite system is the opposite, they do show similar deformation and failure modes. This allows fibre-architectures of the polymer composite to be developed and transferred to the expensive ceramic composite system.

In order to confirm the validity of the model material various model and ceramic sub-elements were subjected to monotonic and cyclic loading and the results non-dimensionalised and compared. The load-displacement (stress-strain) responses were normalised by their microcracking stress σ_m and strain ϵ_m values.

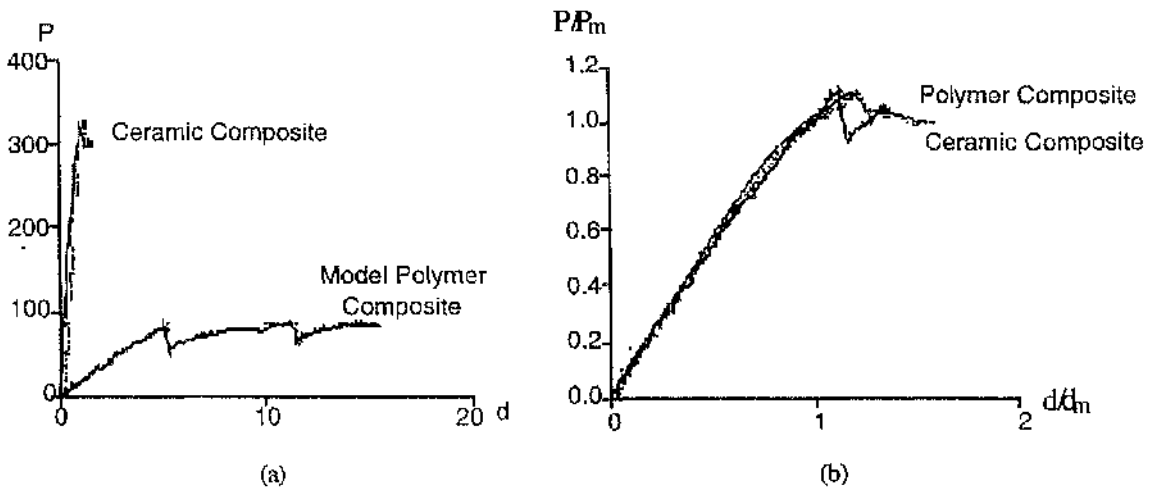


Figure 4.1 (a) Load-displacement curve comparison of Ceramic Composite and Model Polymer Composite.

(b) Non-Dimensionalised comparison of the Polymer Composite and Ceramic Composite

4.1.1 Bend Bars

Flexure tests on the model material 2-D 0/90 laminate implied an elastic modulus (E_1) of 3.97GPa and flexure strength (σ_u) of 62MPa at room temperature. The values obtained agreed with the theoretical equations from the rule of mixtures and are tabulated in table 4.1. The polymer/polymer composite bend bars showed some scatter though an average density was calculated to be 8g/cm³ for an assumed volume fraction (V_f) of 35% and Poissons ratio of 0.29. The moduli E_{22} and the shear stress τ_{12} were estimated to be 0.26GPa and 0.16GPa respectively. Micro-cracking commenced at about 31MPa \pm 3MPa. The initial modulus (E_0) decreased by 14% after being cycled up to a displacement of 7.5mm. Incrementing the cycled displacement below 7.5mm didn't have much effect on reducing the modulus. The strain to failure (ϵ_f) couldn't be measured, due to the ductile nature of the composite.

Fig 4.1.1(a) and fig 4.1.1(b) shows the model material bend bar (MMBB) and Dupont Lanxide bend bar (RSB) normalised. Diagram(a) shows the response of the two materials loaded monotonically to failure. Both curves exhibit similar features. The maximum normalised strength is around $2.2\sigma_m$ for each curve, with matrix fracture (first distinctive drop in load) for each occurring at $2.9\epsilon_m$. Diagram(b) shows the response of the two materials under a cyclic loading/unloading. Again the materials normalised properties and in particular the normalised hysteresis loops are comparable to each other.

Fig 4.1.1(c) shows the model material bend bar and Amercom bend bar (Amercom) normalised. Unlike the normalised graphs for MMBB and RSB, the normalised curves for Amercom and MMBB exhibit no similarities.

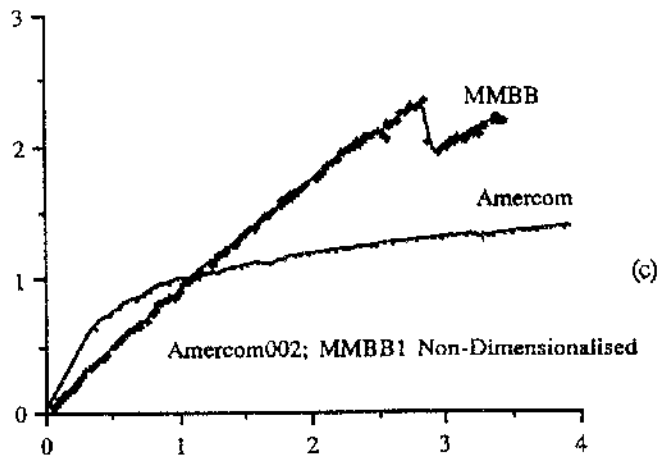
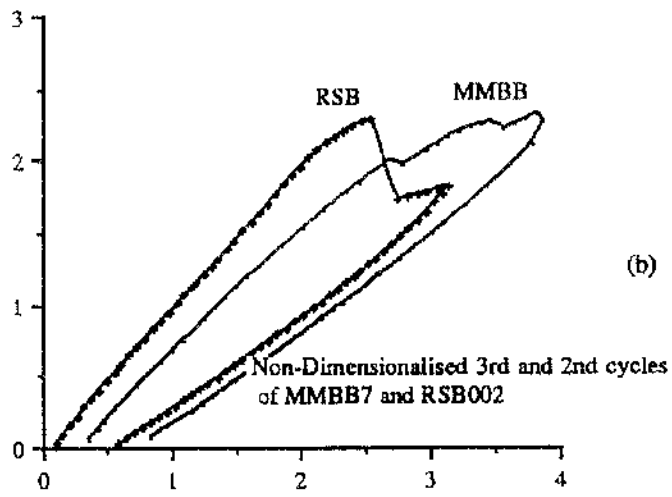
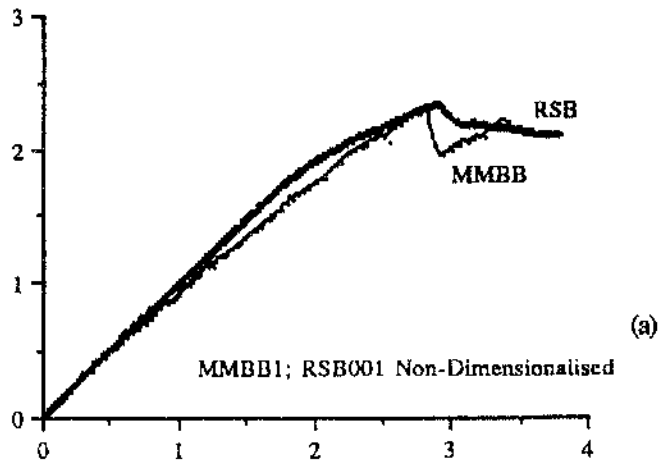


Fig 4.1.1 Bend Bars Non-Dimensionalised

4.1.2 Wedge-Sections

Flexure tests on the model material thickened section show a stiffness (K) of 53kN/m (using a nominal modulus of 4GPa) and a flexure strength (σ_{11}) of 88MPa at room temperature. The inter-laminar moduli E_{22} and the inter-laminar shear stress τ_{12} were estimated to be 0.2GPa and 1.4GPa respectively. The onset of micro-cracking commenced at about 56MPa \pm 3MPa. The values are tabulated in table 4.1. The strain to failure (ϵ_f) couldn't be measured, due to the ductile nature of the composite.

Fig 4.1.2 shows the model wedge section (MMWS) and the Dupont Lanxide reinforced section (RSR) normalised, taken from their respective monotonic stress-strain responses to failure. The normalised linear elastic, matrix fracture levels ($0.6\epsilon_{11}$) are comparable. The normalised strength level for the MMWS however is about 20% larger.

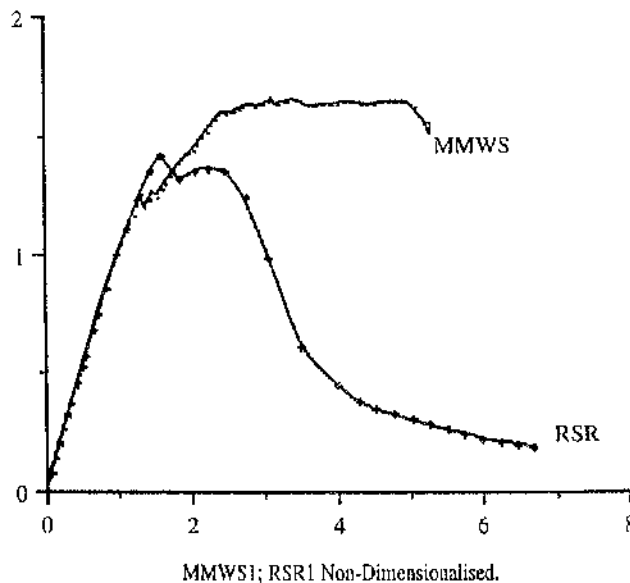


Fig 4.1.2 Non-dimensionalised MMWS and RSR

4.1.3 T-Sections

Flexure tests on the model material t-section obtained a stiffness (K) of 12.4kN/m (using a nominal modulus of 4GPa) and a flexure strength (σ_u) of 26MPa at room temperature. The moduli E_{22} and the shear stress τ_{12} were estimated to be 3.6GPa and 0.12GPa respectively. Micro-cracking commenced at about 13MPa \pm 3MPa. The values are tabulated in table 4.1. The strain to failure (ϵ_f) couldn't be measured, due to the ductile nature of the composite.

Fig 4.1.3 shows the model t-section (MMTS) and the Dupont Lanxide T-Section (RST) normalised, taken from their respective monotonic stress-strain responses to failure. The normalised linear elastic, matrix fracture levels ($0.7\epsilon_m$) are comparable. The normalised strength level for the MMTS however is about 15% larger.

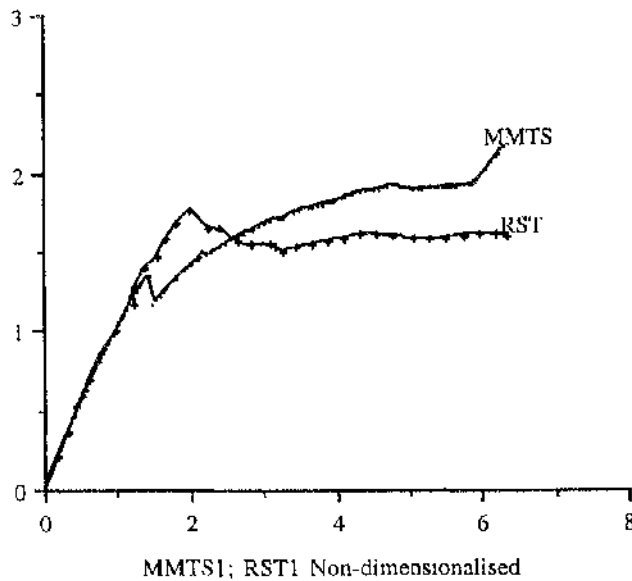


Fig 4.1.3 Non-dimensionalised MMTS and RST

Material	Temp (C)	E_{11} (GPa)	E_{22} (GPa)	τ_{12} (GPa)	σ_m (MPa)	σ_u (MPa)	ϵ_f
<u>Bend Bar</u>							
MMBB	20	3.97	0.26	0.16	31	62	N/A
<u>Thicken Section</u>							
MMWS	20	4	0.2	1.4	56	88	N/A
<u>T-Section</u>							
MMTS	20	4	3.6	0.12	13	26	N/A

Table 4.1 Model material polymer/polymer composite mechanical properties

4.1.4 Discussion

The normalised monotonic and cyclic bend bars curves for the model polymer system and ceramic composite (SiC/Al₂O₃) system are generally similar to each other. Discrepancies in the cyclic hysteresis curves can be attributed to the difficulty of assessing the exact point where microcracking commences. The normalised monotonic curves for the Amercom composite system and the polymer composite exhibit no similarities. Since the polymer composite system was developed to behave as a substitute for the SiC/SiC system, the normalised Amercom composite would require its own model material system to be developed to mimic its deformation and failure patterns.

The normalised curves for the thickened(wedge) sections for the polymer composite and the ceramic(SiC/Al₂O₃) composite each have a similar linear elastic portion. However while the normalised strength level for the polymer composite system remains constant for a constant increase in displacement, the ceramic (SiC/Al₂O₃) composite shows a gradual decline in strength after reaching its maximum stress level.

The normalised curves for the t-section polymer system and the SiC/Al₂O₃ system are in close agreement with each other. Slight discrepancies between the normalised strength levels may be attributed to calculating the absolute point of micro-cracking.

4.1.5 Conclusions

The utility of producing a low cost polyester-polyester composite system to behave as a model material and simulate the Dupont Lanxide SiC/Al₂O₃ ceramic composite system has been demonstrated, at least for ambient conditions. Any discrepancies between some of the model material and ceramic composite normalised curves can be attributed to the difficulty of assessing the exact point where microcracking commences. The inability of the model material to simulate Amercom SiC/SiC may be due to the lack of penetration of the matrix into the fibres. Validation of finite element models of the materials has been proven by the tests.

4.2 Mechanical and Thermomechanical Property Observations

The mechanical properties measured at room and 1273K temperature for the three geometric ceramic composite (bar, wedge, t-section) sub-elements are discussed. Dupont Lanxide (SiC/Al₂O₃) and Amercom (SiC/SiC) ceramic composite sub-elements tested at ambient conditions and 1273K are compared for monotonic and cyclic load tests.

4.2.1 Bend Bars

The 2-D laminated Nicalon-reinforced alumina (SiC/Al₂O₃) had on average an elastic modulus (E_1) of 132GPa and flexure strength (σ_u) of 380MPa at room temperature. This disagreed with the Dupont Lanxide data sheets which (SEP 1989) gave a value of elastic modulus of 200GPa and a flexural strength of 500MPa. However, tensile data produced by Rolls Royce on the same batch of material produced a tensile modulus of 126GPa and a maximum strength of 270MPa.

Since a material tested in bending generally produces higher flexural strength values than the ultimate tensile strength values produced in tension (Mecholsky, 1986), the flexure modulus and strength would seem to agree more with RR uniaxial tensile results, than with the SEP data. The average elastic modulus, for flexure, is on the low side, a more appropriate average would probably be 140GPa since the first two bend bars RSB001 and RSB002 were 30GPa and 38GPa lower in stiffness than the rest of the batch. Microcracking commenced at about 156MPa \pm 20MPa. Cycling the material incrementally from 1.5mm to 2.5mm and 3.5mm resulted in a decrease from the initial modulus E_0 by 22%, 40% and 50% respectively. Increasing the displacement beyond 3.5mm, the materials modulus decreased up to failure (ϵ_f) at a strain of 0.032. The residual displacement (δ_r) for the bend bar cycled to the above displacements of 1.5mm, 2.5 and 3.5mm increased by 17%, 45% and 72% respectively. The behaviour of the reversible elastic and residual

displacements are reported in section 4.6. Values for the inter-laminar moduli E_{22} and the inter-laminar shear stress τ_{12} were estimated from the computational analysis that provided, for each sub-element, inplane/interlaminar direct stresses and shear stresses. The FE analysis (section 4.5) was carried out to support the experimental analysis, particularly for complex geometries. As the experimental results agreed well with the FE analysis, some degree of confidence may be placed in estimated E_{22} and τ_{12} . For the SiC/Al₂O₃ composite, E_{22} was estimated to be 8.4GPa and τ_{12} was 61GPa.

Fig 4.2.1 shows the load-displacement responses for Dupont Lanxide Bend Bars (RSB) tested at ambient and 1273K. Diagram(a) compares the ambient (RSB008) and 1273K (RSB013) conditions for the bend bar, displaced to just above the onset of matrix microcracking before being unloaded. The cycle test conducted at 1273K deviates from that at ambient conditions, showing a reduction of elastic modulus of 12%, a reduced linear elastic proportion and a further reduction in strength by 19%. However the reverse is evident by comparing the load/unload response to failure for the cold (RSB007) curve and the monotonically displaced to failure hot curve RSB011 as shown in diagram (b). This would suggest that the differences in both cases are more likely to be due a variation of $\pm 10\%$ in material, caused by the manufacturing process. The bend strength for the 'hot' test was about 18% stronger and is slightly overestimated because matrix cracking causes a shift of the neutral axis of the beam. The apparent stress for flexure testing was calculated from the measured load, assuming a uniform linear-elastic beam in bending. The secant modulus was affected by matrix hardening. Other material characteristics, including strain to failure (0.032) were similar, happening at around 10mm.

Cycling of the SiC/Al₂O₃ composite bend bars up to and beyond 2.5mm, resulted in *near* collapse of the structure (bend bars RSB0015 and RSB016 shown in fig 3.2.1). This is in contrast to the monotonic tests where the strain to failure (ϵ_f) happened around 0.033 (10mm) and load of 60N was retained to a displacement of ~2.5mm. At this displacement, a transition level is evident, where the load rapidly declines with increasing

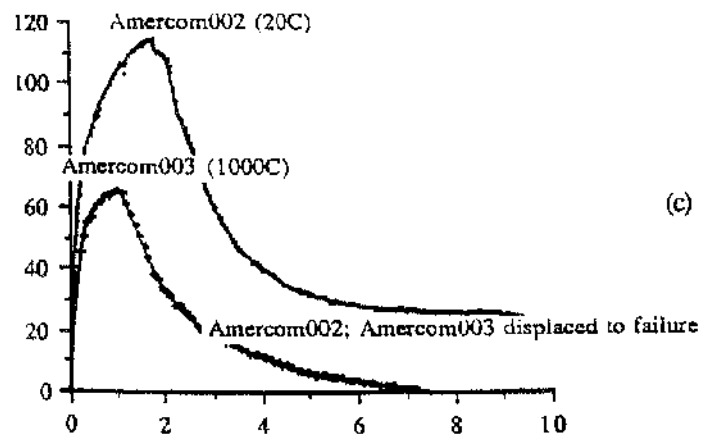
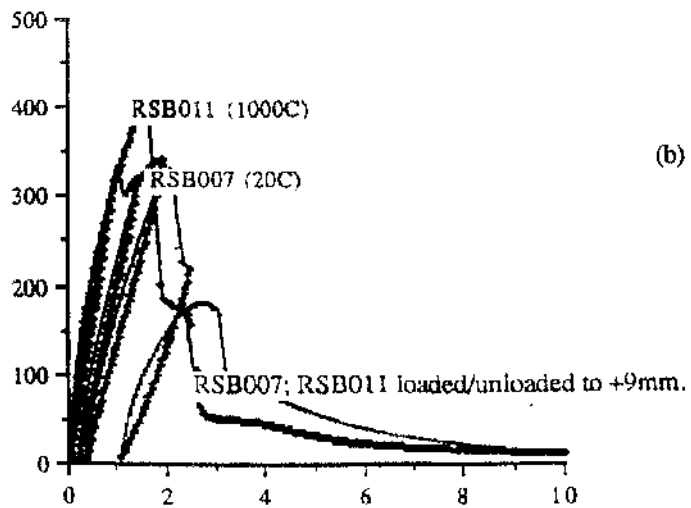
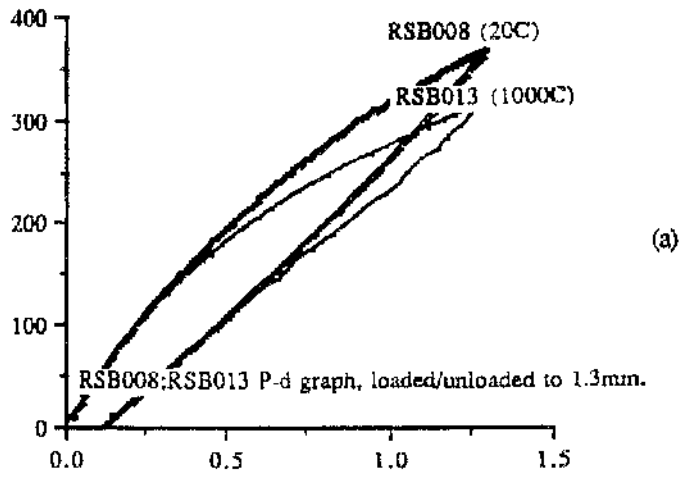


Fig 4.2.1 Bend Bars tested at ambient and 1273K

displacement for the monotonic curves. It would seem that whereas a constant loading can be held beyond the transition level, cycling results in earlier collapse of the structure. This is evident when measuring the increase in residual displacement (δ_r). δ_r increased from 15% up 95% for a cycled displacement of 1.5mm and 2.5mm. δ_r for a cycled displacement of 3.5mm was 100%. Values of the moduli E_{22} and the shear stress τ_{12} were unaffected.

The elastic constants measured at room temperature for the Amercom 3-D braided Nicalon-reinforced silicon carbide (SiC/SiC) obtained a modulus (E_1) of 120GPa and a flexural strength of 138MPa. In comparison to 2-D Nicalon-reinforced silicon carbide (SiC/SiC) (Hillyer (1990), Inghels (1986), Dupont Lanxide Data Sheets (1989)) which has an elastic modulus between 196GPa-235GPa and strength between 223MPa-300MPa, the Amercom 3-D braided composites elastic properties are very low. Values for the transverse modulus and the shear stress couldn't be measured with any degree of certainty. Only one test on the Amercom SiC/SiC at 1273K was carried out because earlier tests at room temperature revealed a poor standard of composite. The comparative load-displacement response for Amercom Bend Bars(Amercom) tested at ambient and 1273K is shown in fig 4.2.1(c). The monotonic 'hot' test showed a 45% drop in strength, a 32% reduction in stiffness and failure at a strain of 0.040 (28% less than ambient).

4.2.2 Thickened (Wedge) Sections

The monotonic load-displacement response for Dupont Lanxide ceramic thickened sections tested at ambient (RSR001) and 1273K (RSR005) is shown in figure 4.2.2. The monotonic 'hot' test shows a 16% drop in strength (σ_u), a stiffness reduction (E_1) of 10%, though the strain to failure was similar to the cold test. Micro-cracking commenced

at about $306\text{MPa} \pm 15\text{MPa}$ and $184\text{MPa} \pm 10\text{MPa}$ for ambient and 1273K respectively.

Cyclic response for the material tested at ambient and 1273K showed the stiffness and strength were again reduced for the 'hot' test. The two type of tests show that the average elastic modulus for the 'hot' tests dropped by 30% and the strength dropping by an average of 24%. This reduced strength however revealed the material to be more ductile compared to the 'cold' test. ie the load bearing capability was still retained at a reduced strength. This was attributed to the shear characteristics of the composite causing the crack to eventually deflect along the fibre axis. The onset of micro-cracking (σ_m) at 1273K was also reduced by an average 23% from ambient values. Cycling the material incrementally from 0.5mm to 1mm and 2mm resulted in a decrease from the initial modulus E_0 by 10%, 40% and 80% respectively. The behaviour of the reversible elastic and residual displacements are reported in section 4.6.

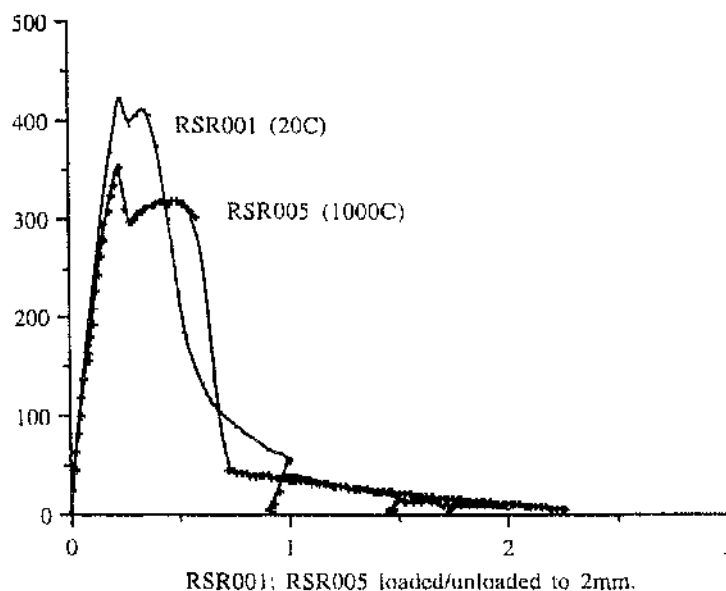


Fig 4.2.2 Dupont Lanxide Wedge Sections (RSR) tested at ambient and 1273K

4.2.3 T-Sections

The monotonic load-displacement responses for Dupont Lanxide ceramic t-sections tested at ambient (RST001) and 1273K (RST005) are shown in figure 4.2.3. The monotonic 'hot' test shows a stiffness reduction of 15% and a reduction of strength by 10%. Cyclic response for the t-section tested at ambient and 1273K displaced up to 2.5mm showed matrix fracture occurring at 1.56mm (306MPa \pm 15MPa). The average elastic modulus for the 'hot' tests dropped equally by 15%. The strains to failure were similar.

The two tests show that the average elastic modulus for the 'hot' tests dropped by 15% and the strength dropping by an average of 14%. The onset of micro-cracking (σ_m) of 121MPa \pm 6MPa at ambient and 1273K were comparable. Cycling the material incrementally from 0.5mm to 1mm and 2mm resulted in a decrease from the initial modulus E_0 by 10%, 40% and 80% respectively. The behaviour of the reversible elastic and residual displacements are reported in section 4.6.

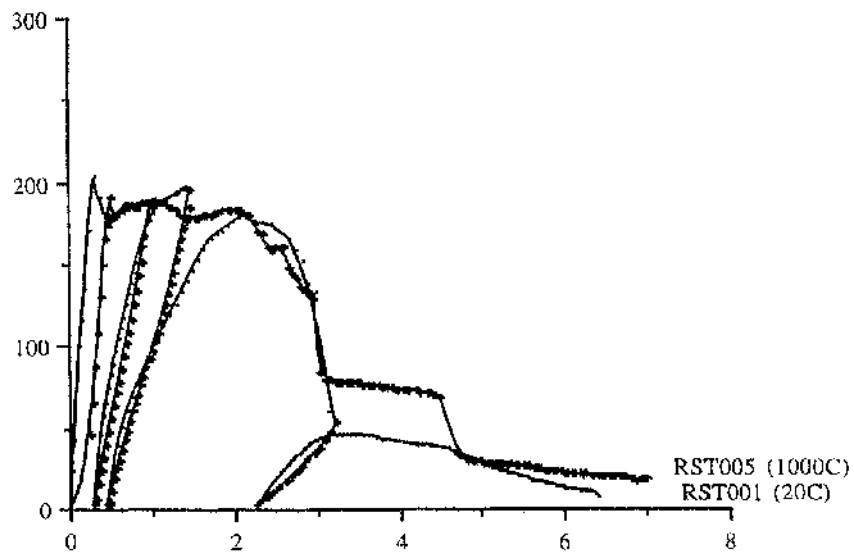


Fig 4.2.3 Dupont Lanxide T-Sections (RST) tested at ambient and 1273K

Material	Temp (C)	E ₁₁ (GPa)	E ₂₂ (GPa)	τ ₁₂ (GPa)	σ _m (MPa)	σ _u (MPa)	ε _f
<u>Bend Bars</u>							
RSB	20	132	8.4	61	156	380	0.032
RSB	1000	127	8.3	60	149	440	0.033
Amercom	20	120	n/a	n/a	68	138	0.033
Amercom	1000	85	n/a	n/a	52	76	0.040
<u>Thicken Sections</u>							
RSR	20	140	4.2	62	310	441	0.030
RSR	1000	94	4.3	60	238	352	0.030
<u>T-Sections</u>							
RST	20	140	142	57	30	49	0.009
RST	1000	119	121	n/a	29	44	0.008

Table 4.2 Ceramic composite mechanical properties at room temperature and 1273K

4.2.4 Discussion

That RSB001 and RSB002 were less stiff than the rest of the batch couldn't be attributed to any cause, other than a manufacturing deficiency. Based on the initial comparison between the cold and hot cycle test up to a displacement of 1.3mm (about microcracking level) it would seem that the hot (1273K) stiffness had been slightly reduced by thermal degradation. This was in contrast to the strength (σ_u) which actually increased in the hot environment. The Amercom bend bars fared poorly when tested at 1273K having a depleted stiffness and strength of 30% and 45% respectively. The microcracking stress also reduced from 68MPa to 52MPa a shift of 24%. The strain to failure seemed similar. The other two geometric sub-elements, the thickened bar (wedge) and the t-section, were affected more severely when tested at 1273K in an air environment, the thickened bar in particular. Tested at 1273K the thickened bar had on average a reduced stiffness and strength in the order of 33% and 20% respectively compared to ambient, with its

microcracking stress level commencing at a lower value of 238MPa, a 23% shift from room temperature tests. Strain to failure was unaffected by temperature. The t-section also had a reduction in its stiffness and strength when tested at 1273K by as much as 15% and 10% respectively, though its microcracking stress levels were unaffected. The t-section was the only geometric specimen to have its transverse moduli reduced when subjected to testing at 1273K by a factor of 15%, the other specimens transverse modulus seemed unchanged. This was the case for the shear modulus results at both room temperature and 1273K, which showed no significant difference.

The elastic properties it seemed were influenced by the level of porosity since pores act as a second phase of zero modulus. It is generally found that porosity reduces Youngs modulus according to a relationship of the form:

$$E=E_0 \exp(-av)$$

where E_0 is the modulus of fully dense material, v is the volume fraction of porosity, and a is a constant determined by Poisson's ratio and also by pore shape and distribution, i.e. is dependent on the microstructure. A universal relationship does not exist. Various authors (Morrell, 1985) have proposed equations to fit experimental data, but all depend on the above material parameters. It has been shown, for example, that the equation:

$$E=E_0[1-1.9v+0.9v^2]$$

is a fair approximation for the case of small, closed, randomly distributed, spherical pores in a material of $v=0.3$, and has been proven for a range of alumina ceramics of different porosities up to 50%. The Amercom materials having a greater porosity, give a reduction in Youngs modulus of appropriately 10-15%. Multiphase materials have moduli intermediate between the values for their constituent phases and to a first approximation,

each phase contributes according to its volume fraction, v_i . The modulus of the composite reduces rapidly as the minor-phase content increases.

$$E = E_1 v_1 + E_2 v_2 + \dots + E_i v_i$$

Moduli were also affected by temperature. Increasing temperature tends to lead to a decreasing modulus, although this is not always the case. Some glass and complex glass-ceramics become stiffer as the temperature is increased. An equation using the temperature coefficient of modulus may be defined as the fractional increase in modulus for each 1K rise in temperature:

$$E_T = E_{25} [1 + \eta_E (T - 25)]$$

$$G_T = G_{25} [1 + \eta_G (T - 25)]$$

for Young's and shear modulus respectively, where η_E and η_G are the respective temperature coefficients.

4.2.5 Conclusions

Testing the SiC/Al₂O₃ composite bend bars at 1273K resulted in no significant change in the state of the elastic modulus (E_1) and the materials strength (σ_u) and the onset of micro-cracking (σ_m). Any discrepancies between the room and elevated temperatures reported in table 4.2 may be attributed to scatter associated with the material. The single test conducted on the Amercom SiC/SiC at 1273K however revealed a poor standard of composite, showing a large drop in strength and reduction in stiffness. Tests were halted on this porous material due its poor quality. The high temperature degradation and oxidation of the surface layer was more predominant in the SiC/Al₂O₃ wedge and, to a

lesser extent, the t-section composite specimens. Both geometries show a reduction in stiffness, the wedge performing poorly with a reduction in all of its other material properties. The wedge system failure mechanism (crack initiation which starts at the reentrant corner propagates across the wedge by fibre pullout) seems to be accelerated by a combination of high temperature degradation involving chemical effects associated with the environment and an increase in fibre pullout. The t-section, which fails by mode I delamination fared well, apart from a slight reduction in its stiffness at 1273K which again was attributed to scatter associated with the material.

4.3 Damage Evolution in Ceramic Composites

Continuum Damage Mechanics (CDM) has evolved as a means of analysing microstructural events such as the microcracking, which occur in engineering ceramics. Whereas fracture mechanics deals with a single well defined crack on the macroscopic level, CDM deals with the collective effect of crack-like defects. The aim of CDM is to describe the influence of material degradation on the stiffness and strength of loaded structures. An intrinsic feature of CDM is the introduction of constitutive variables, either scalar or tensor, as internal variables measuring the material degradation.

Only one measurement of strength or life can be made for one specimen and so it is very difficult to compare evolving damage states between two specimens tested to failure. However stiffness can be measured frequently during damage development, and can be measured without destroying the material.

The damage state is characterised by the parameter, D . For an undamaged state $D=0$, whereas for failure $D=1$. Damage formulations are based on the concept of effective stress and strain equivalence. The matrix stress is the stress experienced by the material whose load-bearing area is being reduced, by some damage mechanism eg crack growth. For a material experiencing damage, the matrix stress tensor $\hat{\sigma}$ can be expressed as:

$$\text{strain}(\epsilon) = \frac{\sigma}{(1-D)} \epsilon \quad (4.3.1)$$

where σ is the nominal stress tensor. Strain equivalence postulates that any strain-based constitutive equation for a damaged material can be written in the same manner as for an undamaged material except that the matrix stress replaces the nominal or aggregate stress. Therefore, for a one-dimensional, isotropic case

$$\text{strain}(\epsilon) = \frac{\hat{\sigma}}{E} = \frac{\sigma}{E(1-D)} \quad (4.3.2)$$

This can be expressed in terms of elastic moduli as proposed by Lemaitre and Chaboche (1978) as

$$D = 1 - \frac{\bar{E}}{E} \quad (4.3.3)$$

where E is the undamaged elastic modulus and \bar{E} is the apparent elastic modulus of the damaged material. Damage can, therefore, be monitored through its effect on the stress/strain response. According to several authors (Kachanov, 1986; Sorensen, 1993) \bar{E} can be best identified experimentally using the unloading elastic modulus of the material. This procedure is especially important if the damage is uniformly distributed throughout the volume over which strain is measured. D may therefore be obtained by measuring the load-displacement (stress-strain) response of the material as shown in fig 4.3(b). For inelastic deformation, D may be established by a set of simultaneous equations:

$$D = 1 - \frac{E'}{E} \quad (4.3.4)$$

$$D' = 1 - \frac{E''}{E} \quad (4.3.5)$$

Inelastic deformation due to, say, plasticity is not the same as inelastic deformation due to microcracking, shown in the figures 4.3 (a) and 4.3 (b) respectively. When E is unaffected by damage all of the elastic loading/unloading lines should be parallel to each other as in the case of fig 4.3 (a). However this is usually never the case as the elastic modulus decreases slightly as strain and hence damage accumulates, as illustrated in fig 4.3 (b).

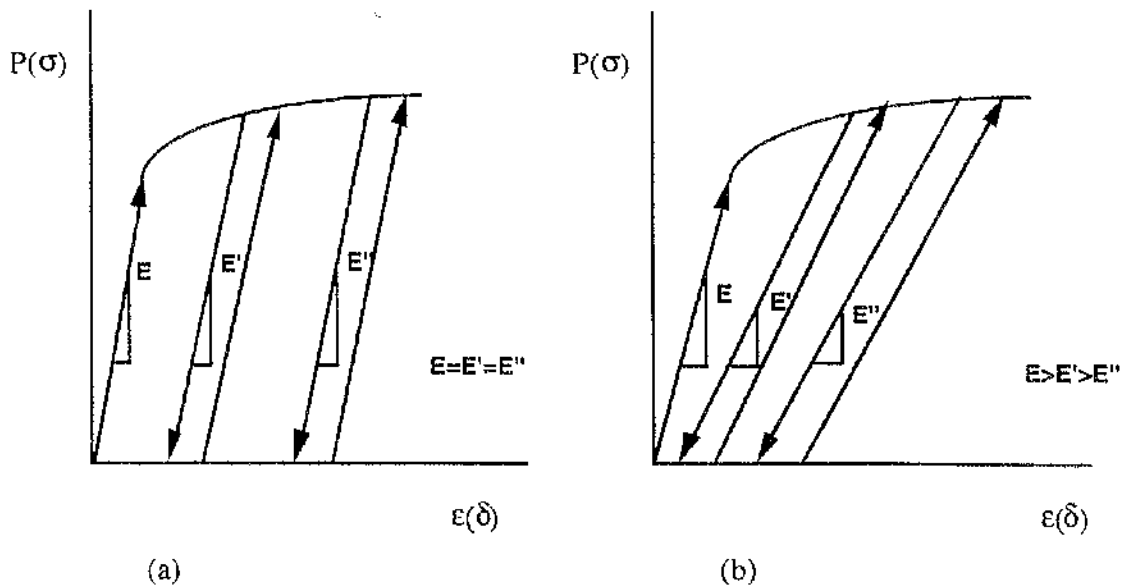


Figure 4.3. Flexure loading/unloading response (a) Inelastic deformation, no damage (b) Inelastic deformation, damage

4.3.1 Modulus Decay Curves

The decay in apparent elastic modulus is introduced as a practical damage analogue since the change in modulus with cycles can be directly related to stress redistribution taking place when internal damage develops in the material (Jessen & Plumtree, 1991). Figures 4.3.1 show the decay in elastic modulus as a function of displacement for each of the sub-elements tested (the Amercom bend bar was omitted, due to insufficient data).

Figure 4.3.1(a) plots the reload elastic modulus, E_I normalised by the initial elastic modulus E_0 as a function of displacement for the three groups of bend bars tested i.e. MMBB, RSB(ambient), RSB(1273K). The decay in the reload modulus of MMBB is small in comparison to that of the Dupont Lanxide bend bars. E for MMBB decreased by 15% for an inelastic displacement of 1.2mm. For an equivalent inelastic displacement, RSB ambient and RSB(1273K) moduli decreased by 50% and 85% respectively

Figure 4.3.1(b) plots the unload elastic modulus, E_2 normalised by the initial elastic modulus E_0 as a function of displacement for the three groups of bend bars tested. The decay in the unload modulus of MMBB was 30% for a displacement of 8mm. RSB(ambient) and the RSB(1273K) unload moduli decrease to almost zero for a displacement of approximately 6.2mm.

Figure 4.3.1(c) plots the unload elastic modulus, E_2 normalised by the initial elastic modulus E_0 , as a function of displacement for the three groups of thickened sections tested ie MMWS, RSR, RSR (1273K). The decay in the unload modulus of MMWS was approximately 70% for a displacement of 10mm. RSR (ambient) and RSB (1273K) moduli both decreased to near zero, for a displacement of 4mm.

Figure 4.3.1(d) plots the unload elastic modulus, E_2 normalised by the initial elastic modulus E_0 , as a function of displacement for the three groups of T-Sections tested ie MMTS, RST (ambient), RST (1000C). The decay in the unload modulus of MMTS was approximately 50% for a displacement of 14mm. RST (ambient) and RST (1273K), moduli decreased to near zero for a displacement of 5mm.

The general trend indicated by the plots is that as the crack density increases (ie number of cracks per mm), the stiffness decreases. Cyclic failure was characterised by the development of initial damage mechanisms such as fibre fracture, debonding and transverse and shear matrix failure followed by the development of later stage mechanisms such as longitudinal splitting and delamination. At the lower stress levels, microstructural flaws were important in the initiation of damage. Their influence on the development of damage decreased with increasing stress to the rapid depletion of crack initiation sites and the accompanying stress redistributions. Longitudinal matrix cracking and delamination were associated with structural flaws such as resin-rich regions containing misaligned fibres. Transverse cracking and branching appears early in the bend bar materials, the stiffness decrease being essentially due to this damage until transverse

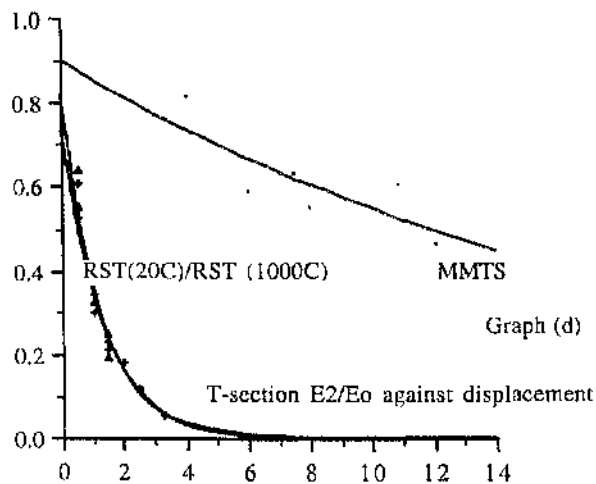
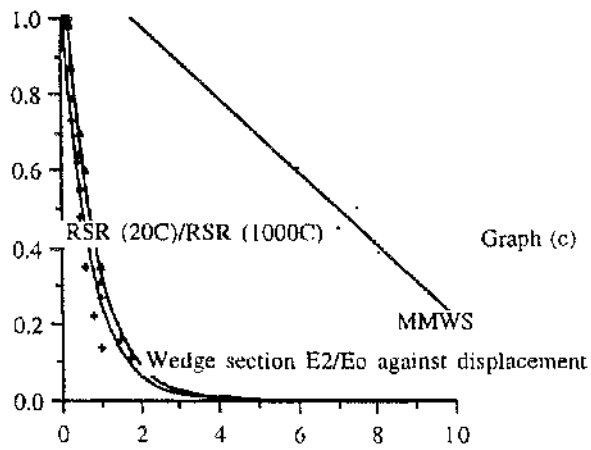
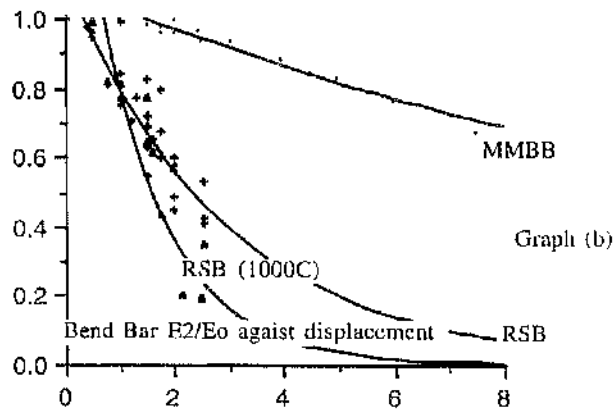
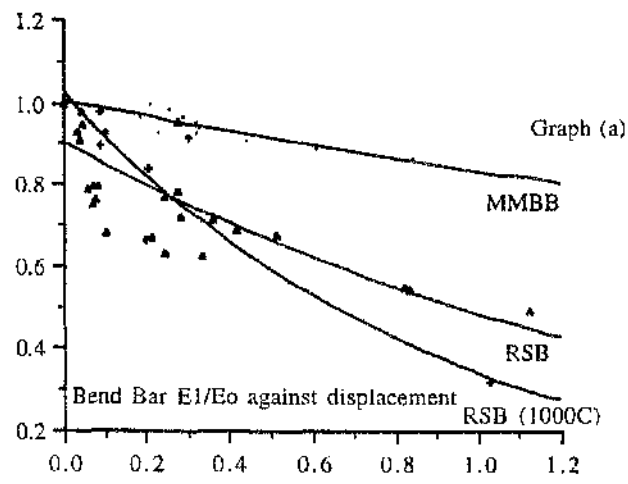


Fig 4.3.1 Modulus Decay Curves

crack saturation. Longitudinal cracking propagates very fast through the stiffer ceramic composites, in particular the t-sections. Failure maps can be seen in section 4.4 showing crack growth and propagation through the sub-element geometries.

4.3.2 Calculation of the Damage (D) parameters

From the loading-unloading curves of the three sub-elements, the damage, D was estimated using equation (4.3.4) and (4.3.5) and plotted against displacement. The damage curves are shown in figures 4.3.2(a)-(c). The damage in the bend bar materials, fig 4.3.2(a), can be related to displacement through a best fit quadratic expression, as follows;

$$\text{Model Material Bend Bar (MMBB): } D=0.0032x^2+0.02x-0.021 \quad (4.3.6)$$

$$\text{Dupont Lanxide Bend Bar (RSB): } D=-0.0017x^2+0.26x-0.076 \quad (4.3.7)$$

$$\text{Dupont Lanxide Bend Bar (RSB) at 1000C: } D=-0.051x^2+0.52x-0.26 \quad (4.3.8)$$

The damage curves for the thickened(wedge) section materials, fig 4.3.2(b), can also be approximated as follows;

$$\text{Model Material Wedge Sections (MMWS): } D=-0.0036x^2+0.04x-0.016 \quad (4.3.9)$$

$$\text{Dupont Lanxide Wedge Sections (RSR): } D=-0.36x^3+1.54x^2-2.3x-0.32 \quad (4.3.10)$$

$$\text{Dupont Lanxide Wedge Sections (RSR, 1000C): } D=0.075x^3+0.47x^2-1.2x-0.15 \quad (4.3.11)$$

The damage curves for the T-Section materials, fig 4.3.2(c), can also be approximated as follows;

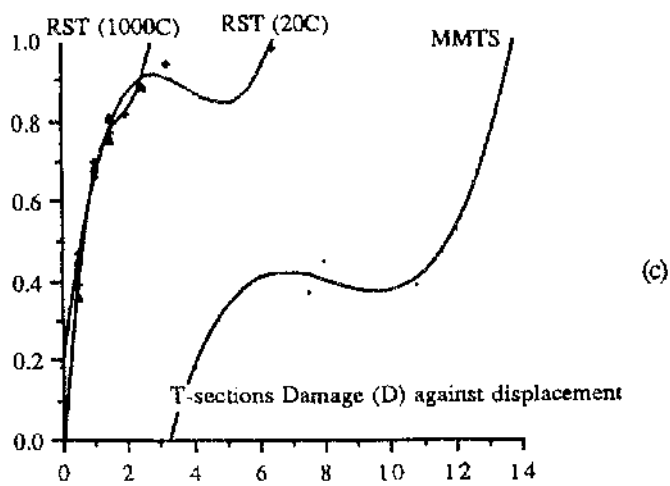
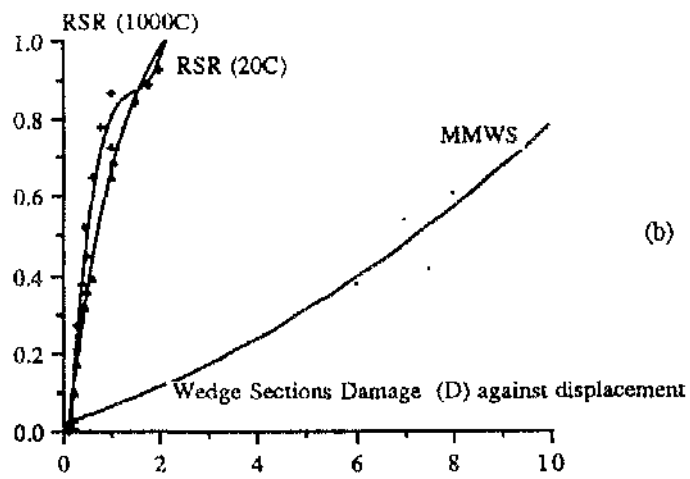
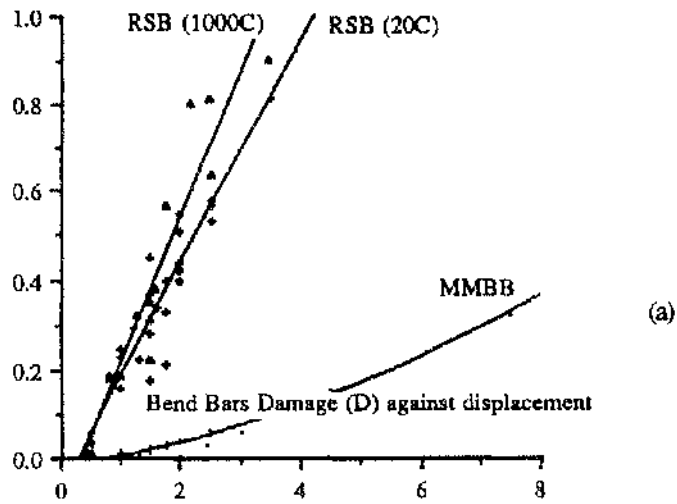


Fig 4.3.2 Damage (D) Curves plotted against displacement (mm)

Model Material T-Sections (MMTS): $D = 0.0043x^3 - 0.11x^2 + 0.84x - 1.88$ (4.3.12)

Dupont Lanxide T-Sections (RST): $D = 0.015x^3 - 0.18x^2 + 0.64x + 0.18$ (4.3.13)

Dupont Lanxide T-Sections (RST) at 1000C: $D = 0.14x^3 - 0.76x^2 + 1.45x - 0.14$ (4.3.14)

4.3.3 Discussion

Modulus decay has provided a valuable tool to monitor cyclic damage development in composite materials. The curves show the rapid development of damage in the stiff, but brittle ceramic composites, relative to the that in the more compliant polyester model material. The cyclic tests show the decay in modulus, as a result of damage for the three geometric sub-elements. The ceramic composite t-section and ceramic composite thickened section show similar decay curves when the unload modulus E_2 is plotted as a function of displacement. The ceramic bend bar behaved differently from the other two geometries. The decay in the ceramic bend bar modulus was more gradual compared to that of the wedge/t sections. A decay of 30%/mm up to 2mm was shown, but this gradually reduces until complete failure occurs at 6mm. The wedge and t-sections decayed at a rate of 70%/mm, with complete failure at around 4mm.

4.3.4 Conclusions

The progressive reduction in modulus can be measured using the Continuum damage mechanics approach to analyse the loading history of cyclically loaded sub-elements such as those presented earlier. Thus for a known displacement, δ , the amount of damage in the composite material, D , can be estimated using equations (4.3.6) to (4.3.14). Once D is known, the component stiffness as well as material elastic modulus E' can be estimated using equation (4.3.2). These are unique damage-displacement relationships for model

and ceramic composites subjected to flexure loading conditions and provide a valuable tool in engineering design. Since the damage parameter, D , describes the stiffness loss, strain in a particular region of the composite can be related to loss in stiffness. The effect of temperature on degradation of the ceramic systems was shown to be minimal.

4.4 Crack Growth Mechanisms-Optical and Fractographic Examination

Crack initiation and propagation through the sub-element geometries were examined after bend testing at room temperature using optical and a scanning electron microscope. The specimens examined optically were first sectioned then placed in a polyester mould, ground and polished. The SEM specimens were sectioned by a diamond saw, cemented onto an SEM stub and given a splutter of gold coating ($\approx 1\mu\text{m}$ thick).

4.4.1 Bend Bars

Fig 4.4.1(a) shows the initiation of cracking from a fibre tow on the tensile surface of the model material bend bars, subjected to a flexure displacement of 2.5mm or $\frac{\delta}{w}=0.714$ (where δ is the displacement and w is the materials thickness). The displacement is just after the microcracking displacement of 2.417mm. As the model material bend bar is deformed further ($\frac{\delta}{w}=1.714$) the progression of the crack can be followed as shown in fig 4.4.1(b). The single crack has now been joined by other independently-produced equally spaced cracks, which are deflected in both directions as they progress through the polyester matrix to the fibre bundles. The number of microcracks eventually increases until saturation occurs (at $\epsilon=0.110$), and no further microcracking occurs.

Fig 4.4.1(c) shows the crack initiation and crack deflection, up to the first fibre bundle, for $\frac{\delta}{w}=0.83$ for the Dupont Lanxide SiC/Al₂O₃ ceramic composite bend bar. Microcracking for the ceramic bend bar occurs at a strain of 0.0012, equivalent to $\frac{\delta}{w}=0.12$. As the ceramic bend bar is further displaced, as shown in fig 4.4.1(d), to $\frac{\delta}{w}=1.17$ the crack deflects and branches through the test bar. During subsequent increases in displacement the cracks continued to open and branch through the material, causing greater damage to the fibre bundles through which the main crack travels. Failure of the

ceramic bend bar occurred at $\frac{\delta}{w} = 3$ as shown in fig 4.4.1(e). Fig 4.4.1(f) shows the fractured surface of the bend bar taken to $\frac{\delta}{w} = 3$. The photograph was taken at the mid-surface, or the fourth bundle of fibres, and reveals evidence of fibre pullout.

The Amercom bend bar cyclic displaced to $\frac{\delta}{w} = 0.75$ is shown in fig 4.4.1(g), but the crack path through this material wasn't very clear. Due to the porosity of the material fracture would likely take place from pore to pore. The pores would normally play an important part in arresting the crack, therefore increasing the amount of work required to fracture the material further, but there seemed little evidence of this occurring. When displaced to failure, $\frac{\delta}{w} = 3.26$, the fracture surface, fig 4.4.1(h), showed little evidence of matrix infiltration into the fibre bundles.



Figure 4.4.1 (a). Model Material bend bar, crack initiation occurring at fibre tow, cycled to 2.5mm.
Magnification x 160

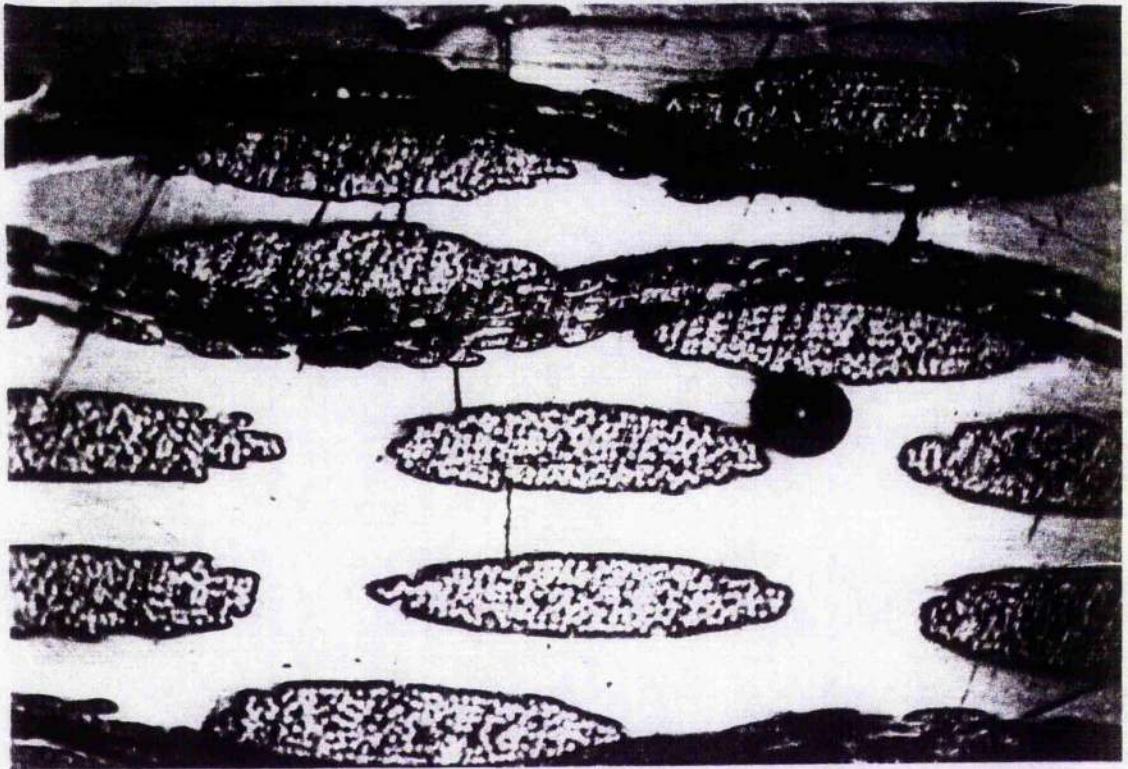


Figure 4.4.1 (b) Crack deflection on tensile surface of model material bend bar after being cycled to 6mm.
Magnification x 70

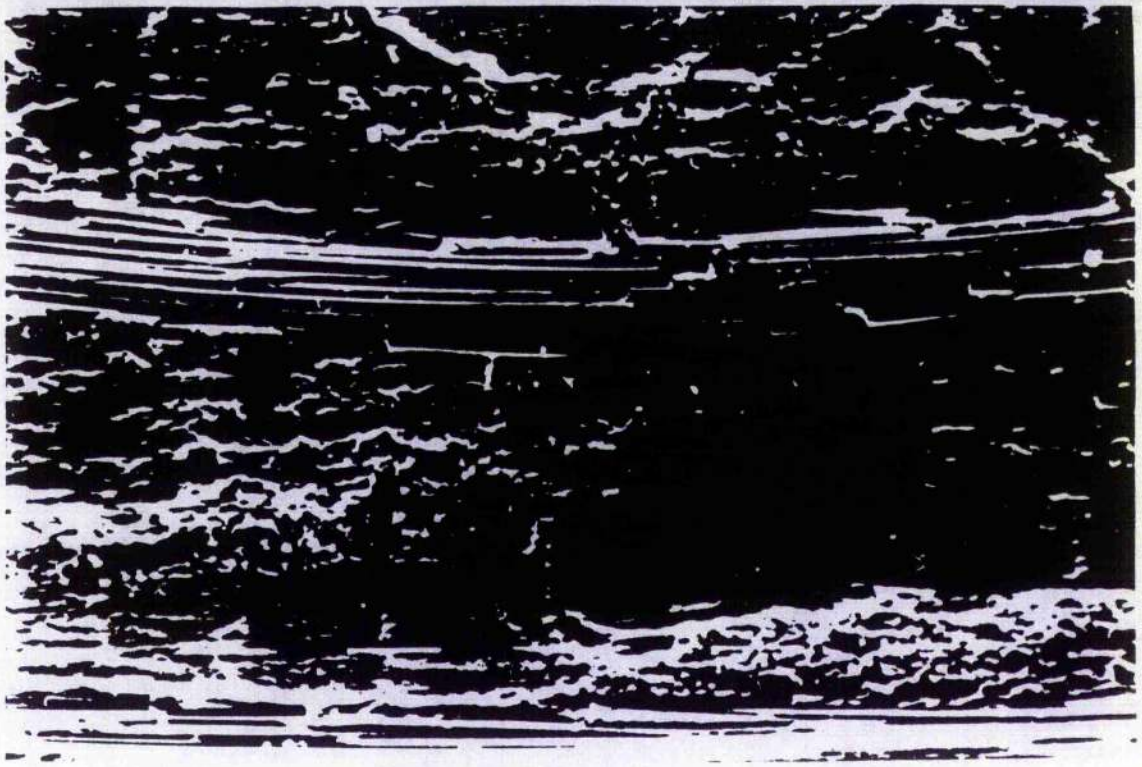


Figure 4.4.1 (c). Crack deflection through fibre bundle of Dupont Lanxide bend bar, cycled to 2.5mm.
Magnification x 80

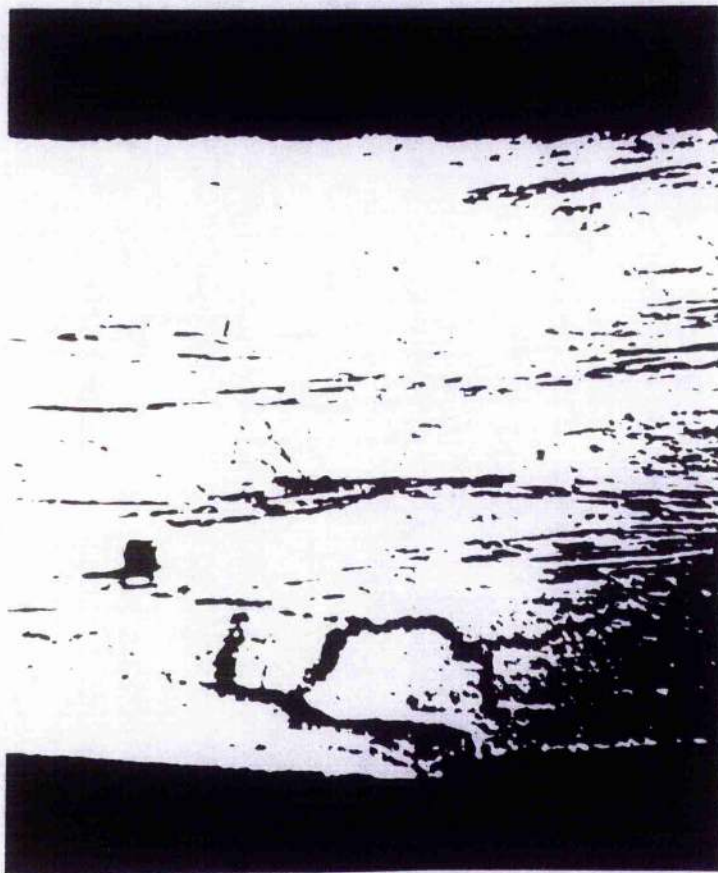


Figure 4.4.1 (d). Crack deflection and branching through Dupont Lanxide bend bar, cycled to 3.5mm.
Magnification x 35

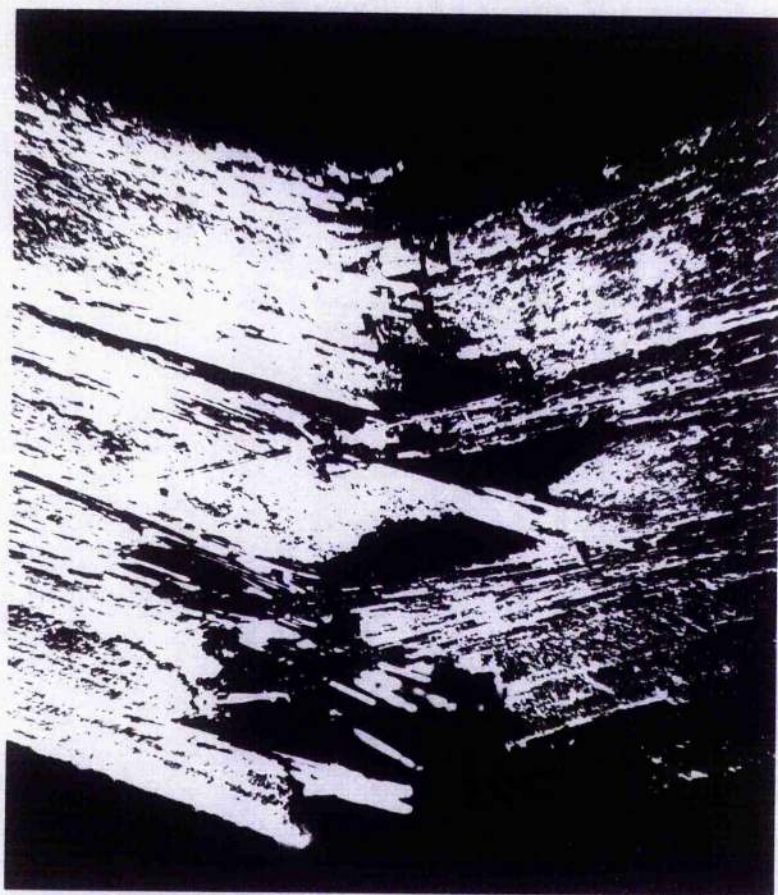


Figure 4.4.1 (e). Dupont Lanxide(DLC) bend bar taken to failure, cycled to 9mm. Magnification x 35

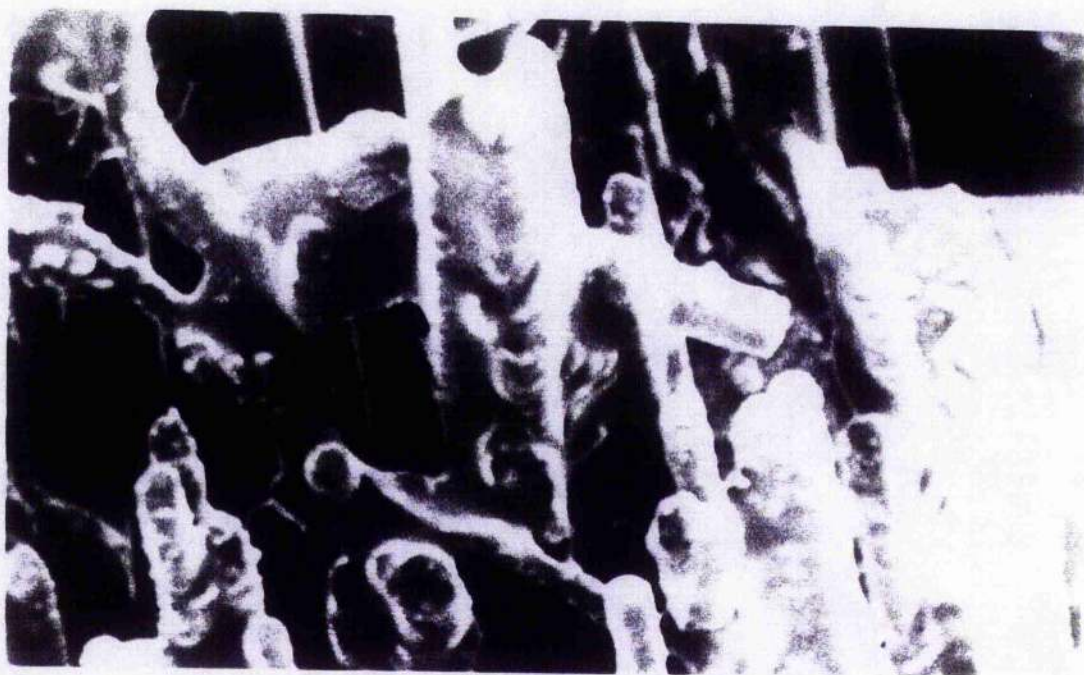


Figure 4.4.1 (f). Tensile fractured surface of DLC bend bar, showing fibre pullout Magnification x 320

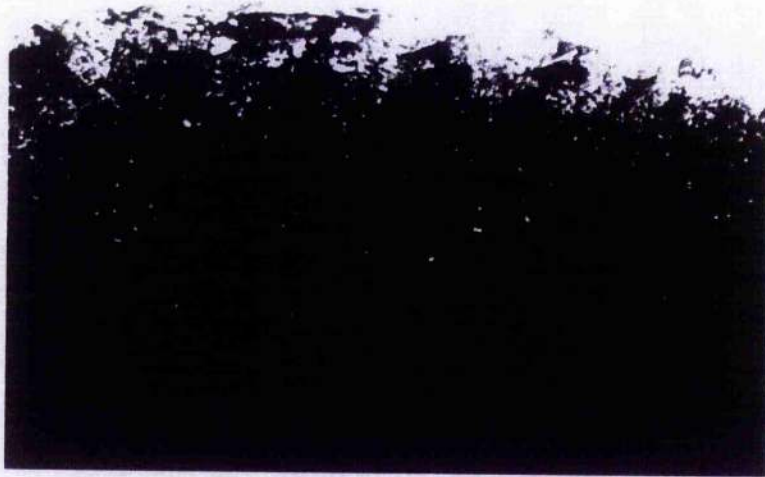


Figure 4.4.1 (g). Amercom bend bar cycled to 2mm. Magnification x 10



Figure 4.4.1 (h). Tensile fractured surface of Amercom bend bar after being displaced to 9.8mm.

4.4.2 Wedge Sections

Crack initiation and propagation of the thickened polyester/polyester composite model material sections tested at room temperature is shown in fig 4.4.2(a). Cracking occurring where the change in the geometric section creates a high stress concentration. This was found to be near the reentrant corner on the tension side (confirmed by computational analysis in section 4.5). Crack propagation passed through the material very rapidly where there was a resin rich matrix, having no fibre bundles to arrest and deflect the fracture.

The SiC/Al₂O₃ ceramic composite thickened section, fig 4.4.2(b), shows a similar nature to crack initiation and deflection for a displacement of $\frac{\delta}{w} = 0.059$. Fig 4.4.2(c) shows a crack deviating and advancing through a fibre bundle. The fibre bundles arrest the fracture somewhat, increasing the work needed to progress the fracture further. As loading continued this crack passed through the matrix material to the next fibre bundle. Increasing the displacement, the crack continued to open and branch causing greater damage to the fibre bundles through which the main crack had already travelled. Final failure of the SiC/Al₂O₃ ceramic composite thickened section is reached at $\frac{\delta}{w} = 0.25$, as shown in fig 4.4.2(d). The fractured surface of a thickened section is shown in figures 4.4.2(e)-(f), showing the crack being deflected by the fibre bundles and fibre pullout occurring.

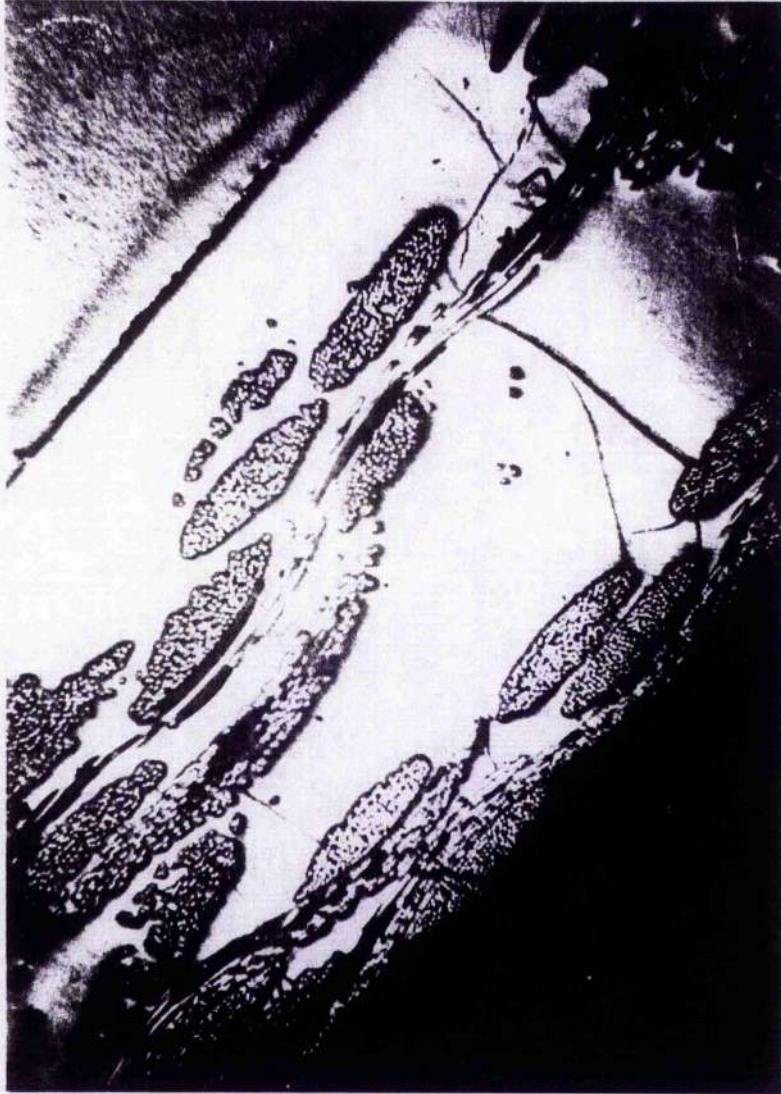


Figure 4.4.2 (a). Crack deflection through a resin rich matrix of the model material thickened section, cycled to 7.5mm. Magnification x 35

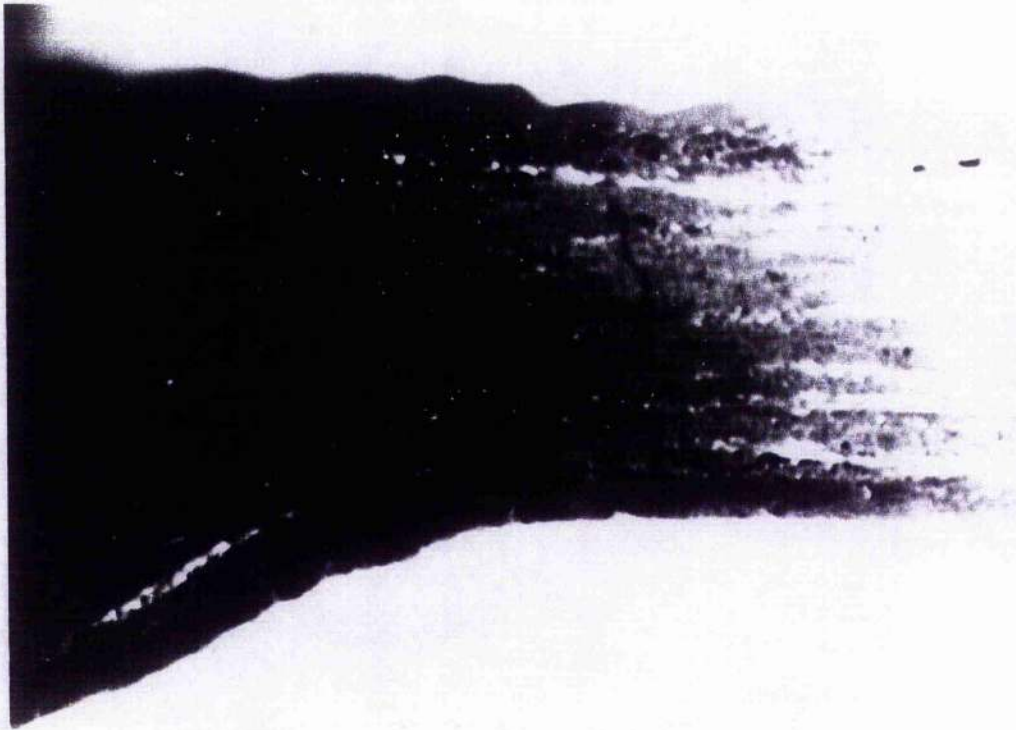


Figure 4.4.2 (b). Crack initiation on Dupont Lanxide thickened section, cycled to 0.472mm. Magnification x 15

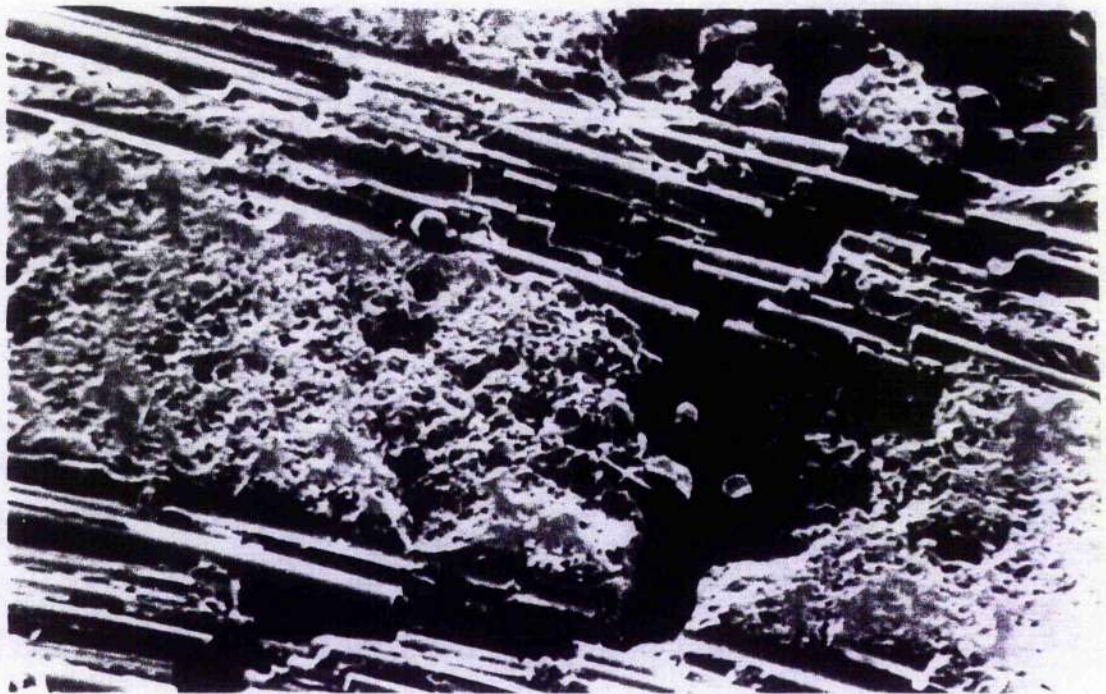


Figure 4.4.2 (c). Crack deflection through fibre tow of DLC wedge section, cycled to 0.472mm. Mag x 160

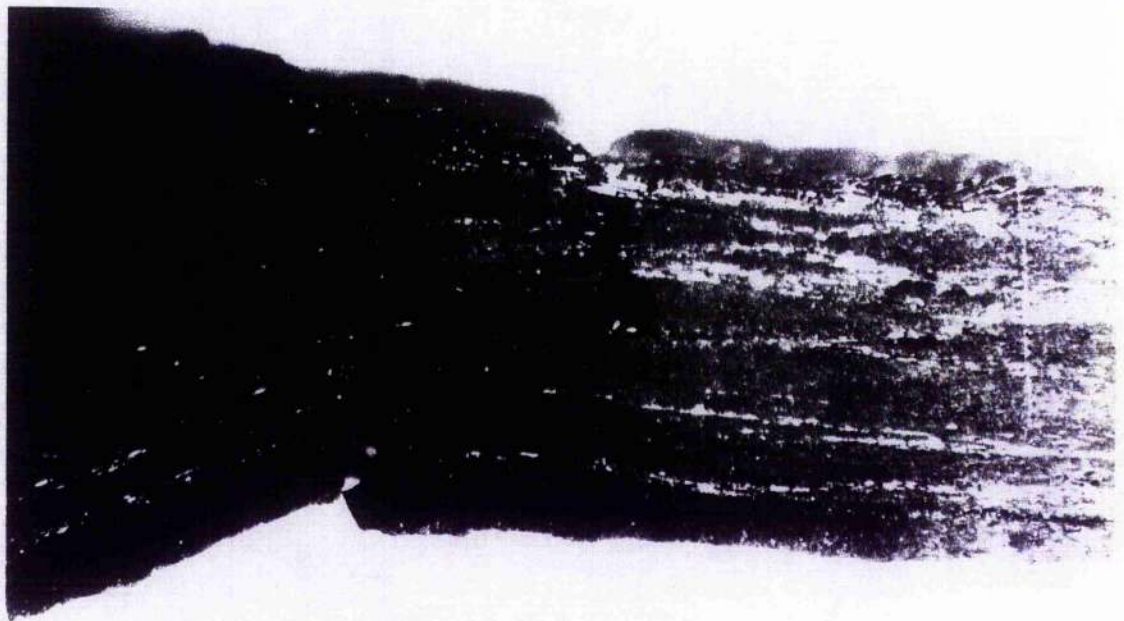


Figure 4.4.2 (d). Dupont Lanxide thickened section taken to failure, cycled to 2mm. Magnification x 15

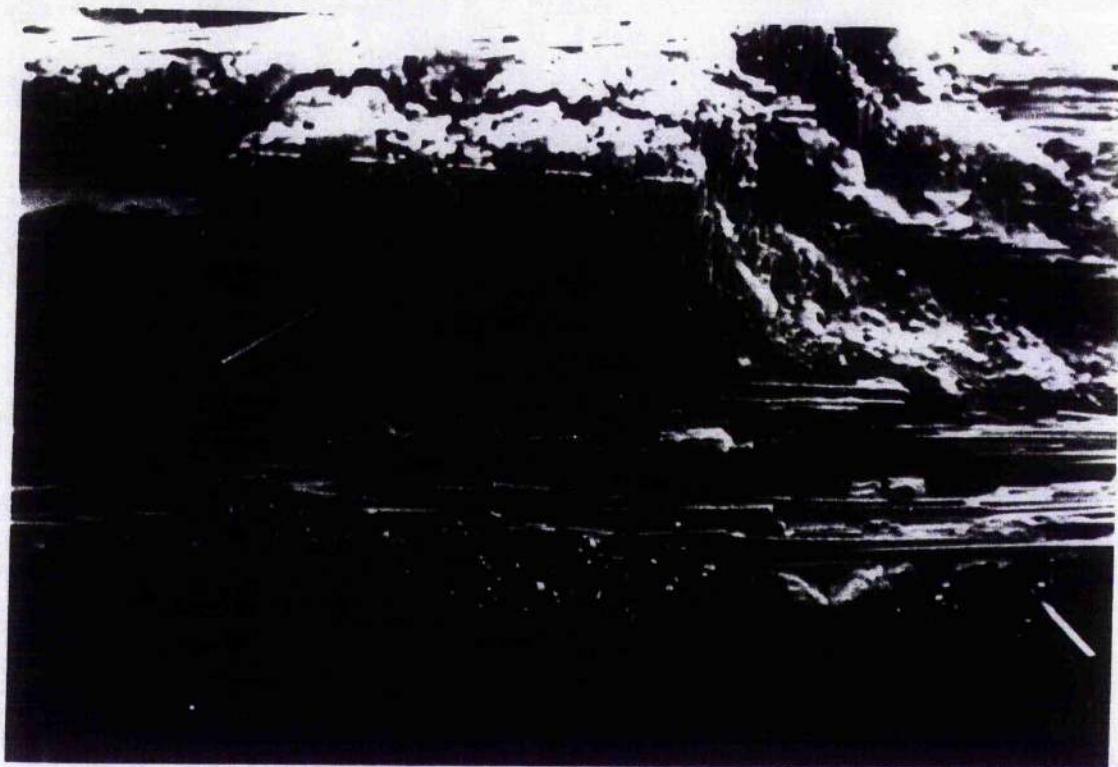


Figure 4.4.2 (e). Fractured surface of DLC thickened section. Magnification x 40

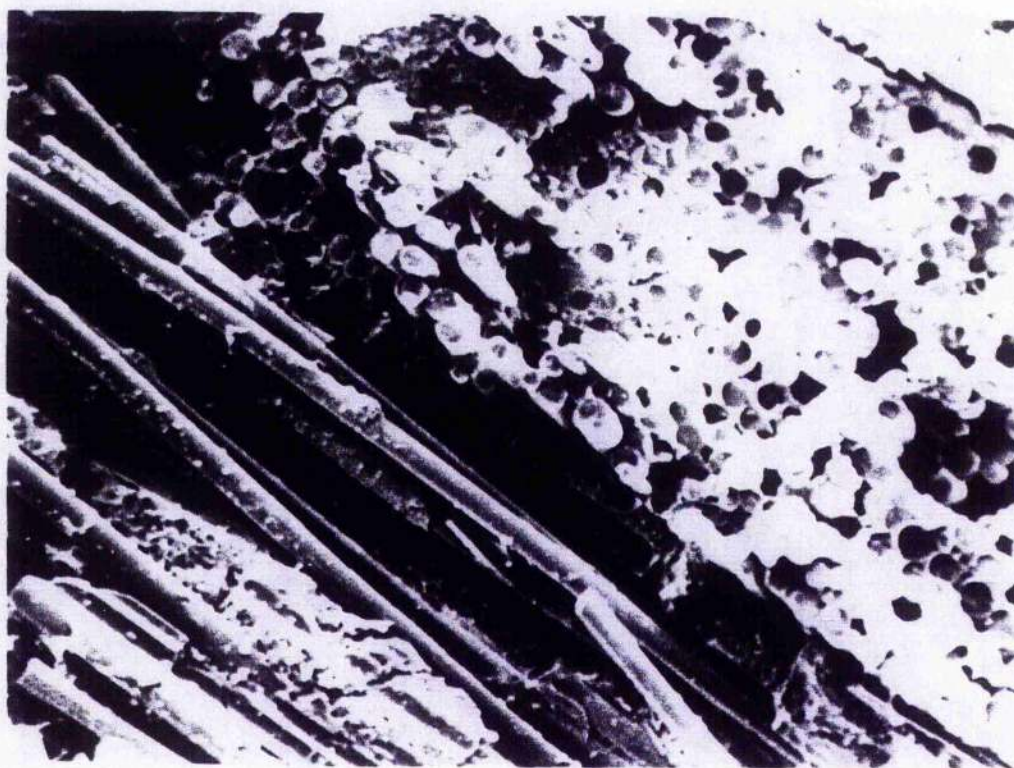


Figure 4.4.2 (f). Fibre pull-out occurring on DLC thicken section. Magnification x 160

4.4.3 T-Sections

Crack initiation and propagation in the polyester-polyester model material t-sections tested at room temperature is shown in figures 4.4.3 (a)-(b). Initiation of cracking on the model material t-section is shown in fig 4.4.3(a), which occurs at the central void region (confirmed by computational analysis in section 4.5). When subjected to increased stress, the cracks coalesce and deflect along the fibre bundles, eventually running the full length of the web.

This is more evident on the SiC/Al₂O₃ ceramic composite t-sections tested at room temperature, shown in figures 4.4.3(c)-(d). Fig 4.4.3(c) shows the initiation of cracking in the triaxial stress zone in the interior of the material, at the central void, and travelling down the web of the section. Increasing the stress results in the t-section failing by inter-laminar 'tearing', a mode I delamination, as shown in fig 4.4.3(d). Fractured surfaces of the material are shown in fig 4.4.3(e) and fig 4.4.3 (f), reveals fibre pullout occurs while the crack is being deflected through a fibre tow.



Figure 4.4.3 (a). Crack deflection and branching progressing through the model material t-section. Magnification x.35



Figure 4.4.3 (b). Crack opening on the model material t-section central region after being displaced to 7.5mm. Magnification x.35

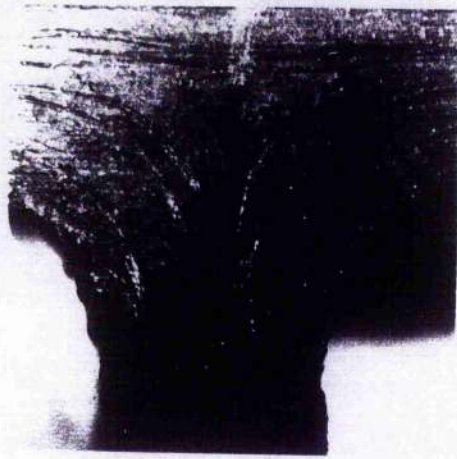


Figure 4.4.3 (c).Crack initiation on Dupont Lanxide T-Section, cycled to 1.5mm. Magnification x.1.5

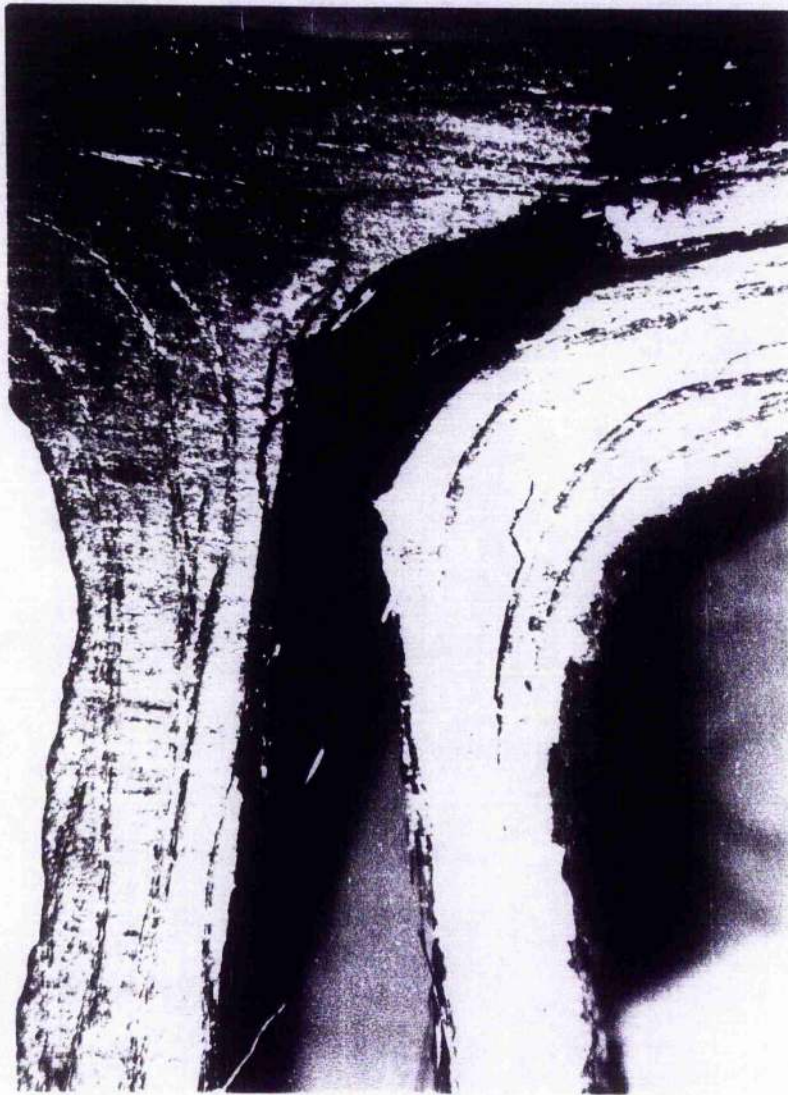


Figure 4.4.3 (d). Dupont Lanxide T-section taken to failure after being cycled to 6.4mm. Magnification x.15



Figure 4.4.3 (e).Fibre pullout occurring on Dupont Lanxide T-Section.

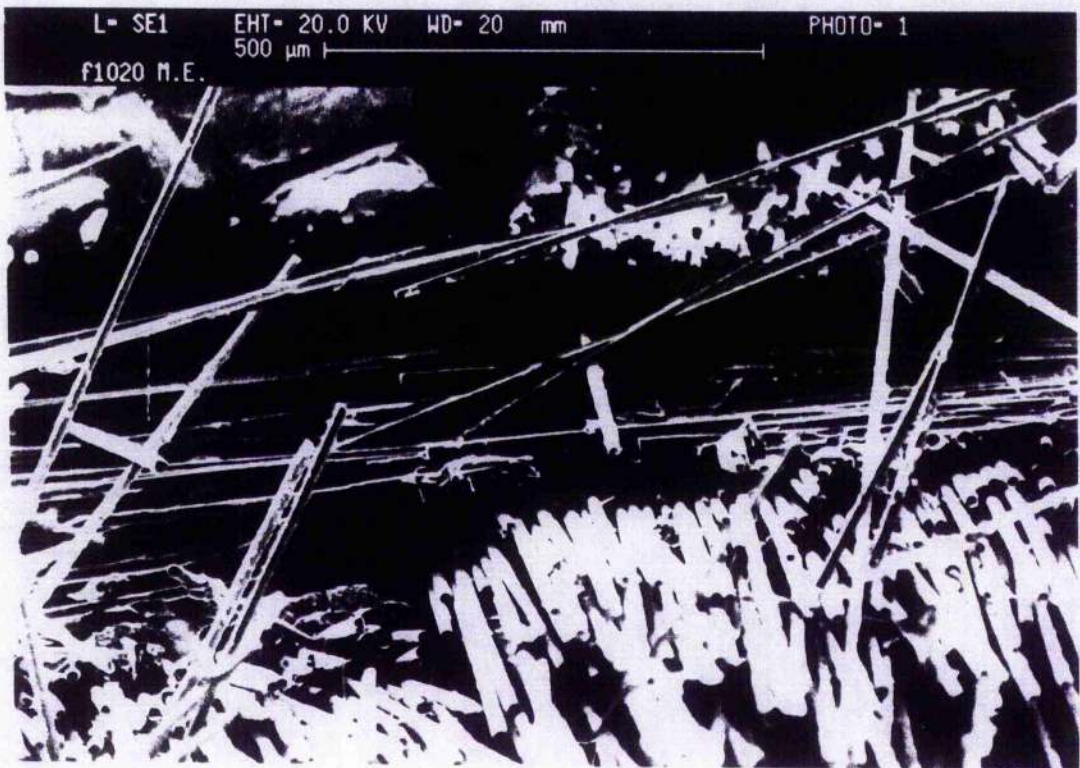


Figure 4.4.3 (f). Crack deflection through Dupont Lanxide T-Sections fibre tow.

4.4.4 Thermomechanical Tests

Crack deflection of $\frac{\delta}{w} = 0.75$ in a SiC/Al₂O₃ ceramic composite bend bar tested at 1273K is shown in fig 4.4.4(a). The crack progresses in similar fashion to the bend bar tested under ambient conditions. The fibre bundles deflect and arrest the primary crack, requiring an increase in energy to fail the material, as shown in fig 4.4.4(b), in which $\frac{\delta}{w} = 3.33$. Fractured surfaces of the material tested at 1273K are shown in figures 4.4.4(c)-(d). Fig 4.4.4(c) reveals fibre pullout, while closer examination of a fibre surface and interface, fig 4.4.4(d), shows slight oxidation of the fibre surface.

Amercom SiC/SiC composite bend bar, displaced to failure ($\frac{\delta}{w} = 2.39$) is shown, together with its fractured surfaces in fig 4.4.4(e) and fig 4.4.4(f). Little evidence of matrix infiltration of the fibre bundles is again found, which may account for the depletion in material properties at 1273K, in comparison to tests conducted under ambient conditions. This is likely caused by the individual fibres breaking earlier in the test causing a reduction in actual cross sectional area and apparent decrease in stiffness.

Crack deflection through a SiC/Al₂O₃ ceramic composite thickened (wedge) section at 1273K cycled prior to failure is shown in fig 4.4.4(g). The matrix microcracking, ultimate strength and composite modulus values have all been decreased, while the strain to failure was unaffected (compared to room temperature). Apparently temperature has an effect on degrading the fibre properties. Fractured surfaces of the material tested at 1273K are shown in figures 4.4.4(h)-(i), revealing fibre pullout and crack deflection through a fibre tow.

Crack initiation and propagation of the SiC/Al₂O₃ ceramic composite t-section at 1273K is shown in fig 4.4.4(j). Initiation of cracking on the ceramic t-section occurs at the central void region and run down the web. Increasing the stress results in the t-section failing in a

similar manner to the ambient testing by inter-laminar 'tearing'. The ultimate strength and composite modulus values have all been slightly decreased, while matrix microcracking the strain to failure was unaffected (compared to room temperature) Fractured surfaces of the material are shown in figures 4.4.4(k)-(l), revealing fibre pullout.

4.4.5 Discussion

Failure occurs in different ways. The onset of the non-linear deflection coincides with the formation of a matrix single crack, followed by multiple cracks and additional cracks caused by stress concentrations due to the fibre architecture and the various percentage of porosity. The SiC/Al₂O₃ ceramic composite bend bar failure initiated by cracking from a fibre tow on the tensile surface, the single crack been joined by other independently-produced equally spaced cracks the cracks continued to open and branch through the material, causing greater damage to the fibre bundles through which the main crack travels. The number of microcracks eventually increases until saturation occurs. There was little difference between the ambient and 1273K load-displacement plots for the SiC/Al₂O₃ ceramic composite bend bar. The Amercom SiC/SiC bend bar crack path through this material wasn't very clear. Due to the porosity of the material fracture would likely take place from pore to pore. Lack of matrix infiltration of the fibre bundles accounted for the depletion in material properties at 1273K.

The thickened section failed, not by the expected delamination near the corner but as a result of a crack which initiated at the corner and propagated across the specimen by fibre pullout. Finite element analysis conformed the presence of a stress concentration at the corner, but the effect is exacerbated by fibre depletion near the change in section in the real section. The effect of testing the thickened section at 1273K in an air environment proved to have an effect on reducing it's material properties caused by degrading the fibrous structure.

The t-sections failed by mode I delamination initiated in the triaxial stress zone in the interior of the material. Finite element analysis again confirming that this was the area of maximum principal stress. This was also the zone in which the design of the fibre architecture and infiltration by the matrix are most problematic. The effect of testing the t-section at 1273K in an air environment proved to have a slight effect on reducing its ultimate strength and composite modulus.

4.4.6 Conclusions

The nature of the tests performed allowed the material failure mechanisms to be observed by optical microscopy. This allowed the failure patterns to be observed step by step and their evolution for different load levels noted. This evolution can be simulated in Finite element modelling combining damage parameters to develop mechanistic models for the prediction of engineering materials response of ceramic composites. The emphasis on the design of the fibre architecture was critical for the sub-element geometries which must also take into account the requirement for better quality control during manufacture.



Figure 4.4.4 (a). Crack deflection of DLC ceramic bend bar cycled to 2mm at 1000C.
Magnification x 10

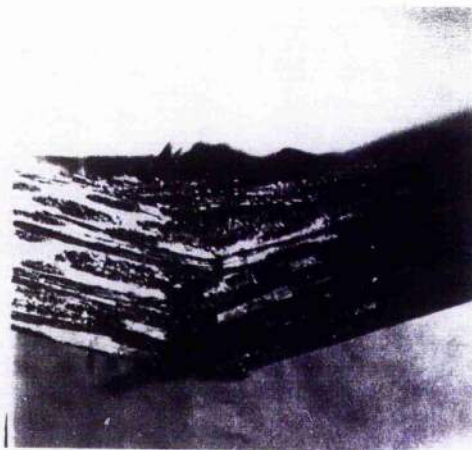


Figure 4.4.4 (b). DLC Ceramic bend bar taken to failure after being displaced to 10mm at 1000C.
Magnification x 10

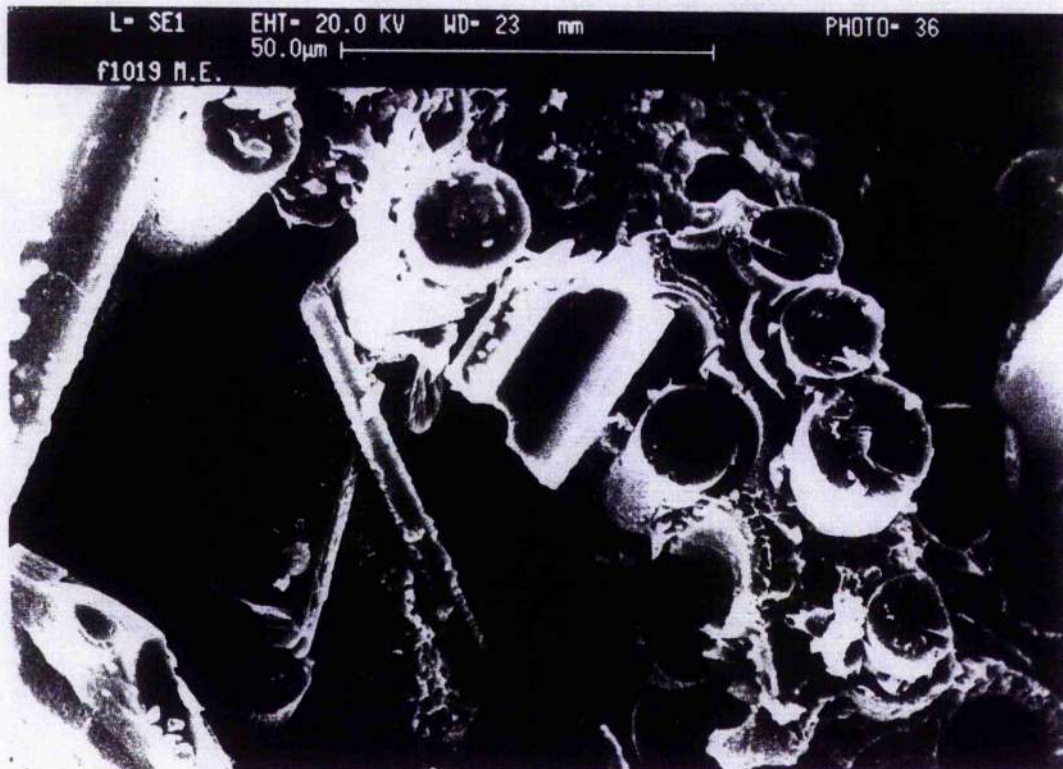


Figure 4.4.4 (c). Fractured surface of DLC ceramic bend bar at 1000C, showing fibre pullout.



Fig 4.4.4 (d). DLC bend bar showing oxidation of fibre surface and interface at 1000C.

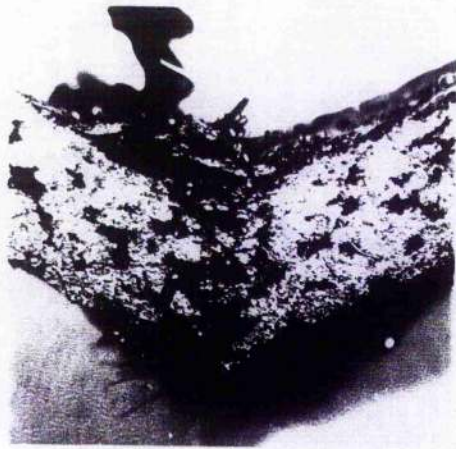


Figure 4.4.4 (e). Amercom bend bar taken to failure at 1000C.



Figure 4.4.4 (f). Amercom bend bar showing fibre pullout occurring at 1000C.



Figure 4.4.4 (g). DLC thickened section prior to failure, displaced to 2.25mm at 1000C. Magnification x 10



Figure 4.4.4 (h). Fractured surface of DLC ceramic thickened section at 1000C.

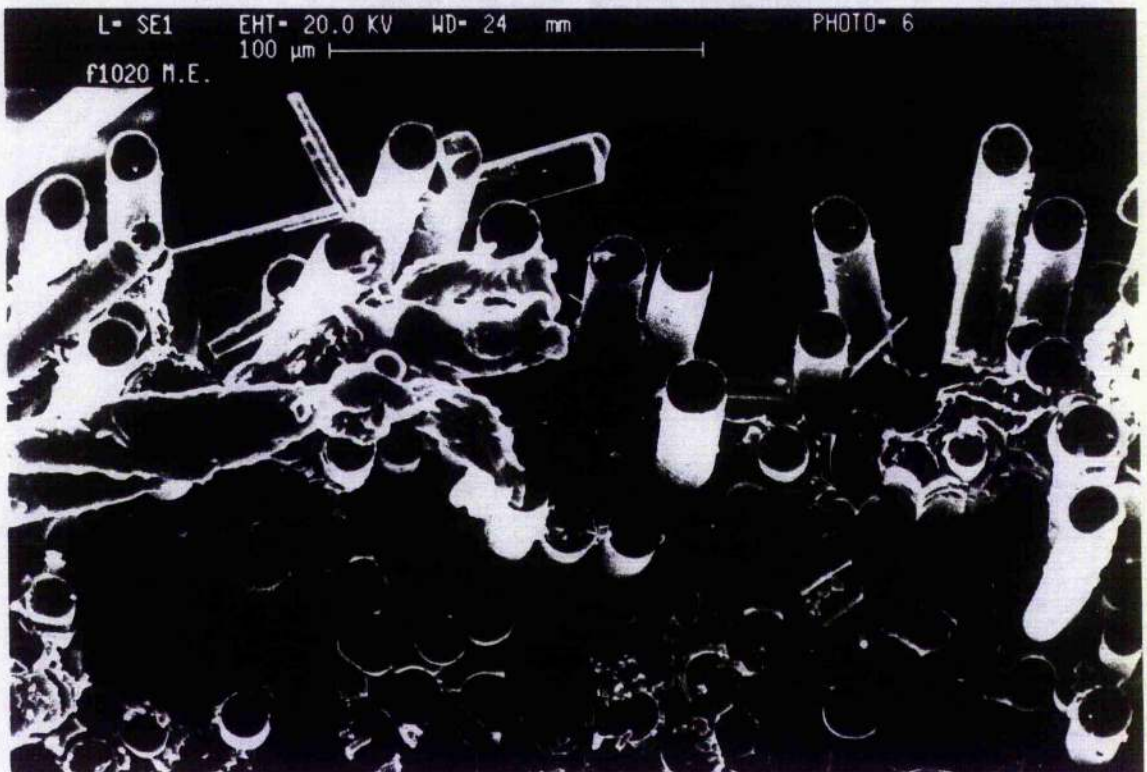


Figure 4.4.4 (i). Fibre pullout and crack deflection through fibre tow of DLC thickened section at 1000C.



Figure 4.4.4 (j). Crack deflection through DLC Ceramic T-Section displaced to 1.5mm at 1000C.
Magnification x 10



Figure 4.4.4 (k). Fractured surface of DLC ceramic T-Section at 1000C.



Figure 4.4.4 (l). DLC ceramic T-section showing fibre pullout occurring at 1000C.

4.5 Design System FE Observations of the Sub-elements

As a precursor to the stress analysis of the sub-elements, and to also exercise the finite element module developed in associated work by Hopper (1993), geometric solid modelling of the sub-elements was carried out using Catia. The analyses were carried out using the FE solver ABAQUS v 5.2. 1st order plane strain elements (4 noded quads) were used throughout. The material properties were initially linear/isotropic. For the 'thickened section' and 't beam' sub-elements architectural models were generated in Catia using the Ceramic Composites Design System function developed by Hopper as part of GUIDE (ref, GUIDE). The principal material directions were input to the linear/isotropic analyses of those sub-elements to produce output stress components referred to the principal material directions. The stress contour plots for the 'thickened section' and 'T beam' sub-elements should therefore be interpreted as follows

s11=in-plane direct stress

s22=inter-laminar direct stress

t12=inter-laminar shear

with the 1 and 2 directions as shown in figs 4.5.1-4.5.12

4.5.1 Analysis of Sub-elements

A simple but adequate benchmark of the conclusions in section 4.2, was to compare the experimental and computational linear elastic displacements for each of the sub-element geometries. Elastic isotropic properties for the polyester model material and the SiC/Al₂O₃ ceramic composite had been previously derived from the bend bars. Taking typical load values from the linear elastic portion of the experimental load-displacement graphs, the displacements obtained by the design systems FE analysis compared favourably with the

experimental displacements as shown in table 4.5.1. Deviations between the calculated and experimental displacements would be due to the dimensions of the sub-element geometries not being measured accurately enough or uncertainty in material properties. Some degree of confidence and reliance could therefore be placed on the computational stresses and strains.

Although the initiation of microcracking is generally related to the onset of non-linearity from the load-displacement plot, the magnitude and location of the microcracking stress and strains can be difficult to interpret experimentally for complex geometries. To verify, the conclusions of the experimental fractographic examinations, computational values were obtained for the inplane, interlaminar and shear stresses for both the polyester model material and the ceramic composite. The microcracking load as previously derived from the experimental graphs was used as a benchmark during adjustment of the material properties input to the analysis. Table 4.5.2 tabulates, for each sub-element, a nominal elastic modulus and the related microcracking stress and strain values σ_m and ϵ_m . The suffices 11 etc correspond to the stress notations in section 3.

The computed stress field for the bend bars is shown in fig 4.5.1(a)-4.5.1(b) for the polyester model material (MMBB) and the Dupont Lanxide ceramic composite (RSB) respectively. Only the inplane direct stress s_{11} are given, since the other stress components are small in comparison. This (inplane-direct) stress is the dominant stress, likely to initiate failure. The stress contour plots for the inplane stresses, for a linear elastic loading, show a maximum stress occurring along the the tensile surface at the mid-span, just above the tensile surface (fig 4.5(a)). The experimental and fractographic examinations support this, with crack initiation occurring at the mid-span tensile surface at a fibre tow as shown previously in figures 4.4.1(a)-(h).

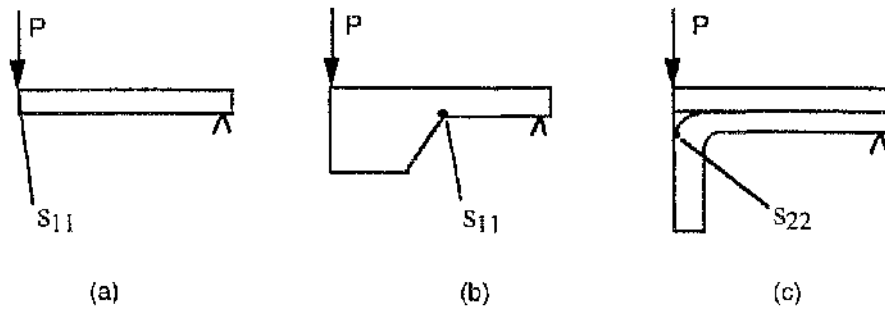


Fig 4.5 Maximum stress conditions (a) bend bars, (b) thickened sections, (c) t-sections

The computed results for the thickened (wedge) sections are shown in fig 4.5.1(c)-(d) for the model material (MMWS) and the ceramic composite (RSR) respectively. The two materials when subjected to a linear elastic load show the (inplane-direct) stress to be the dominant stress, likely to initiate failure. The maximum inplane stress is present at the fillet radius as shown in fig 4.5(b). The computed maximum stress is artificially high since it results from an over-estimated stress concentration factor at the fillet. This is due to the fillet radius not being accurately measured. However it does support the conclusions of the optical examination of the model material thickened section and the ceramic composite thickened section, which show crack initiation starting at the fillet radius, as shown in figures 4.4.2 (a)-(f).

The computed results for the t-sections are shown in fig 4.5.1(e)-(f) for the model material (MMTS) and the ceramic composite (RST) respectively. The two materials, when subjected to a linear elastic load, show the (interlaminar-direct) stress to be the dominant stress, likely to initiate failure. The maximum stress, for both materials, occurs at the mid-span at the lower point of the matrix region as shown in fig4.5(c). This supports the conclusions of the optical examination of the model material t-section and the ceramic composite t-section crack initiations and propagation as shown in figures 4.4.3(a)-(f).

4.5.2 Discussion

The inplane-direct stress was the dominant stress to initiate failure in the bend bar coupons. The finite element analysis stress contour plots for the inplane stresses showed a maximum stress occurring along the surface at the mid-span, just above the tensile surface. This was supported by experimental and fractographic examinations. The inplane-direct stress was the dominant stress likely to initiate failure in the thickened section coupons. This failed not by the expected delamination near the corner, but as a result of a crack (maximum inplane stress was present at the fillet radius) which initiated at the corner and propagated across the specimen by fibre pullout. This was supported by the optical examination of the thickened section systems showing crack initiation starting at the fillet radius. The interlaminar-direct (mode I delamination) stress was found to be the dominant stress to initiate failure for the t-section systems. The maximum stress occurred at the mid-span at the lower point of the matrix region (void region). This was also supported by the optical examination of t-section systems.

4.5.3 Conclusions

The finite element modelling of the coupons, produced via the Catia solid modeller and mesh generator, enhanced by Hopper 1993, has allowed the fibre orientations in composite systems to be specified. The subsequent analysis using Abaqus has proven to be a valuable tool in benchmarking the stress fields for simple composite coupons which was later able to predict with some confidence the response of more complex geometries. Work is still required however, to allow the finite element model to predict the spread of the damaged zone (ie include a mathematical model of microcracking). This may be done within the framework of continuum damage mechanics at some later stage.

	(Experimental)	Design System			
		Displacement (mm) δ	Inplane-direct stress (MPa) S_{11}	Interlaminar-direct stress (MPa) S_{22}	shear stress (MPa) τ_{12}
MMBB	0.822	0.833	14	-0.4	0.3
RSB	0.257	0.2496	127	-3	3
MMWS	1.422	1.278	53	1	3
RSR	0.193	0.208	305	3	-18
MMTS	2.147	1.98	-5	12	1
RST	0.157	0.126	-13	27	4

Table 4.5.1

	MMBB	RSB	RSB (1000C)	Amercom	Amercom (1000C)	MMWS	RSR	RSR (1000C)	MMTS	RST	RST (1000C)
Modulus GPa											
E	3.97	132	127	120	85	4	140	94	4	140	119
Stresses MPa											
s _{m11}	31	156	149	68	52	56	310*	238*	5.4	-13	-
s _{m22}	-0.9	-3.7	-3.5	-	-	1.06	-3.4	-2.6	13	30	29
s _{m12}	0.67	3.7	3.5	-	-	3.18	-20	-15	1.1	4	-
Strains											
e _{m11}	7.3E-3	1.03E-3	1.2E-3	6E-3	7E-4	0.013	2E-3	1.8E-3	-2.5E-3	-1.6E-4	-
e _{m22}	3.4E-3	-4.4E-4	-4.2E-4	-	-	5.2E-3	.8E-4	-6E-4	3.6E-3	2.1E-4	2.4E-4
e _{m12}	4E-3	.61E-4	.58E-4	-	-	2.3E-3	.32E-4	-2.5E-4	-9.2E-3	-0.7E-4	-
							* Artificially high values related to the SCF				

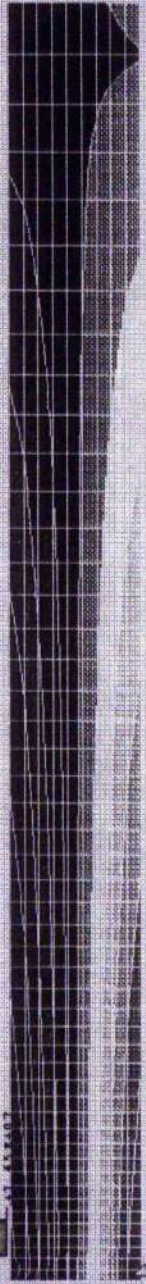
Table 4.5.2

1

```

#11 VALUE
-1.60E+07
-1.36E+07
-1.12E+07
-8.96E+06
-6.61E+06
-4.25E+06
-1.90E+06
44.42E+05
42.72E+06
45.14E+06
47.43E+06
49.84E+06
51.31E+07
53.45E+07

```



2

```

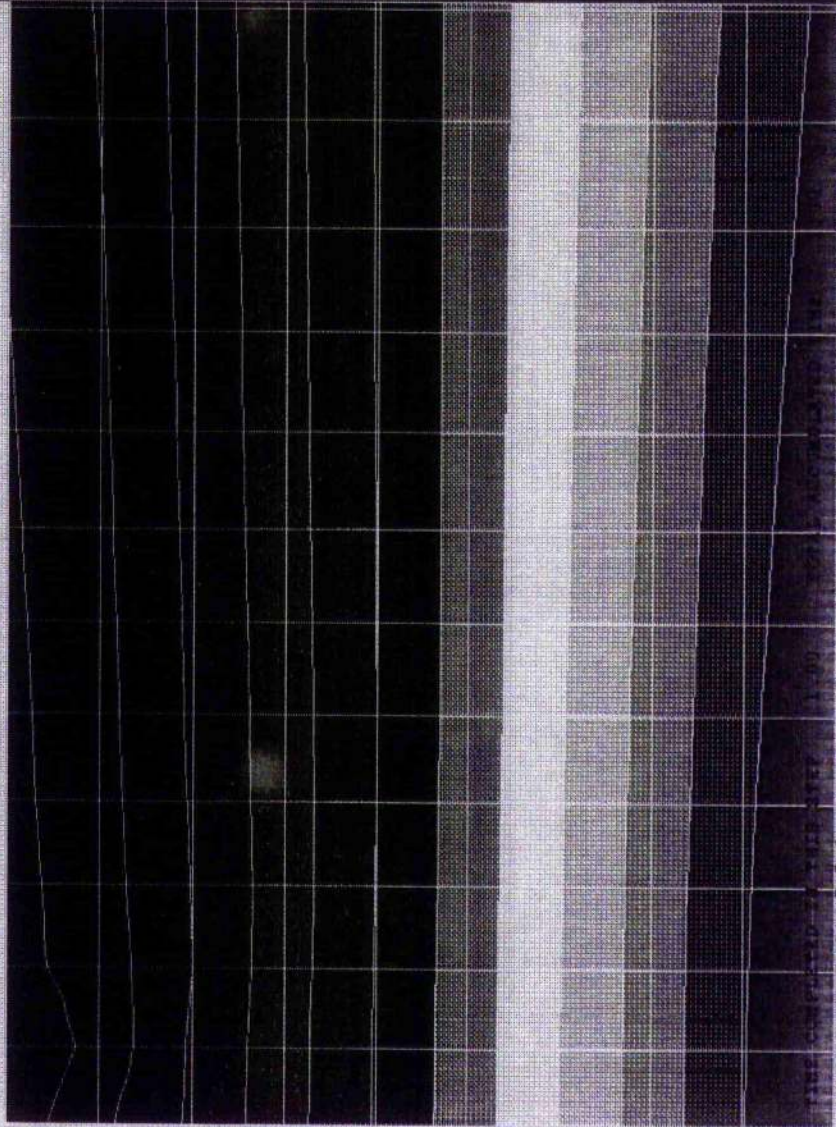
TIME COMPLETED IN THIS STEP 1.00 TOTAL ACCUMULATED TIME 1.00
ABAQUS VERSION: 5.2.1 DATE: 18-OCT-93 TIME: 13:07:33 STEP 1 INCREMENT 1

```

Fig 4.5.1 (a) Model Material Bend Bar (MMBB) In-plane Stress Condition

1

MIN	VALUE
1	1.39E+08
2	1.17E+08
3	9.83E+07
4	7.76E+07
5	5.69E+07
6	3.61E+07
7	1.54E+07
8	5.26E+06
9	3.59E+07
10	4.67E+07
11	66.74E+07
12	88.91E+07
13	11.08E+08
14	13.22E+08



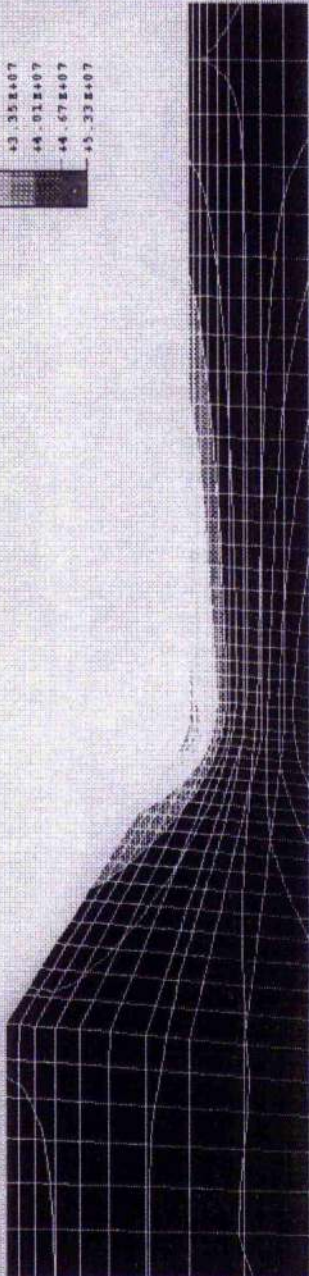
TIME CONSUMED IN THIS STEP: 1.00
ABAQUS VERSION: 5.2.1 DATE: 07 SEP-93 TIME: 14:41:32 STEP: 1 INCREMENT: 1

Fig 4.5.1 (b) Dupont Lanxide Bend Bar (RSB) In-plane Stress Condition

1

MIN	MAX
-3.23E+07	3.23E+07
-2.57E+07	2.57E+07
-1.91E+07	1.91E+07
-1.25E+07	1.25E+07
-5.95E+06	5.95E+06
-6.39E+05	6.39E+05
67.23E+06	67.23E+06
41.38E+07	41.38E+07
62.04E+07	62.04E+07
42.70E+07	42.70E+07
43.35E+07	43.35E+07
44.01E+07	44.01E+07
44.67E+07	44.67E+07
45.33E+07	45.33E+07

4



2

TIME COMPLETED IN THIS STEP 1.00 TOTAL ACCUMULATED TIME 1.00
 ABAQUS VERSION: 5.2.1 DATE: 18-OCT-93 TIME: 13:23:10 STEP 1 INCREMENT 1

Fig 4.5.1 (c) Model Material Thickened Section (MMWS) In-plane Stress Condition

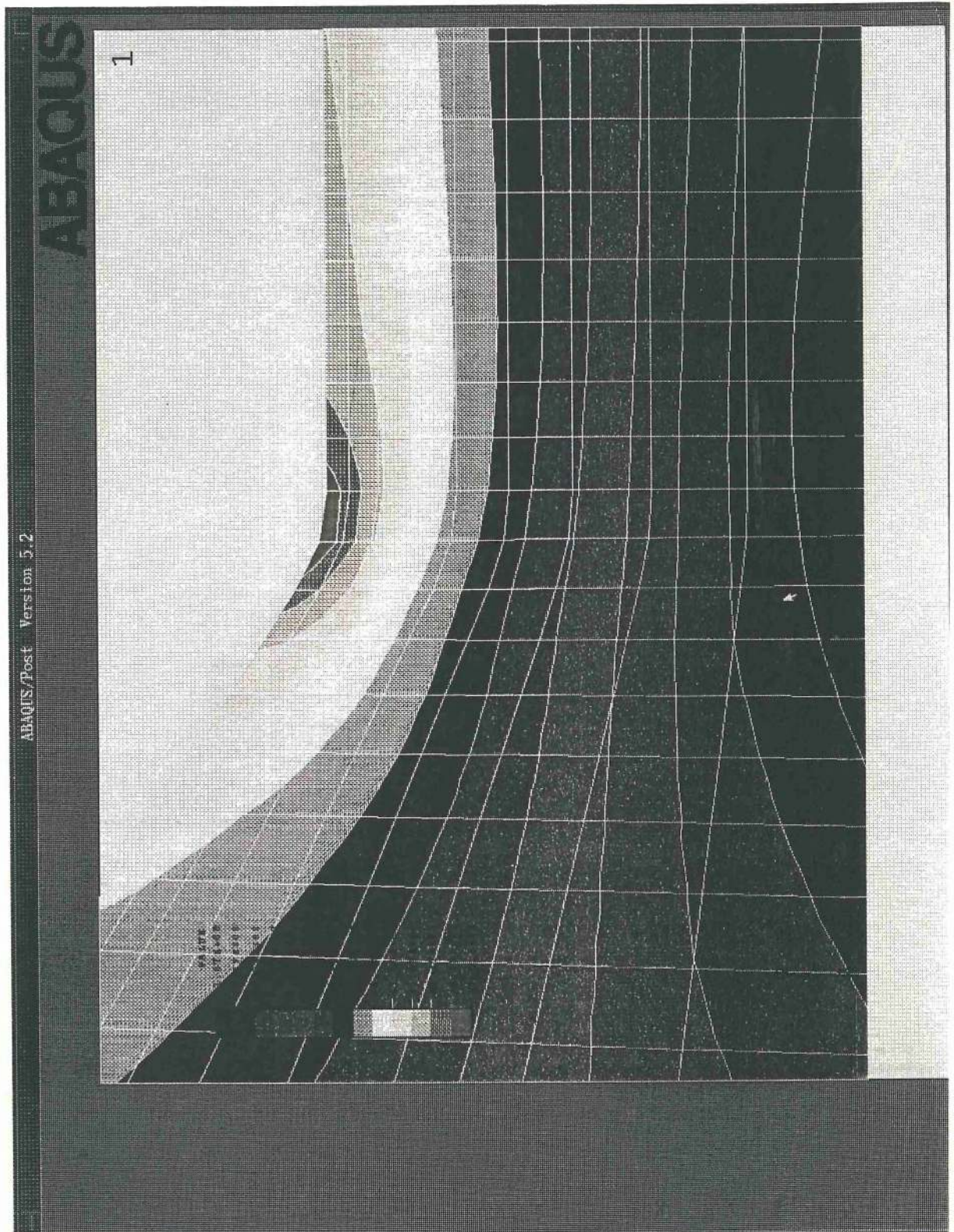


Fig 4.5.1 (d) Dupont Lanxide Thickened Section (RSR) In-plane Stress Condition

1

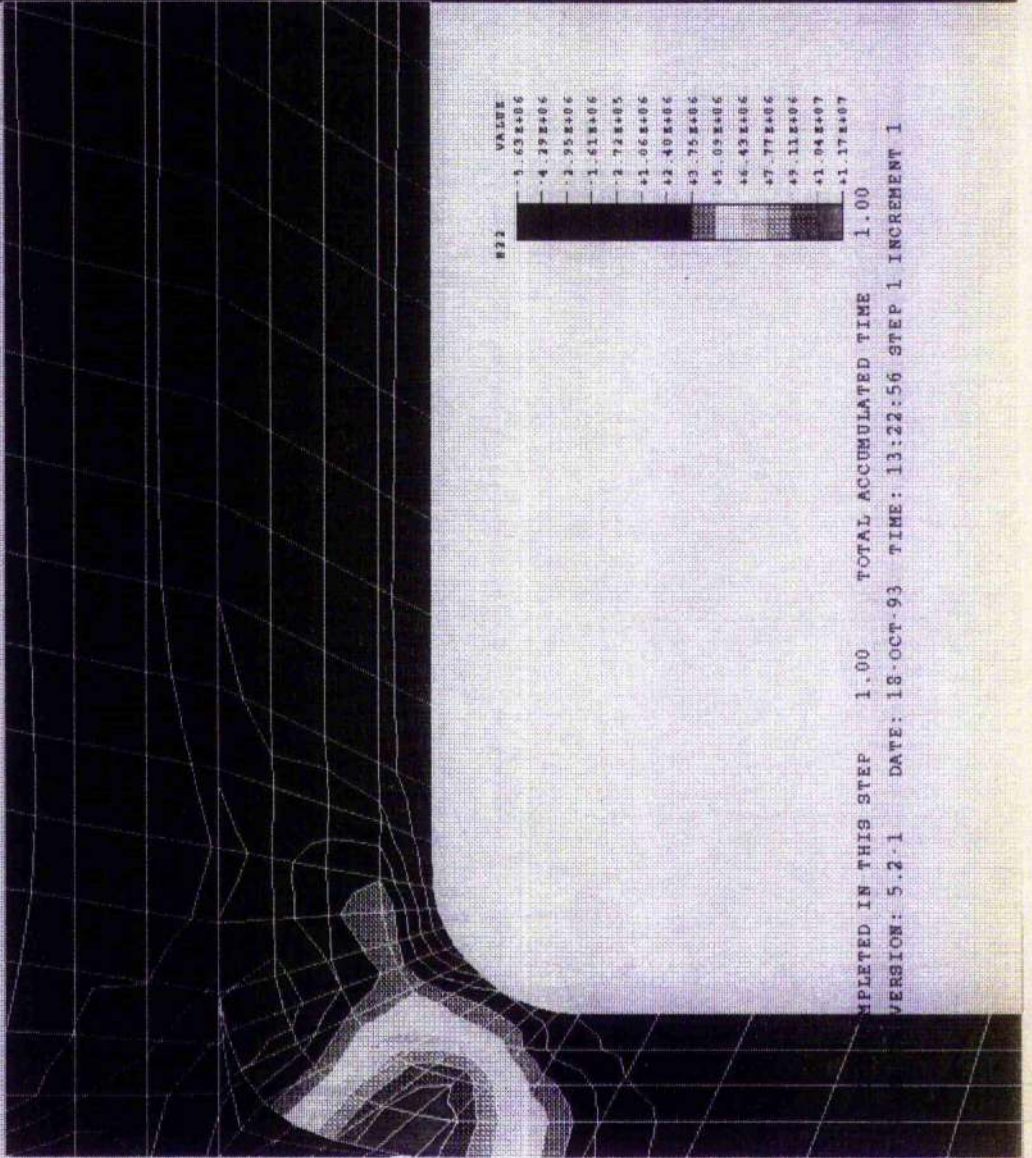


Fig 4.5.1 (e) Model Material T-Section (MMTS) Interlaminar Stress Condition

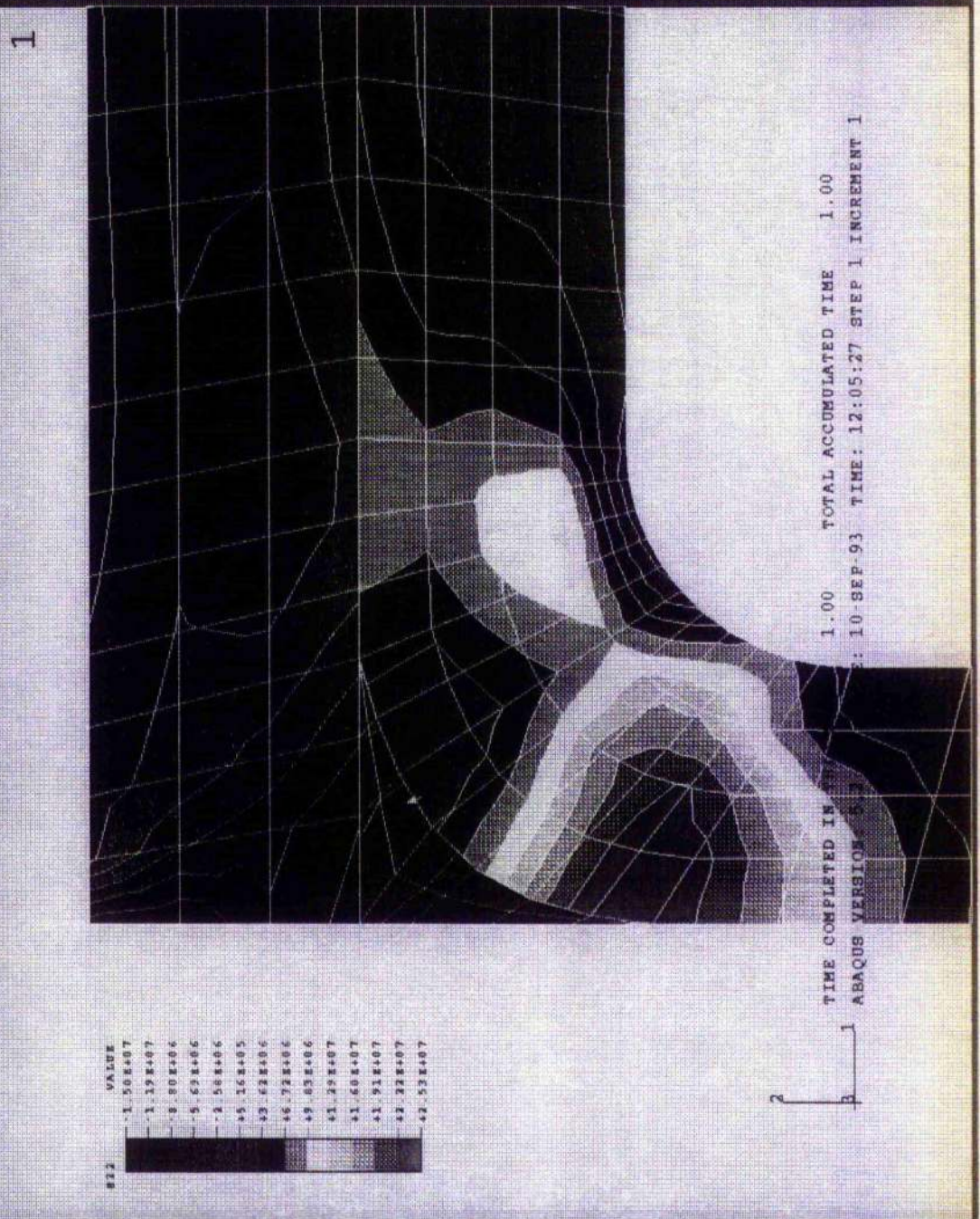


Fig 4.5.1 (f) Dupont Lanxide T-Section (RST) Interlaminar Stress Condition

4.6 Residual Strain Behaviour & Energy Release Rates

The mechanical behaviour of the cyclic load-displacement curves for geometric sub-elements tested recorded the reversible behaviour (δ_{rei}), which is the response of the material to a loading, and observed the residual behaviour (δ_r) resulting from mechanical damage. The variation of these strains help provide a good indication of the underlying damage (Sorensen, Talreja, (1993); Inghels, Lamon, (1991)). Also for each of the cyclic tests conducted the value of the strain energy release rate (G), associated with delamination growth, was determined directly by measuring the area enclosed by the load-deflection curves (hysteresis loops). The residual displacements and energy release rates were normalised by their microcracking displacements (δ_m) and microcracking release rate (G_m) respectively and plotted as a function of displacement (δ) which had also been normalised by the materials microcracking displacement (δ_m). Measuring of the crack extensions (a) for each of the geometric sub-elements was however hampered, and the analysis is incomplete.

4.6.1 Bend Bars

Figure 4.6.1(a) shows the response of the normalised residual-displacement behaviour for the SiC/Al₂O₃ ceramic composite and polyester model material composite bend bars. The model material (MMBB) composite and SiC/Al₂O₃ (RSB) composite tested at room temperature showed a similar response. The permanent strain increased linearly until the specimen fractured. The SiC/Al₂O₃ composite tested at 1273K showed the residual strain response to be non-linear, damage caused by permanent strain occurring at a greater rate, as shown by the gradient of the curve, later in the deformation.

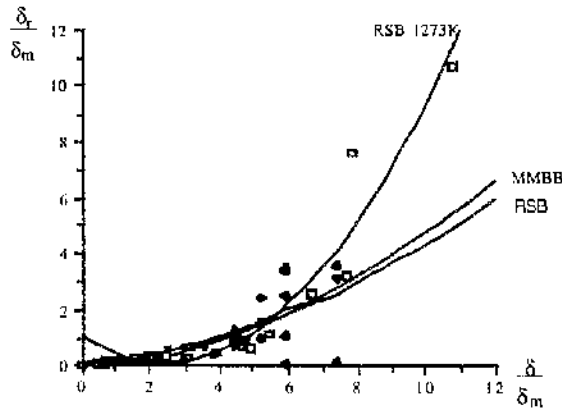


Fig 4.6.1 (a) Bend bars non-dimensionalised residual behaviour

Figure 4.6.1 (b) shows the response of the normalised energy release rate-displacement behaviour for the bend bars. The strain energy release rate increases with increased crack extension. The cracks being arrested and deflected by the fibre bundles require extra energy to propagate the crack further. The slopes display a constant linear increase in energy dissipation corresponding to the decay in the initial modulus until each of the graphs reaches an upper limit. Upon further cycling a decreasing amount of energy dissipation will occur. The increase in energy dissipated per cycle was observed with increase in maximum cyclic stress. Large hysteresis loops were evident at the end of the 'hot' test on SiC/Al₂O₃ (RSB) composite indicating a disproportionately large amount of energy dissipated in the material. The high energy dissipation per cycle corresponds with the material exhibiting a rapid initial modulus decay.

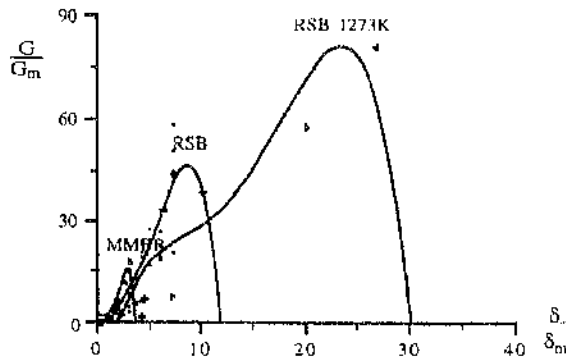


Fig 4.6.1 (b) Bend bars non-dimensionalised energy release rates behaviour

Tables 4.6.1, 4.6.2 and 4.6.7 tabulate the reversible/residual strain behaviour, energy release rates, and crack extensions (were obtained) for the bend bars tested at room and 1273K.

4.6.2 Thickened Sections

Figure 4.6.2(a) shows the response of the normalised residual-displacement behaviour for the SiC/Al₂O₃ ceramic composite and polyester model material composite thickened (wedge) sections. No direct comparison can be made between the model material (MMWS) composite and SiC/Al₂O₃ (RSR) composite tested at room temperature. The rate of increase of permanent strain is greater in the polyester composite in comparison to the more brittle Dupont Lanxide thickened sections. The response of the SiC/Al₂O₃ at room temperature is linear. At 1273K it is stepper. The effect of temperature therefore is to increase the residual strain on the thickened section.

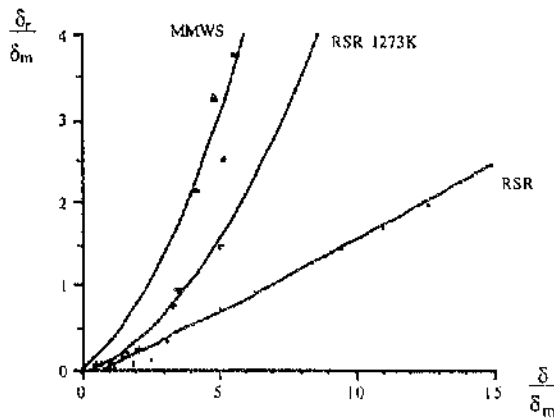


Fig 4.6.2 a) Thickened sections non-dimensionalised residual behaviour

Figure 4.6.2 (b) shows the response of the normalised energy release rate-displacement behaviour for the thickened sections. The strain energy release rate increases with increased crack extension non linearly (parabolically) reaching a peak and then decreasing with each continued cycles. The SiC/Al₂O₃ thickened composite tested at room temperature and 1273K showed no change in the amount of energy dissipated. A larger amount of energy was dissipated per cycle for the ceramic composites compared to the polyester model material.

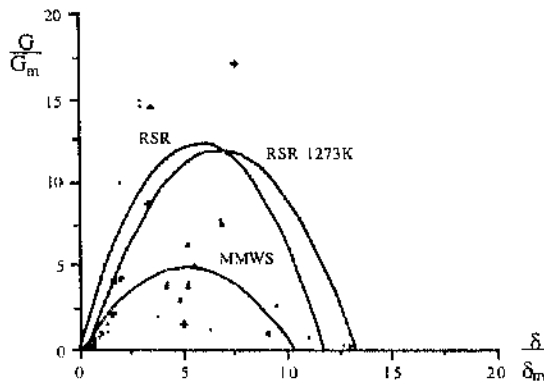


Fig 4.6.2 (b) Thickened sections non-dimensionalised energy release rates behaviour

Tables 4.6.3, 4.6.4 and 4.6.8 tabulate the reversible/residual strain behaviour, energy release rates, and crack extensions for the thickened sections tested at room and 1273K.

4.6.3 T-Sections

Figure 4.6.3 (a) shows the response of the normalised residual-displacement behaviour for the SiC/Al₂O₃ ceramic composite and polyester model material composite t-sections.

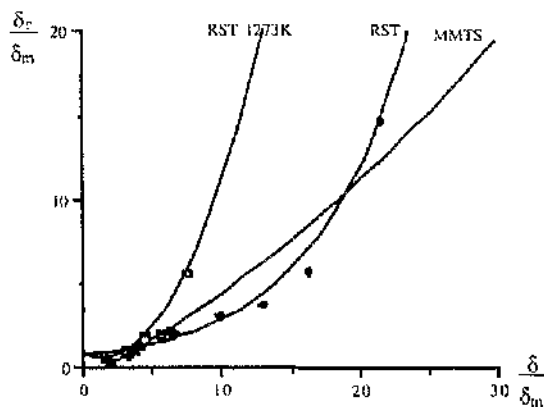


Fig 4.6.3 (a) T-sections non-dimensionalised residual behaviour

The model material (MMTS) composite and SiC/Al₂O₃ (RST) composite tested at room temperature show a similar response. For the MMTS the permanent strain increased linearly until the specimen fractured. The SiC/Al₂O₃ t-section composite tested at 1273K showed the residual strain to increase more rapidly. The damage caused by permanent strain is therefore increased by temperature.

Figure 4.6.3 (b) shows the response of the normalised energy release rate-displacement behaviour for the t-sections. The strain energy release rate for the SiC/Al₂O₃ t-section composites increases with increased crack extension non linearly (parabolically) reaching a peak and then decreasing with each continued cycles. The model material t-section

showed a rapid but linear energy release rate. The SiC/Al₂O₃ t-section composites tested at room temperature and 1273K showed the amount of energy dissipated in the 'hot' test to be reduced. A larger amount of energy was dissipated per cycle for the ceramic composites compared to the polyester model material.

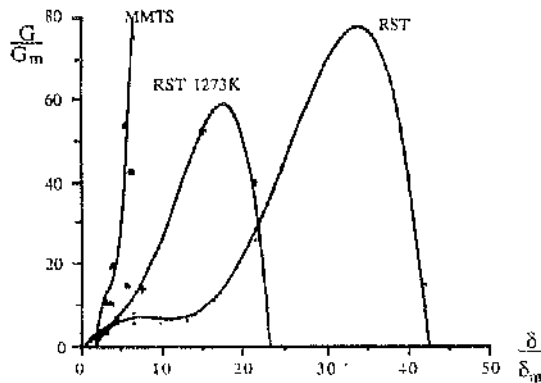


Fig 4.6.3 (b) T-sections non-dimensionalised energy release rates behaviour

Tables 4.6.5, 4.6.6 and 4.6.9 tabulate the reversible/residual strain behaviour, energy release rates, and crack extensions (were obtained) for the thickened sections tested at room and 1273K.

4.6.4 Discussion

The SiC/Al₂O₃ ceramic composite and polyester model material composite normalised residual strain curves were shown to be generally similar for the bend bars and the t-sections sub-elements. This wasn't shown by the thickened sections, the increase of the ceramic composites normalised residual strain rate being gradual compared to the model material. Temperature had the effect of increasing the rate of permanent strain in all of the geometric sub-elements. There was found to a greater amount of energy dissipated (normalised) in the ceramic composite materials, the exception shown for the model

material t-section which compared favourably with the ceramic specimen. Temperature had a different effect on the energy release rates for each of the three sub-elements. For the ceramic composite bend bars large hysteresis loops were evident. This gave a disproportionately large amount of energy dissipated in the material.. The ceramic composite thickened sections were unaffected by the temperature at 1273K while the ceramic composite t-sections had a reduced amount of energy dissipated by the material tested at 1273K.

4.6.5 Conclusions

Temperature had an effect of increasing the rate of increase of permanent strain in all of the geometric sub-elements, with these high residual strains causing a dramatic increase in the work of fracture. Temperature was also significant in increasing the energy dissipated in the ceramic composite bend bars, reducing the energy dissipated in the t-sections and being insignificant in the thickened sections. A high energy dissipation per cycle corresponded with the material exhibiting a rapid initial modulus decay. Measurements of the crack extensions were incomplete and are therefore not reported.

Test No	No Cycles	δ (mm)		δ_r	G (mJ)	a_c (mm)
		Total	δ_{rel}			
MMBB1	1	6.5	-	-		NA
MMBB2	1	9.05	-	-		NA
MMBB3	1	0.988	0.833	0.155	1.78	
	2	1.494	1.311	0.183	3.47	
	3	1.74	1.514	0.226	4.02	NA
MMBB4	1	0.991	0.78	0.211	1.52	
	2	1.5	1.241	0.259	2.84	
	3	1.75	1.459	0.291	3.44	
	4	1.995	1.666	0.329	4.45	
	5	2.494	2.124	0.370	7.2	NA
MMBB5	1	1.517	1.287	0.23	3.37	
	2	3.0	2.557	0.443	16.05	
	3	4.473	3.706	0.767	44.03	1.574
MMBB6	1	1.964	1.644	0.32	6.05	
	2	3.941	3.332	0.609	39.7	
	3	5.977	4.678	1.299	107.3	1.76
MMBB7	1	2.441	2.122	0.319	13.31	
	2	4.949	4.111	0.838	57.57	
	3	7.487	5.892	1.595	161.57	1.97

Table 4.6.1 Model Material Bend Bar (MMBB)

Test No	No <u>Cycles</u>	δ (mm)		δ_r	G <u>(mJ)</u>	a_c <u>(mm)</u>
		<u>Total</u>	δ_{rel}			
RSB001	1	2.5				
	2	2.756				1.773
RSB002	1	1	0.955	0.045	5	
	2	1.5	1.225	0.275	145	
	3	1.75	1.424	0.326	165	0.74
RSB003	1	1	0.927	0.073	44	
	2	1.5	1.233	0.267	136	
	3	1.75	1.233	0.517	149	
	4	2	1.166	0.834	135	1.857
RSB004	1	1	0.92	0.08	22	
	2	1.5	1.216	0.284	138	
	3	1.75	1.334	0.416	102	
	4	2	1.179	0.821	164	
	5	2.5	1.314	1.186	124	1.642
RSB005	1	0.4	0.364	0.036	6	
	2	0.8	0.74	0.06	23	
	3	1.2	1.097	0.103	40	
	4	1.6	1.353	0.246	120	
	5	2	1.638	0.3	112	0.796
RSB006	1	0.5	0.467	0.033	9	
	2	1	0.932	0.068	50	
	3	1.5	1.288	0.212	124	
	4	2	1.666	0.334	128	
	5	2.5	1.375	1.125	349	
	6	3.5	0.96	2.54	-	2.266
RSB007	1	0.5	0.452	0.048	12	
	2	1	0.919	0.081	28	
	3	1.5	1.258	0.242	117	
	4	2	1.642	0.358	118	
	5	2.5	1.433	1.067	299	1.642
RSB008	1	1.3	1.172	0.128	81	0.414
RSB009	Not Tested					
Am001	1	0.502	0.445	0.057	24	
	2	1.004	0.838	0.166	26	
	3	2.059	1.542	0.517	88	
Am002	1	9.797			637	

Table 4.6.2 Dupont Lanxide Bend Bars (RSB)/Amercom(Am)

Test No	No <u>Cycles</u>	δ (mm)		δ_r	G <u>(mJ)</u>	a_c <u>(mm)</u>
		<u>Total</u>	δ_{rel}			
MMWS1	1	7.503	-	-	751	0.764
MMWS2	1	9.822	-	-	910	0.99
MMWS3	1	8.011	4.254	3.757	601	0.8
MMWS4	1	7.503	4.98	2.523	460	0.97
MMWS5	1	7.01	3.756	3.254	362	
MMWS6	1	6.005	3.855	2.15	456	0.83

Table 4.6.3 Model Material Wedge Section (MMWS)

Test No	No <u>Cycles</u>	δ (mm)		δ_r	G <u>(mJ)</u>	a_c <u>(mm)</u>
		<u>Total</u>	δ_{rel}			
RSR001	1	1.003	0.094	0.909	205	
	2	1.5	0.046	1.454	17	
	3	1.75	0.034	1.716	5	
	4	1.996	0.008	1.988	2	Failed
RSR002	1	0.148	0.119	0.029	5	
	2	0.3	0.233	0.077	64	
	3	0.472	0.094	0.378	97	0.796
RSR003	1	0.101	0.091	0.01	2	
	2	0.201	0.181	0.02	7	
	3	0.3	0.234	0.066	33	
	4	0.4	0.291	0.109	149	
	5	0.5	0.179	0.32	-	0.8
RSR004	1	0.203	0.177	0.026	10	
	2	0.465	0.099	0.366	95	
	3	0.6	0.067	0.533	13	
	4	0.8	0.063	0.737	10	
	5	1	0.076	0.924	8	x

Table 4.6.4 Dupont Lanxide Wedge Section (RSR)

Test No	No Cycles	δ (mm)		δ_r	G (mJ)	a_c (mm)
		Total	δ_{rel}			
MMTS1	1	10.73	-	-	374	NA
MMTS2	1	12.529	-	-	526	NA
MMTS3	1	12.08	7.8	4.209	297	NA
MMTS4*	1	10.8	6.9	3.9	102	NA
MMTS5 x	1	8.03	5.762	2.238	137	NA
MMTS6* x	1	7.5	5.615	1.885	71	NA
MMTS7 x	1	6	4.567	1.433	76	NA
MMTS8 x	1	4	3.595	0.405	24	NA

Table 4.6.5 Model Material T-Section (MMTS)

Test No	No Cycles	δ (mm)		δ_r	G (J)	a_c (mm)
		Total	δ_{rel}			
RST001	1	1	0.699	0.301	98	NA
	2	1.503	1.033	0.47	77	
	3	3.247	0.993	2.254	313	
	4	6.4	-	-	178	
RST002	1	0.5	0.377	0.123	40	NA
	2	0.997	0.696	0.301	68	
	3	1.502	1.033	0.469	76	
RST003	1	0.497	0.371	0.126	39	NA
	2	0.988	0.664	0.324	69	
	3	1.5	1.032	0.468	67	
	4	1.996	1.421	0.575	73	
	5	2.5	1.628	0.872	135	

Table 4.6.6 Dupont Lanxide T-Sections (RST)

Test No	No Cycles	δ (mm)		δ_r	G (mJ)	a_c (mm)
		Total	δ_{rel}			
RSB010	1	6.816	-	-	688	Failed
RSB011	1	9.00	-	-	969	Failed
RSB012	Not Recieved					
RSB013	1	1.27	1.132	0.138	71	
RSB014	Not Recieved					
RSB015	1	1.497	1.295	0.202	21	
	2	2.468	1.441	1.027	92	
	3	3.446	0	3.446	459	2.67
RSB016	1	0.494	0.405	0.089	13.4	
	2	1.497	1.198	0.299	82	
	3	2.524	0.065	2.459	523	2.43
RSB017	1	0.79	0.689	0.101	30	
	2	1.581	1.378	0.203	84	
	3	2.142	1.326	0.816	396	1.62
RSB018	1	1.004	0.916	0.088		
	2	1.754	1.394	0.36		1.6
RSB019	Not Tested					
RSB020	Not Tested					
Am003	1	7.17			807	

Table 4.6.7 Dupont Lanxide Bend Bar (RSB)/Amercom(Am) at 1000C

Test No	No Cycles	δ (mm)		δ_r	G (mJ)	a_c (mm)
		Total	δ_{rel}			
RSR005	1	2.255	-	-	223	NA
RSR006	1	0.15	0.09	0.06	2	NA
	2	0.302	0.209	0.09	13	
	3	0.451	0.298	0.153	27	
RSR007	1	0.497	0.302	0.195	54	NA
	2	1.035	0.085	0.95	188	
	3	1.503	0.021	1.482	20	
RSR008	1	0.202	0.147	0.055	7	NA
	2	0.602	0.363	0.239	56	
	3	0.991	0.229	0.762	113	
RSR009	} Not Tested					
RSR010	}					

Table 4.6.8 Dupont Lanxide Wedge Section (RSR) at 1000C

Test No	No Cycles	δ (mm)		δ_r	G (mJ)	a_c (mm)
		Total	δ_{rel}			
RST004	1	4.934	-	-	887	NA
RST005	1	7	-	-	678	NA
RST006	1	0.497	0.344	0.153	31	NA
	2	1	0.674	0.326	56	
	3	1.487	0.873	0.614	104	
RST007	1	0.503	0.298	0.205	24	NA
	2	1.496	0.946	0.55	116	
	3	2.467	0.628	1.839	239	
RST008	}					
RST009	} All Not Tested					
RST010	}					

Table 4.6.9 Dupont Lanxide T-Section (RST) at 1000C

5.0 Final Conclusions

Optical heating was found to be a practical method for generating high temperature rates in laboratory testpieces. Tests on ceramic composite specimens, subjected to thermal transients using an optical furnace, have shown that the mechanical performance of these materials is degraded by temperature but not by the amount initially expected. Nevertheless, such materials are expensive to produce and test. The utility of a low cost polyester-polyester composite system to behave as a model material and simulate the Dupont Lanxide SiC/Al₂O₃ ceramic composite system has been demonstrated, at least for ambient conditions. Any discrepancies between some of the model material and ceramic composite normalised curves can be attributed to the difficulty of assessing the exact point where microcracking commenced. The inability of the model material to simulate Amercom SiC/SiC was attributed to the lack of penetration of the matrix into the fibres.

An approximate modulus, obtained from the bend bar, was used for the thickened section and the t-section since calculating an *exact* elastic modulus was problematic. Although the materials database is incomplete, knowledge of these complex geometries was sufficient to allow their performance to be established and compared. Measuring the crack length (a_c) accurately for these geometries was also prone to error and in many cases, the data tables simply omitted these values. The Amercom 3-D braided SiC/SiC composite tests were halted due to the poor quality and porosity of the material. Due to the small quantity of each batch of material tested, a statistical approach (Weibulls modulus) wasn't appropriate.

Failure of the bend bars commenced with the initiation of cracking from a fibre tow on the tensile surface, the single crack progressing through the material to be joined by other independently produced cracks. During subsequent increases in displacement the cracks continued to open and branch through the material, causing greater damage to the fibre

bundles through which the main crack travelled. The number of microcracks eventually increased until saturation, and no further microcracking occurred. The Amercom bend bars failure mapping was very clear though, due to the porosity of the material, fracture would likely take place from pore to pore. The pores would normally play an important part in arresting the crack, therefore increasing the amount of work required to fracture the material further, but there was little evidence of this occurring. Crack initiation and propagation of the thickened sections (wedge) occurred where the change in the geometric section created a high stress concentration. This was found to be near the reentrant corner on the tension side. As loading continued the crack passed through the material to the next fibre bundle, the crack continuing to open and branch causing greater damage to the fibre bundles through which the main crack had already travelled. The crack was deflected by the fibre bundles, failure finally happening with fibre pullout. Crack initiation and propagation in the t-sections occurred at the central highly voided region. When subjected to increased stress, the cracks coalesce and deflect along the fibre bundles, eventually running the full length of the web. Increasing the stress results in the t-section failing by inter-laminar 'tearing', a mode I delamination,

Testing the SiC/Al₂O₃ composite bend bars at 1273K resulted in no significant change in the state of the elastic modulus (E_1) and the materials strength (σ_u) and the onset of microcracking (σ_m). Discrepancies between the room and elevated temperatures may be attributed to scatter associated with the material. The high temperature degradation and oxidation of the surface layer was more predominant in the SiC/Al₂O₃ thickened section (wedge) and to a lesser extent the t-section composite specimens. Both geometries show a reduction in stiffness, the wedge performing poorly with a reduction in all of its other material properties. The wedge system failure mechanism is accelerated by a combination of high temperature degradation associated with an increase in fibre pullout. The t-section showed a slight reduction in its stiffness at 1273K which again was attributed to scatter associated with the material. Temperature had the effect of increasing the rate of increase

of permanent strain in all of the geometric sub-elements, with these high residual strains causing an increase in the work of fracture. Temperature was also significant in increasing the energy dissipated in the ceramic composite bend bars, reducing the energy dissipated in the t-sections and being insignificant in the thickened sections. A high energy dissipation per cycle corresponded with the material exhibiting a rapid initial modulus decay.

The progressive reduction in modulus with deformation was measured using the Continuum damage mechanics (CDM) approach, by analysing the loading history of cyclically loaded sub-elements. Unique damage-displacement relationships for model and ceramic composites subjected to flexure loading conditions were obtained and will provide a valuable tool in engineering design. The nature of the tests performed allowed the material failure mechanisms to be observed (after testing) by optical microscopy. Failure patterns were observed step by step with their evolution for different load levels.

The finite element modelling of the coupons, produced via the Catia solid modeller and mesh generator allowed the fibre orientations in composite systems to be specified. The modelling proved to be a valuable tool in benchmarking the stress fields for simple composite coupons which was later able to predict with some confidence the response of more complex geometries. Work is still required however, to allow the finite element model to predict the spread of the damaged zone (ie include a mathematical model of microcracking). This may be done within the framework of continuum damage mechanics at some later stage.

6.0 References

- ASTM C1161 (1990) American Standards Testing Materials (Brittle & Monolithic Ceramics)
- Baratta F.J (1984) Requirements For Flexure Testing Of Brittle Materials; ASTM STP844 pp194-22
- Borossa.(1989) Developments And Applications Of CVD Ceramic Coatings; Industrial Ceramics Vol 9 No3
- Butler E.G (1988) Engineering Ceramics: Applications And Testing Requirements; Int Jn High Tech Ceramics 4 pp93-102
- Butler E.G, Lewis M.H (1991) Prospects For Ceramics In Airborne Gas Turbine Engines
- Buddery.J.H. (1988) Furnace Design And Temperature Control; Int Jn High Tech Ceramics Vol4
- Caputo A. et al (1985) Development Of A New, Faster Process For The Fabrication of Ceramic Fiber Reinforced Ceramic Composites By Chemical Vapour Infiltration; US Department Of Energy, AR & ID Fossil Energy Materials Program (DOE/FE AA 15 10 10 0)
- Creber.D et al (1988) AlN Composite Growth By Nitridation of Aluminium Alloys; Engineering & Science Proc Vol 9, No7-9 pp975-82
- Chateigner.S,Jouin J.M.(1990) Reliability Thermomechanical And Fatigue Behaviour of High Temperature Structural Fibrous Ceramic Composites; Commission Of The Eur Comm's EUR 12810 EN
- CREIPI Report (1987) Study Of Thermal Shock Resistance Of Ceramics- Temperature Measurement Of Ceramics In A High Temperature And High Speed Combustion Gas Flow; Yokosuka Research Lab, EW86002
- Doebelin.E.(1983) Measurement Techniques, Applications And Design; 3rd Ed
- Evans, Marshall (1989) The Mechanical Behaviour Of Ceramic Composites; Acta Metal Vol 37, No 10 pp2567-2583
- Eurotherm Engineering (1989) GUIDE Book 818EN-3 Glasgow University Integrated Design Engine; Mech Eng Dept, Glasgow University
- Hancock J.W, et al (1990) Design Methods for the use Technical Ceramics and Ceramic Composites in Hostile Engineering Environmens; Dept of Mech Eng; Univ Glas; Sco
- Hartsock D, McLean A. (1984) What A Designer With Ceramics Needs; Cer Bulletin pp266-271
- Hoagland R.G, et al (1976) Reduction Of Errors In Ceramic Bend Tests; Am Cer Soc pp189-93
- Hopper. I (1993) Research Contract Final Report For Rolls Royce; Glasgow University
- Herceg.E.E (1983) Handbook Of Measurement And Control; Schaevitz Engineering

- Hillyer, R.D. (1990) Phase I Evaluation Of Sic/Sic Monotonic Tensile And Interlaminar Shear Behaviour; RR Rep MPI-85-90
- IEEE Spectrum (1990) Virtual Instruments; Nat Instruments
- Inghels E, Lamon J (1991) An Approach To The Mechanical Behaviour Of Sic/Sic And C/Sic Ceramic Matrix Composites Part 1/2; Jn Mat Science Vol26 pp5403-5419
- Jessen, Plumtree (1991) Continuum Damage Mechanics Applied To Cyclic Behaviour Of A Glass Fibre Putrusion; Composites Vol 22, No3
- Jamaluddin A, Fiveland W. (1990) Radioactive Transfer In Multi-Dimensional Enclosures With Specularly Reflecting Walls; ASME HTD V137 pp95-100
- Kachanov L.M (1986) Introduction To Continuum Damage Mechanics ISBN 90-247-3319-7
- Kodosky J et al (1989) Programming With Pictures; Comp Languages
- Langman R.D. (1987) Computer Control Of A Simple Electro-Thermal Process; IJEEE V24
- Lemaitre J, Chaboche J (1978) Aspect Phenemenologique De La Rupture Par Endomangement. J Applied Mechanics Vol2, pp317-365
- Kachanov L.M (1986) Introduction To Continuum Damage Mechanics; Martinus Nijhoff Publishers, ISBN 90-247-3319-7
- Klein (1986) Which Weave; Advanced Materials & Processes 3/86
- Kodosky J et al (1989) Programming With Pictures; Comp Languages
- Langman R.D (1987) Computer Control Of A Simple Electro-Thermal Process; IJEEE Vol 24
- Loveday M.S, Morrel R. (1988) Standardization Of Mechanical Testing And Quality Control; Int Jn High Tech Cer, V4
- Marsh A, Bell D (1988) High-Temperature Flexural Strength Of Engineering Ceramics; Inst Jn High Tech Cer V4
- Marschall C, Rudnick A. (1974) Conventional Strength Testing Of Ceramics Composites; US Report Mil AF 33(615)-2335
- Mecholsky J.J (1986) Evaluation Of Mechanical Property Testing Methods For Ceramic Matrix Composites; Cer Bul V65 pp315-323
- Morrell. R (1985) Handbook Of Properties Of Technical Engineering Ceramics, Part 1 HMSO
- Mullin J.V, Knoell A. (1970) Basic Concepts In Composite Beam Testing; MTRSA V10 pp16 No12 -20
- McCafferty J, Hancock J (1992) Experimental And Computational Models Of The Deformation Of Ceramic Composites By Micro-Cracking; In Proc, 1st Asian Pacific Conf
- McCarty L.H (1990) Software Simulates Instrumentation Systems; Design News Nat Inst's
- Newaz G.M, Walsh W. (1989) Interrelationship Of Damage And Strain In Particulate Composites; Jn Comp MatOs V23 pp326-337

- Newkirk M et al (1986) Preparation Of Lanxide Ceramic Matrix Composites: Matrix Formation By The Directed Oxidation Of Molten Metals; 11th Conf Composites And Advanced Ceramic Materials
- NI Application Note (1990) Thermocouples And Temperature Measurement; NI
- Philips L. N (1969) Carbon Fibre Reinforced In Plastics For Process Equipment; Process Engineering 12/69
- Quinn G.D (1991) Design Data For Engineering Ceramics: A Review Of The Flexure Test; Jn Am Cer Soc V74(9) pp2037-66
- Ramamurphy II et al (1990) Modelling Of Heat Transfer In Indirectly-Fired Continuous Reheating Furnace; ASME (STP844) HTD V146
- Richard.T.G. (1987) The Personal Computer As A Laboratory Instrument- Part1 Exp Techniques pp20-23
- Roscensaft M, Marom G (1985) Evaluation Of Bending Test Methods For Composite Materials; Jn Comp Tech & Res V7(1) pp12-16
- Schiroky G Et Al (1989) Ceramic Composites For Gas Turbines Via A New Process; Gas Turbine & Aeroengine Congress
- Schlichting (1980) Chemical Vapour Deposition of Silicon Carbide, Review 13; Powder Met Int Vol 12, No 3
- Sorensen B.F (1993) Analysis Of Damage In A Ceramic Matrix Composite. J Damage Mechanics, Vol2 pp246-72
- Stephanie J, Rickerl P (1991) Infrared Curing Of Polyimides; ANTEC V37 pp1696-99
- Severn Furnaces Ltd Bristol BS12 2UR
STP 470B (1990) Manual On The Use Of Thermocouples; ASTM

Appendix A1

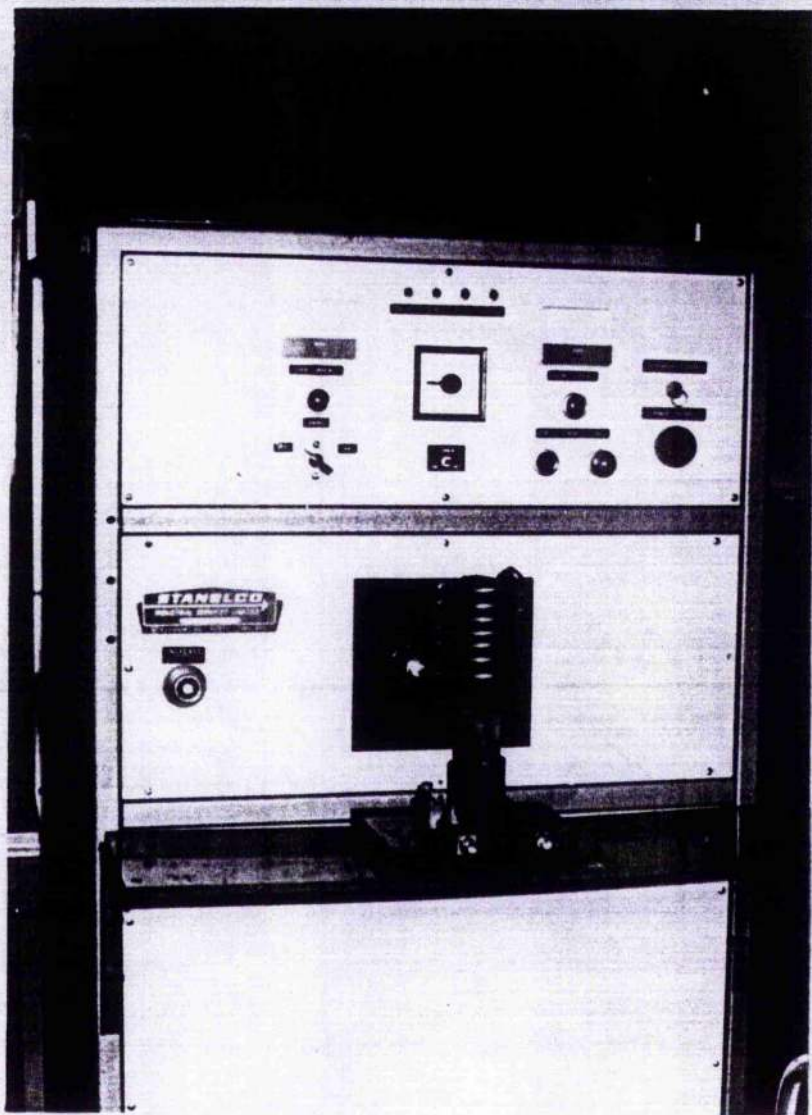


Fig A1-1 RF (470kHz) Induction Generator having a power consumption of 12-15kW

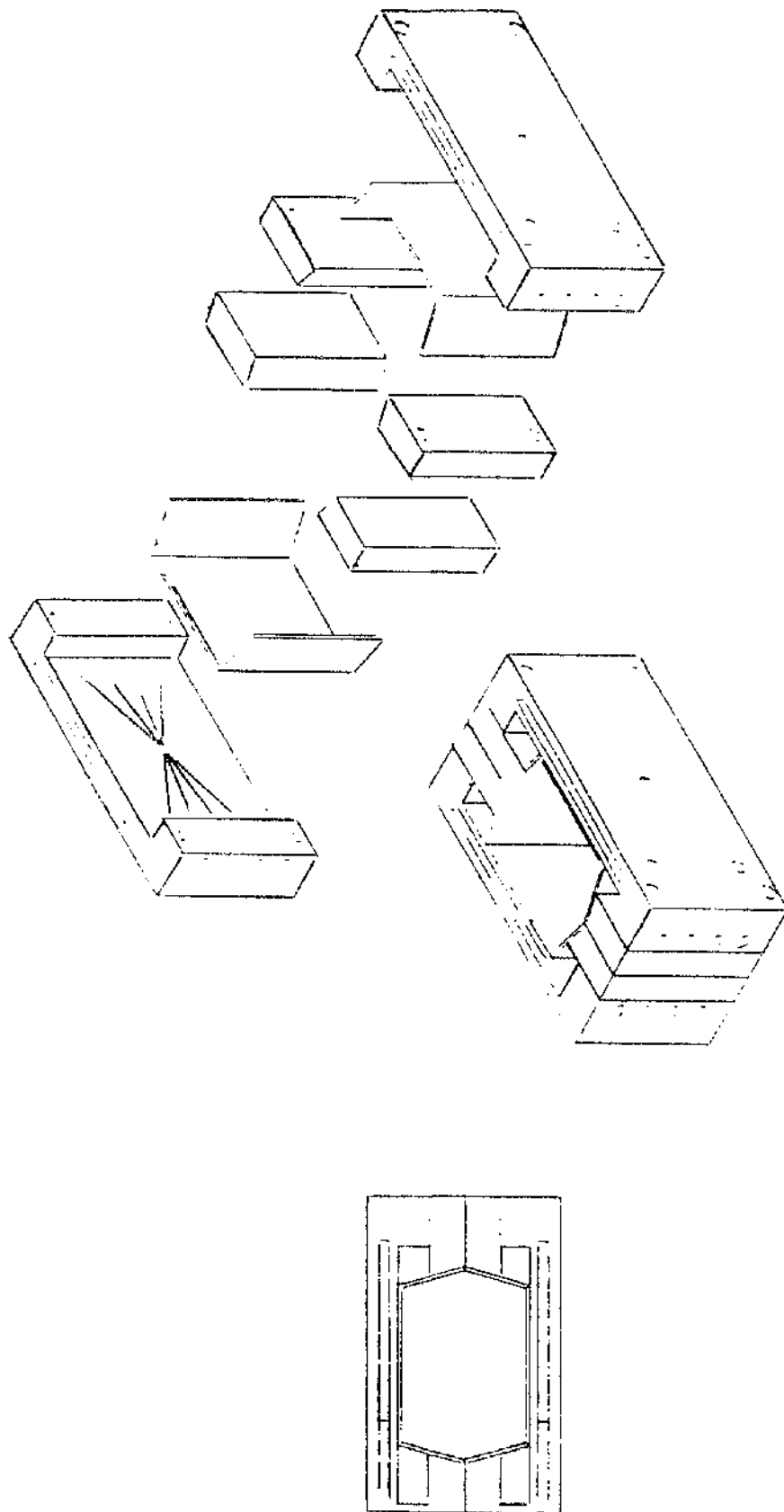


Fig A1-3 Split Horizontal Furnace Exploded View

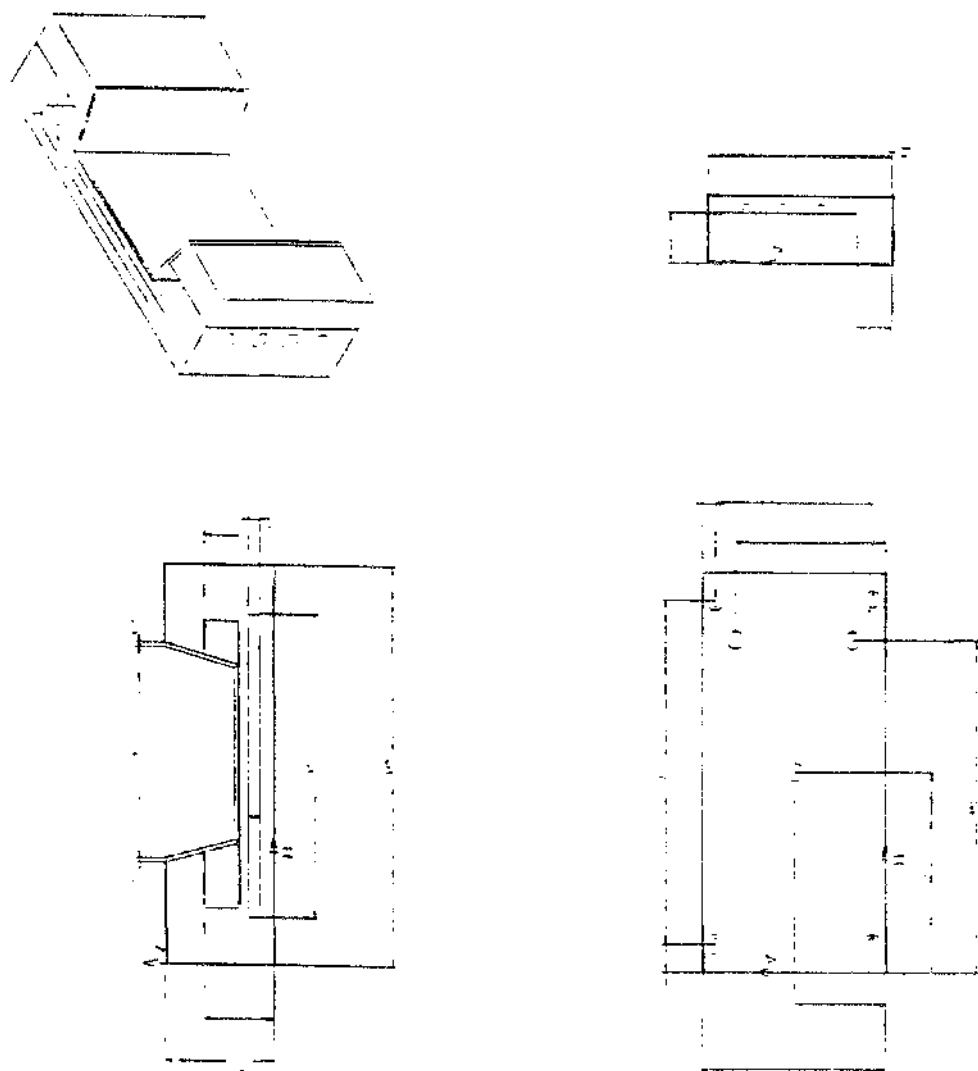


Fig A1-4 Split Horizontal Furnace Dimensioned View

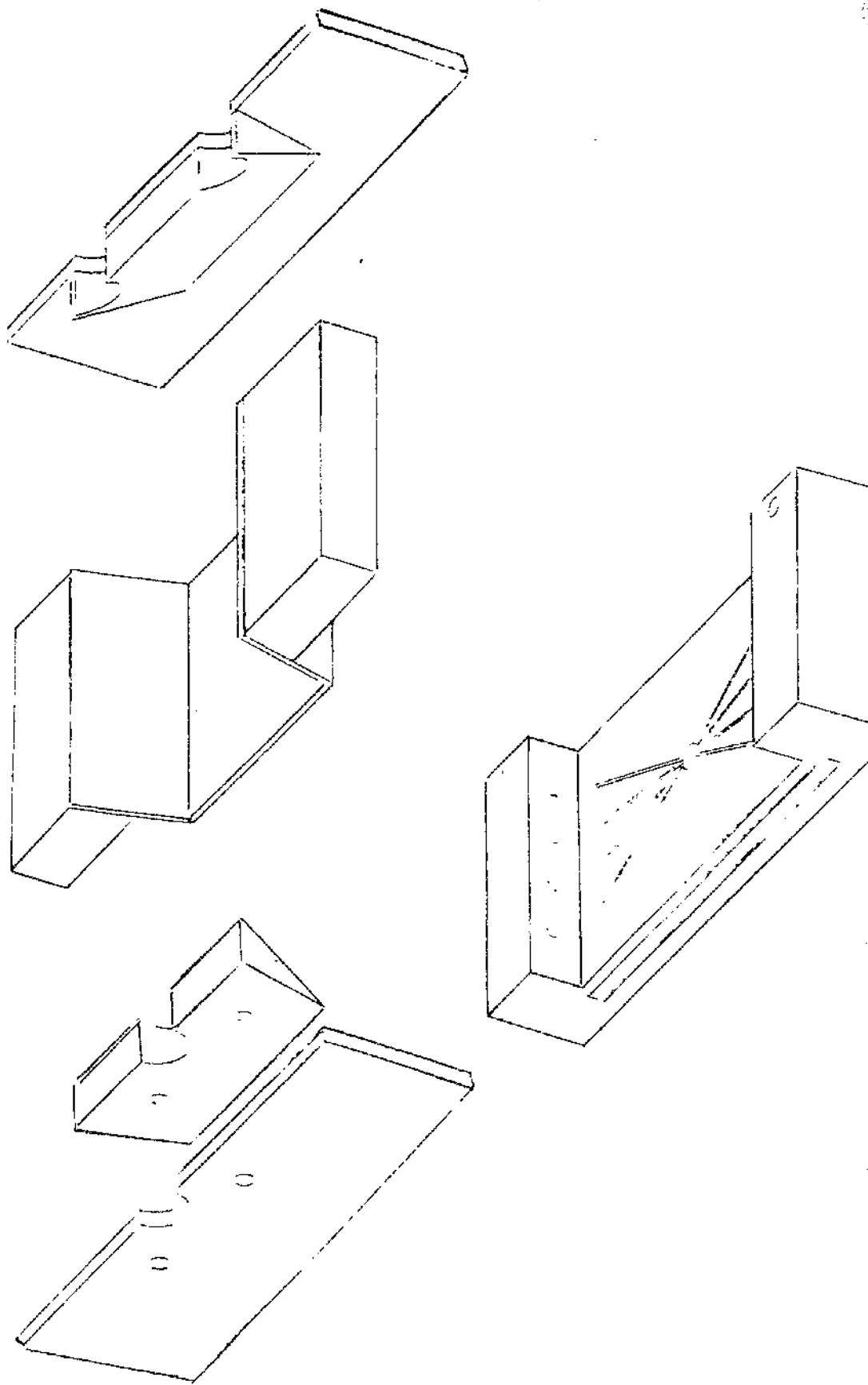


Fig A1-5 Split Horizontal Furnace Side/Base Exploded View